



室蘭工業大学

学術資源アーカイブ

Muroran Institute of Technology Academic Resources Archive



旋回シュートにおけるエロージョンの数値解析と摩耗予測

メタデータ	言語: eng 出版者: 公開日: 2018-05-24 キーワード (Ja): キーワード (En): 作成者: 肖, 磊 メールアドレス: 所属:
URL	https://doi.org/10.15118/00009626

平成 29 年度 博士学位論文

旋回シュートにおけるエロージョンの数
値解析と摩耗予測

肖 磊

室蘭工業大学大学院工学専攻
先端生産システム工学コース

Doctoral Thesis

**Numerical simulation of erosion and erosive
prediction on rotating chute**

Lei XIAO

Course of Advanced Production Systems Engineering
Muroran Institute of Technology, Japan

2017. 6

CONTENTS

Chapter 1 Introduction and background	1
1.1 Introduction of wear	1
1.2 Introduction of erosive	2
1.3 Erosion models	5
1.3.1 Finnie's model	5
1.3.2 Bitter's model	6
1.3.3 Hutching's theory	7
1.3.4 Levy's theory	9
1.3.5 Tilly's model	10
1.4 Numerical simulation of erosion	11
1.5 Structure of this thesis	14
References	16
Chapter 2 Experiments	21
2.1 Introduction	21
2.2 Materials	21
2.3 Experimental method	23
2.3.1 Apparatus	23
2.3.2 Erosion test	24
2.3.3 Single particle impact test	25
2.4 Summarization	25
References	25
Chapter 3 Impact angle dependence of erosion for spheroidal carbide cast iron	26
3.1 Introduction	26

3.2 FEM analysis	26
3.3 Results	28
3.3.1 Analytical results	28
3.3.2 Results of single particle impact tests	28
3.3.3 Discussion of correlation between test results and analytical results	29
3.4 Discussion	32
3.4.1 Discussion of von mises stress	32
3.4.2 Discussion of impact angle dependence based on equivalent plastic strain	33
3.5 Conclusions	35
References	35

Chapter 4 Finite element analysis of single particle impact on mild steel and spheroidal graphite cast iron

4.1 Introduction	37
4.2 Finite element modeling	37
4.3 Results and discussion	42
4.3.1 Crater	42
4.3.2 Dependence of impact angle from test	45
4.3.3 Dependence of impact angle FE simulation	45
4.4 Conclusions	51
References	52

Chapter 5 A comparative study of material loss and crater deformation on ductile material during erosion simulation using 2 different material models

5.1 Introduction	53
5.2 Simulation	54
5.2.1 Material models	54
5.2.1.1 Johnson-Cook material model	54
5.2.1.2 Simple material model	55

5.2.1.3 Material failure	55
5.2.2 Finite Element Modeling	56
5.3 Results and discussion	57
5.3.1 Effect of shear failure for simple material model	57
5.3.2 Effect of friction coefficient	60
5.3.3 Craters of single particle impact	62
5.4 Conclusions	65
References	66

Chapter 6 Impact simulation of angular particles on mild steel using a coupled method of finite element and smoothed particle hydrodynamics	68
6.1 Introduction	68
6.2 Brief description of SPH theory	69
6.3 Simulation	71
6.3.1 Johnson-Cook material model	71
6.3.1.1 Constitutive equation and failure equation	71
6.3.1.2 Equation of State (EOS)	72
6.3.2 Numerical modeling	73
6.4 Results and discussion	77
6.4.1 Comparison of sphere impact and cone impact	77
6.4.2 Effect of angularity for single cone impact	80
6.5 Conclusions	84
References	85

Chapter 7 Erosive prediction on liners of rotating chute using a coupled simulation of DEM and FEM	87
7.1 Introduction	87
7.2 Brief description of DEM theory	88
7.3 Numerical model	91

7.4 Results and discussion	95
7.4.1 Flow of raw materials	95
7.4.2 Stress state on liners	96
7.5 Conclusions	102
References	103
Chapter 8 General conclusions and prospects for future work	104
8.1 General conclusions	104
8.2 Prospects for future work	107
ACKNOWLEDEMENT	108
PUBLICATIONS AND PRESENTATIONS	109
LIST OF FIGURES	110
LIST OF TABLES	115

Chapter 1

Introduction and background

1.1 Introduction of wear

In many industrial fields such as chemical engineering, petroleum, metallurgy, mining and power industry etc., there must be some hostile work environments including high temperature, high pressure, high corrosion and much dust. The devices working in these environments may face a serious common problem, which is wear. Especially on the pipes of solid-fluid convey and corrosive liquid delivery systems, wear is particularly outstanding. Due to wear, microstructure, chemical composition, chemical and mechanical properties of material may change, crack and material removal may also occur, shortening the service lives and performances of components using these materials, even leading to catastrophic danger, so regular maintenances have to be made on these damaged devices, or new components have to be replaced for damaged components regularly, not only affecting operating safety but also causing economic loss as well. According to some estimations, approximately about one-third of the world's energy resources are cost down by friction in one form or another [1], some surveys around 2~3 decades ago showed that wear and friction cost Canada in excess of \$5 billion per year and cost the United States more than \$100 billion per year [2]. In the other hand, wear is also useful for mankind, dating back to thousands years ago, tools with sharp cutting edge such as knives, axes, swords and arrows were made by ancient people for hunt and war, and in recent years, some advanced machining processes based on wear were also proposed and put into application, such as water jet machining (WJM), electrochemical machining (ECM) and chemical machining (CHM) etc. [3].

Wear is defined by ASTM (American Society for Testing and Materials) as “damage to a solid surface, generally involving the progressive loss of material, due

to relative motion between that surface and a contacting substance or substances” [4]. According to different working mechanisms, wear can be classified into several categories: Adhesive wear, Slide wear, Erosive wear, Fretting wear, Fatigue wear and other forms of metal wear. However, in real cases, it is too difficult to distinguish one type of wear with another clearly, because wear is a complicated surface damage process caused by the interactions of two or more materials, usually accompanied with physical and chemical changes. In many cases one type of wear transfers into another, and two or more types of wear operate together [5, 6]. In scientific research, people tend to simplify the complex problem into several individual simple problem, these simple problems are analyzed separately so as to get a better understanding of the original complex problem. In this thesis, erosive wear is taken out separately from the complex wear phenomenon and selected as research subject.

1.2 Introduction of erosive wear

Erosive wear, also named as erosion, is deformation or loss occurred on the material surface caused by impact of small disperse solid particles. It is an important material failure mode in components like pipes, valves, pumps, turbine blades, powder mixers in many industrial devices for solid-gas delivery and pneumatic conveying system. Take blast furnace as an example, blast furnace is an usual device in modern iron-making industry, at the top of blast furnace, raw materials were charged into the blast furnace through rotating chute, so impact between raw materials and inner surface of rotating chute is very serious, leading to serious erosion on the inner surface of rotating chute, meanwhile, at the bottom of blast furnace, pulverized coal was injected into blast furnace through tuyeres, so serious erosion also occurs on the inner surface of pipelines by impact of pulverized coal particles, erosion phenomenon in blast furnace is shown in Fig. 1.1 schematically.

Erosion is defined by ASTM as “progressive loss of original material from a solid surface due to mechanical interaction between that surface and a fluid, a multicomponent fluid, or impinging liquid or solid particles” [7]. The process of erosion is very complex, so it is difficult to describe erosion mechanisms. In general,

erosion mechanisms are different for different types of materials. For ductile materials such as pure metals and alloys, the impact of hard particles causes severe, localized plastic strain at the impact site on the surface. Material is removed when the strain exceeds the material's strain-to-failure. For brittle materials, such as ceramic and intermetallic compounds, the force of impacting particle causes localized cracking at the surface. With subsequent impact, these cracks propagate and eventually link together, and as a result, material becomes detached from the surface [8]. The factors influencing erosions are also very complicated. These factors were broadly classified into 3 categories according to previous study: (i) impingement variables describing the particle flow (particle velocity, angle of impact, particle concentration) (ii) particle variables (particle shape, particle density, particle size) (iii) material variables (Young's modulus, Poisson's ratio, plastic behavior, failure behavior, hardening behavior, microstructure, hardness, toughness) [9], Fig. 1.2 shows the classification of these factors. In general, erosion for ductile material tend to reach maximum at impact angles ranging from 15deg. to 30deg., meanwhile erosion for brittle material tend to reach maximum at impact angles ranging from 80deg. to 90deg., and erosion for cast iron tend to reach maximum at impact angles ranging from 50deg. to 70deg., typical curves of relationship between erosion rate and impact angle are shown in Fig. 1.3 [10].

In order to make it clear the effect of factors affecting erosion and erosion mechanisms for different types of materials. A great number of experiments were taken. Based on the results of these experiments, a large number of models were proposed to describe mechanisms of erosion, and also, a large number of empirical or semi-empirical equations were developed to predict the erosion amount on eroded materials. Meng reviewed the journal *Wear* from 1957 to 1992 and *Wear of Materials (WOM)* conferences from 1977 to 1991, the total number of involved papers was 5466 (4726 in *Wear*, 740 in *WOM*), and found that more than 300 equations were proposed to describe frictional phenomena, of course a significant number of equations relate to wear but were not particularly amenable to analysis, so 28 erosion wear equations were listed in the appendix of this paper [11]. In section 1.3, several

models and equations of erosion proposed by previous researchers are briefly introduced.

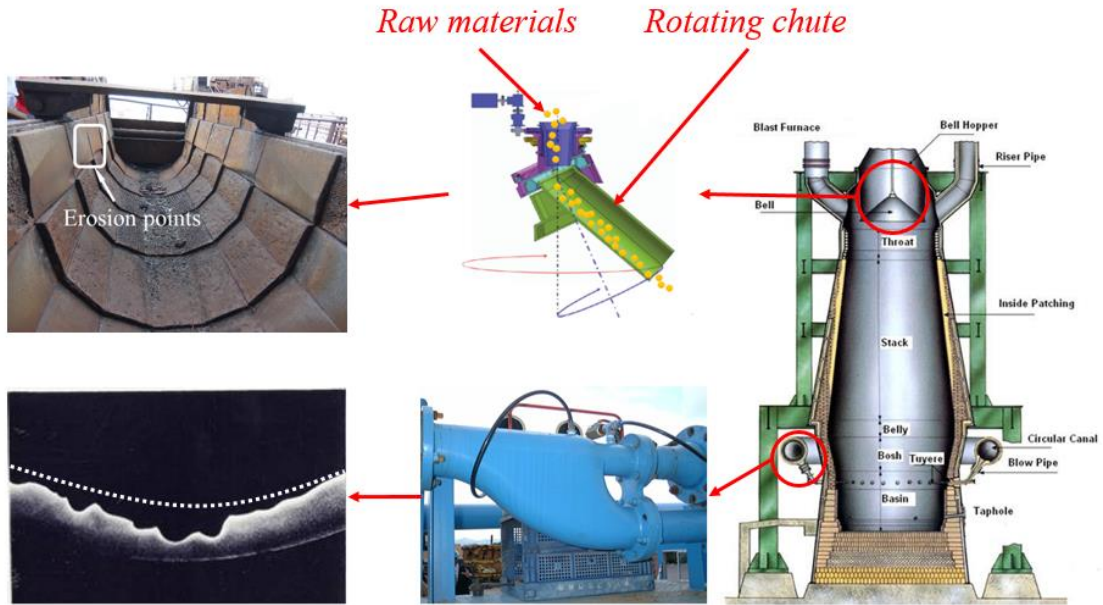


Fig. 1.1 Erosion phenomenon in blast furnace

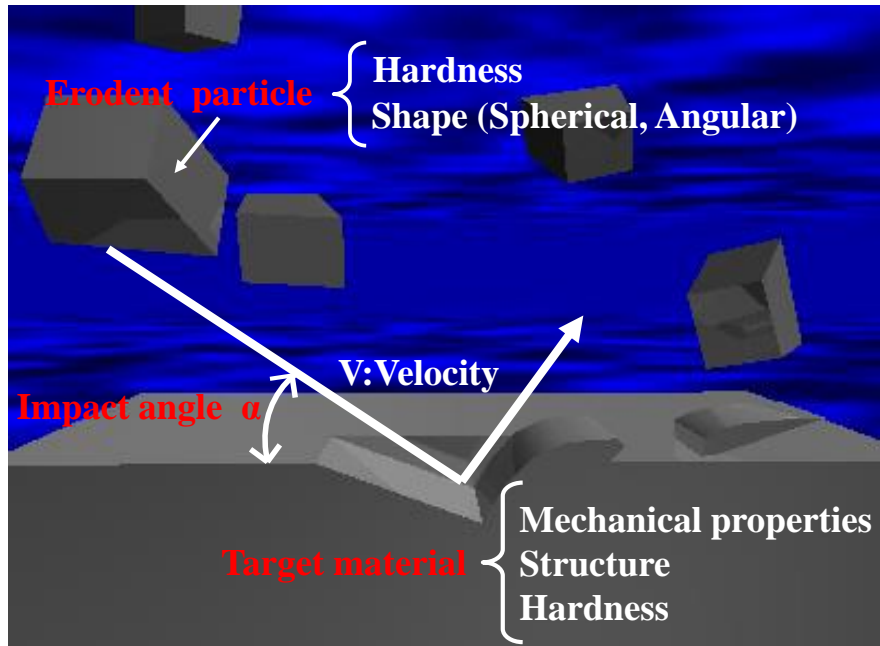


Fig. 1.2 Classification of factors affecting erosion

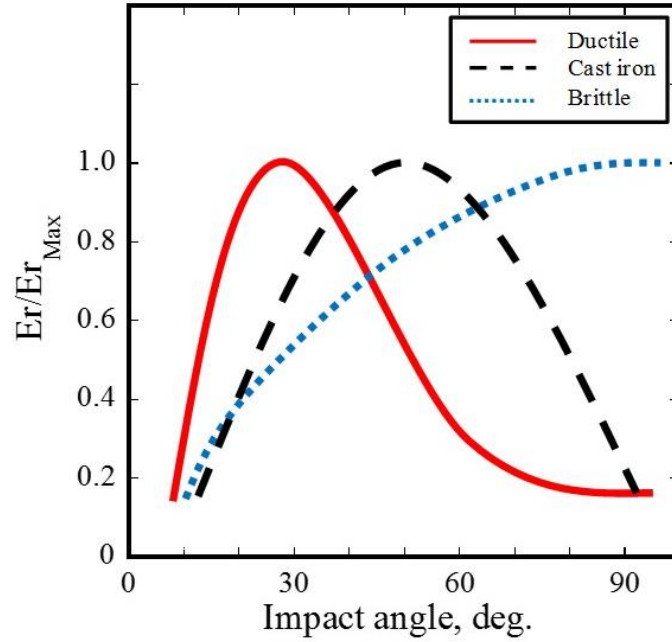


Fig. 1.3 Typical curves of erosion and impact angle for ductile/brittle materials and cast iron

1.3 Erosion models

1.3.1 Finnie's model [12]

Finnie developed the first theoretical model for erosion. For erosion of ductile material, the model is derived from the motion of a single angular rigid abrasive particle striking a ductile material surface to displace or cut away part of material. The equation is expressed as Eq. 1-1,

$$\begin{aligned}
 Q &= \frac{mV^2}{p\psi K} \left(\sin 2\alpha - \frac{6}{K} \sin^2 \alpha \right) & \tan \alpha &\leq \frac{K}{6} \\
 Q &= \frac{mV^2}{p\psi K} \left(\frac{K \cos^2 \alpha}{6} \right) & \tan \alpha &\geq \frac{K}{6}
 \end{aligned}
 \tag{1-1}$$

Where, Q is volume of removed material, m is the mass of abrasive particle, K is the ratio of vertical to horizontal force components, ψ is ratio of the depth of contact l to the depth of the cut (y_t), as shown in Fig. 1.4. V is the velocity of abrasive particle, p is the plastic flow stress.

Comparing to experimental results, the results of Eq. 1-1 agrees closely at low impact angles but underestimates at high impact angles, no erosion is obtained at impact angle 90deg. if calculates using Eq. 1-1, however erosion still exists at 90deg.

actually. The disagreement between equation result and actual result is because only one face of abrasive particle is considered to contact with material surface for Eq. 1-1, as shown in Fig. 1.4, however both faces may contact with material surface actually.

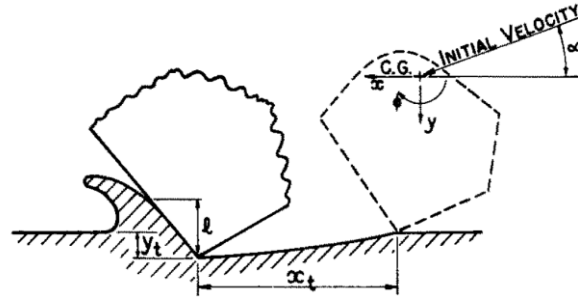


Fig. 1.4 Schematic view of Finnie's model for ductile material [12]

1.3.2 Bitter's model [13, 14]

Bitter assumed that erosion is sum of deformation wear W_d and cutting wear W_c . The repeated collisions of a large number of particles increases the elastic limit and eventually make it equal to strength of the impacted material, meaning that material become relatively hard and brittle and can no longer be plastically deformed. With further deformation, if the elastic limit is exceeded, the surface layer is destroyed and fragments of it are removed. If a particle strikes a horizontal surface at an acute angle, the material is subjected to shear, if shear strength is exceeded, destruction occur.

Based on Hertian contact theory and energy balance equation, an equation for deformation wear W_d is derived, as expressed in Eq. 1-2,

$$\begin{aligned}
 W_d &= \frac{M(V\sin\alpha - V_{el})^2}{2\varepsilon} & V\sin(\alpha) > V_{el} \\
 W_d &= 0 & V\sin(\alpha) < V_{el}
 \end{aligned}
 \tag{1-2}$$

Where, M and V are total mass and velocity of impact particles respectively, α is the attack angle, ε is the energy needed to remove a unit volume of material from the body by deformation wear, and V_{el} is threshold velocity of collision at which the elastic limit is just reached, V_{el} is computed using the collision of a sphere with a flat body, obtained by Eq. 1-3,

$$V_{el} = \frac{\pi^2}{2\sqrt{10}} y^{\frac{5}{2}} \left(\frac{1}{d}\right)^{\frac{1}{2}} \left[\frac{1 - q_1^2}{E_1} + \frac{1 - q_2^2}{E_2} \right] \quad (1-3)$$

Where, y is elastic load limit, d is density of sphere, q_1 and q_2 are poisson's ratio of sphere and flat body, E_1 and E_2 are Young's modulus of sphere and flat body.

Cutting wear W_c is expressed as Eq. 1-4,

$$W_c = \frac{2MC(V\sin\alpha - V_{el})^2}{\sqrt{V\sin\alpha}} \left(V\cos\alpha - \frac{C(V\sin\alpha - V_{el})^2}{\sqrt{V\sin\alpha}} \ell \right) \quad \alpha \leq \alpha_0 \quad (1-4)$$

$$W_c = \frac{M[V^2\cos^2\alpha - K_1(V\sin\alpha - V_{el})^{3/2}]}{2\ell} \quad \alpha \geq \alpha_0$$

Eq. 1-4 is valid at $V\sin(\alpha) \geq V_{el}$, α_0 is the impact angle at which the horizontal velocity component has just become zero when the particle leaves the body. ℓ is cutting wear factor obtained experimentally. C and K_1 are obtained using Eq. 1-5 and Eq. 1-6 respectively,

$$C = \frac{0.288}{y} \sqrt[4]{\frac{d}{y}} \quad (1-5)$$

$$K_1 = 0.82 y^2 \sqrt[4]{\frac{y}{d}} \left(\frac{1 - q_1^2}{E_1} + \frac{1 - q_2^2}{E_2} \right)^2 \quad (1-6)$$

1.3.3 Hutching's theory [15-17]

Hutching and his coworkers analyzed the process of material removal by observing the appearance and microscopic section view of craters. When particle impact on surface of specimen, the impact of particle exerts shear action on surface layer to form a lip at the exit end of crater. Above a critical velocity, the lip is detached from the surface by propagation of ruptures at the base of the lip, the craters formed in aluminum specimens at impact angle 18.5deg. and impact velocity 220 m/s and 210 m/s are shown in Fig. 1.5 [15].

Erosion mechanism of particle impact on ductile material at oblique impact angle was further classified into two distinct modes of surface deformation, namely cutting and ploughing. Fig. 1.6 shows the schematic view of these two deformation modes under an angular particle impact [16]. When the angle between leading edge of

particle and material surface is larger, cutting deformation occurs. Cutting is also called as micromachining in [16]. Meanwhile, when the angle between leading edge of particle and material surface is small, ploughing deformation occurs. In [17], it is also noted that surface deformation by spherical particles impact is similar to ploughing deformation, as shown in Fig. 1.7. In the process of cutting deformation, it may also occur that cutting edge of the particle tends to bury itself deeply into the specimen rather than scooping out material as a chip. Material can be removed as a result of a particle breaking up during its cutting action. At this moment, a lip raised during the early stages of the impact is subsequently cut off by fragments of the particle [16].

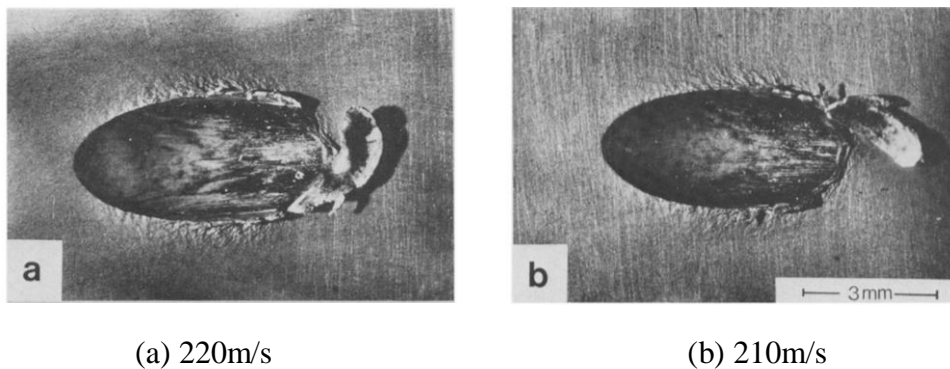


Fig. 1.5 Craters on aluminum specimens at impact angle 18.5deg., impact velocity is 220m/s and 210m/s [15]

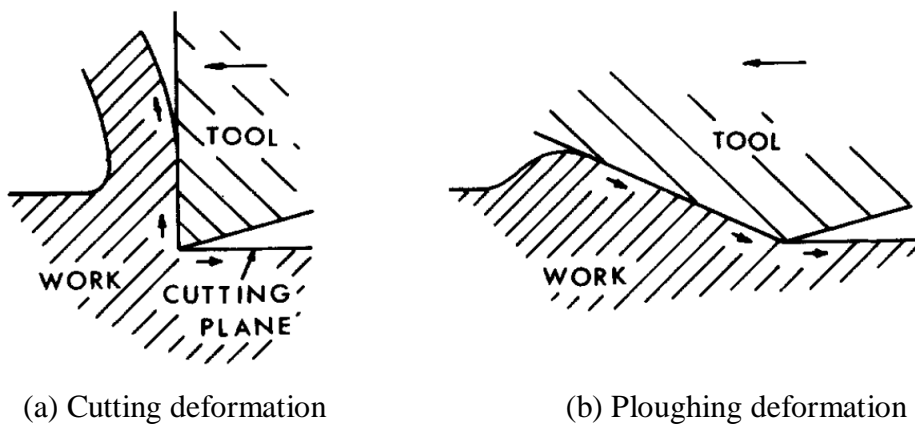


Fig. 1.6 Two modes of surface deformation impacted by an angular particle [16]

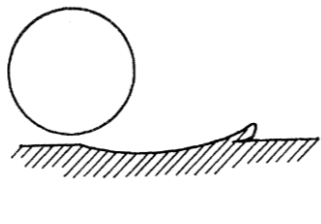


Fig. 1.7 Surface deformation impacted by a spherical particle [17]

1.3.4 Levy's theory [18]

Levy argued that micromachining is not the mechanism of erosion on ductile material. Through analysis of the incremental erosion rate, it was found that initial erosion rate caused by the first initial batch of particles was much lower than that caused by subsequent batches of particles, as shown in Fig. 1.8. If micromachining was the mechanism of erosion, initial incremental erosion rate on uneroded surface should be higher than subsequent incremental erosion rate on eroded surfaces because work hardening of material surface due to machining action would have reduced machinability of the surface.

A Platelet mechanism was proposed to explain the erosion on ductile materials. The surface material is extruded by impact of particles and platelets were formed, with subsequent particles impact, platelets spread by forging and finally remove from material surface. A large number of experiments were taken to validate this mechanism theory.

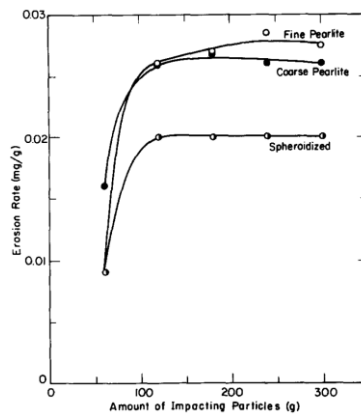


Fig. 1.8 Incremental erosion rate of 1075 (240 μ m SiC; velocity $V=30.5$ m/s; angle of impingement, 30deg.) [18]

1.3.5 Tilly's model [19]

According to high speed photographic and metallographic observation, Tilly argued that erosion of ductile materials occurs in two stages. The first stage is when the impacting particle strikes the surface to produce an indentation and possibly remove a chip of metal. The second stage is when the particle breaks up and fragments are projected radially from the primary site. So the erosion in these two stages was analyzed separately. The primary erosion is expressed as Eq. 1-7,

$$\varepsilon_1 = \hat{\varepsilon}_1 \left(\frac{V}{V_r} \right)^2 \left[1 - \left(\frac{d_0}{d} \right)^{\frac{3}{2}} \frac{V_0}{V} \right]^2 \quad (1-7)$$

Where, erosion (ε) is defined as the material removal by unit mass of impacting particles. d_0 is a threshold size of particle, no erosion occurs below d_0 . d is size of particle. V_0 is threshold velocity of particle, no damage occurs below V_0 . When particle size and velocity are with respect to d_0 and V_0 , V_r is the velocity for maximum erosion $\hat{\varepsilon}_1$. V is any velocity of particle. The secondary erosion is expressed as Eq. 1-8,

$$\varepsilon_2 = \frac{V_r^2}{\psi} F \quad (1-8)$$

Where, ψ is the second erosion factor. F is the degree of fragmentation which is a function of velocity, particle size and impact angle. F is expressed as Eq. 1-9,

$$F = \frac{W_0 - W}{W_0} \quad (1-9)$$

Where, W_0 is the proportion of particles (by weight) within the specialized size range before testing and W is the proportion after testing. If all particles were broken into smaller fragments, F is 1. If $\hat{\varepsilon}_2$ is maximum secondary erosion, Eq. 1-8 becomes Eq. 1-10,

$$\varepsilon_2 = \hat{\varepsilon}_2 \left(\frac{V}{V_r} \right)^2 F_{d,v} \quad (1-10)$$

Where, $F_{d,v}$ is fragmentation for particle size d and velocity V .

Combined Eq. 1-7 and Eq. 1-10, the total erosion can be expressed as Eq. 1-11,

$$\varepsilon = \hat{\varepsilon}_1 \left(\frac{V}{V_r} \right)^2 \left[1 - \left(\frac{d_0}{d} \right)^{\frac{3}{2}} \frac{V_0}{V_r} \right]^2 + \hat{\varepsilon}_2 \left(\frac{V}{V_r} \right)^2 F_{d,v} \quad (1-11)$$

1.4 Numerical simulation of erosion

The previous researches mentioned in section 1.3 were based on erosion experiments. It is no doubt that experiment is a direct method for erosion research. However, experiment is a time-consuming and labor-intensive way for researches. Furthermore, as mentioned before, erosion is a complex process affected by many factors, these factors influence erosion simultaneously and synergistically, so it becomes difficult to get an insight into the effect of each factor experimentally so as not to understand erosion mechanism completely. In addition, it is also impossible to obtain all information during erosion process experimentally, such as stress, plastic strain, change of solid particle velocity and energy etc.. With advancement of computational technology, numerical simulation has become an effective and efficient way to overcome shortages of experiment, and has been put into application in erosion researches since 1990s.

Finite Element Method (FEM) is most widely used in areas of erosion researches. Shimizu et al. presented two-dimensional (2D) FE models to investigate the impact angle dependency of erosion on mild steel and ferritic spherical-graphite cast iron, the target material in FE models were impacted by single particle, plastic strain was used as evaluation [20-22]. In 2D FE models, impact particle was simplified as cylinder rather than sphere, so the simulations could not correctly reflect the actual conditions during erosion, some three-dimensional (3D) FE models were put forward in the subsequent erosion simulation. Molinari et al. performed 3D FE simulations of metallic plates by spherical particles impact with a view to develop an insight into the fundamental mechanisms of erosion, the roles of plastic flow, friction and adiabatic shearing during erosion were revealed [23]. Griffin et al. developed a 3D FE model with 5 solid particles to investigate the erosion process on an alumina scale/MA956

substrate, damage accumulation was computed by using two failure models, namely shear failure model and tensile failure model [24]. Eltobgy et al. investigated the erosion process of ductile material Ti-6Al-4V by building a FE model with 3 solid particles, Johnson-Cook material model was applied into the target material [25]. Aquaro et al. developed a FEM codes to simulate the erosions on brittle and ductile materials, the erosion criterions in these codes were based on the theoretical models proposed by previous researchers [9, 26, 27]. Yang et al. used Johnson-Cook and Johnson-Holmquist material models for ductile material Ti-6Al-4V and brittle material SiC ceramic respectively, investigated their erosion processes under impact of 100 SiC particles [28]. Liu used Wang's model, investigated the effect of particle shapes on erosion of ductile materials impacted by 4 different shape particles, including cube, dodecahedron, icosahedron and sphere [29].

FEM has its intrinsic advantages for simulation, such as time- or memory-saving. However, there are still some limitations for applications of FEM, for example, when target material is impacted by tip of angular particles or particles with high velocity, distortion or tangle of meshes may occur on the target material, dramatically decreasing the accuracy of simulation results. Therefore, a Mesh-free method named as Smoothed Particles Hydrodynamics (SPH) was utilized in erosion simulation to overcome these limitations. In SPH, Lagrange meshes of FEM were replaced with a set of scattered particles, which could avoid mesh distortion or tangling due to large deformation of material. Papini et al. used SPH method to conduct impact simulation of angular particles on ductile material copper and Al6061-T6 [30-32], and particle embedment on ductile material Al6061-T6 during erosion [33]. Yang et al. used a coupled algorithm of SPH and FEM to investigate erosion process of 5 spherical particles impact on ductile material Ti-6Al-4V [34], and impact process of single spherical particle on ductile metal pipe with polymer coatings [35].

A special simulation method, named as micro-scale dynamic model (MSDM), was proposed by Prof. D. Y. Li and his coworkers [36], and has been applied to simulate solid particles erosion on ductile, brittle, composite material and alloy etc. [37-44].

Amongst the above simulations, erosion by large number of particles impact has

been involved in some numerical models. For example, in FE models of [28] and [29], target materials were impacted by 100 spherical particles, while in SPH models of [30] and [31], target materials were impacted by 105 irregular particles. However, in these models, the interactions between solid particles were totally ignored, which is an obvious shortage for these models. The numerical model of [30] is shown in Fig. 1.9. In addition, the FE method in the above simulations was also utilized in the research of an advanced machining process named as Abrasive Water Jet (AWJ) [45, 46], but in real cases of AWJ, solid particles are conveyed with fluid, but the simulation of this method did not take fluid into consideration. So although results of these models agreed well with test results so that these FE or SPH methods can be seen as a powerful tool to assist experiments, there were still disagreements between simulation conditions and test conditions. In recent years, Discrete Element Method (DEM) was applied into erosion simulations. Because of its strong ability to handle large number of particles, the interactions between particles can be simply defined. Besides, a coupled algorithm of Computational Fluid Dynamics (CFD) and Discrete Element Method (DEM) was also proposed recently, making simulation of solid-fluid delivery easier, so the CFD-DEM method provided an effective way to take simulation of erosion considering influences of fluid conveying solid particles. In [47], impact of different parameters on screening efficiency and mesh wear was studied using DEM. In [48], CFD-DEM was conducted in simulation of particulate flow in feed pipes, an approach combining experimental and numerical simulation was initiated to get a fundamental understanding of erosion mechanisms on pipe bends. In the simulations of [47] and [48], DEM was used to create solid particles. Whereas, in [49-52], Prof. Zang and his coworkers also applied DEM into impact simulation on glass, and the target material was built as an array of DEM particles, as shown in Fig. 1.10. Their work provided a new idea for erosion simulation in the future.

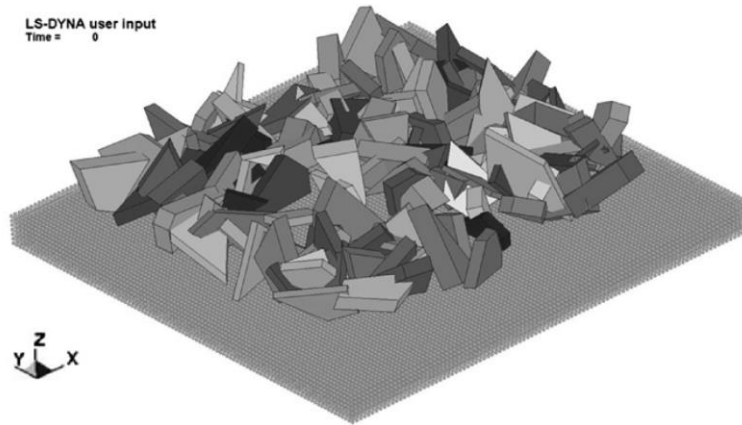


Fig. 1.9 Numerical model of 105 irregular particles impact in [30] (target material is built using SPH method)

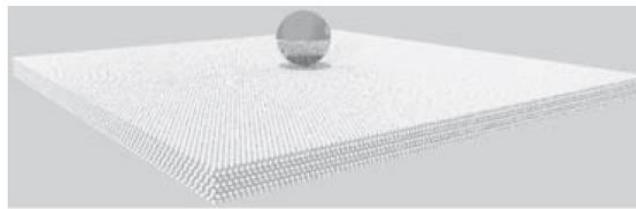


Fig. 1.10 Numerical model in [47] (target material is built using DEM)

1.5 Structure of this thesis

In the previous study of our laboratory, 2D FE models were built, as shown in Fig. 1.11. There are some discrepancies between 2D FE model and actual erosion process, so some improvements were made in the work of this thesis. The main contents in each chapter are listed as below.

In chapter 1, research introduction and background are described.

In chapter 2, erosion experiments for this thesis are described.

In chapter 3, 3D FE models of single particle impact on spheroidal carbide cast iron and spheroidal graphite cast iron were built.

In chapter 4, 3D FE models of single particle impact on mild steel and spheroidal graphite cast iron were built.

In chapter 5, a 3D FE model of 5 spherical particles impact on mild steel was built. Material failure criterion was applied into target material to make material loss appear.

In chapter 6, 3D numerical models were built using a coupled algorithm of SPH and FEM. The impact region on target material was built by SPH method to avoid mesh distortion and tangling when impacted by angular particles.

In chapter 7, DEM was used to simulate raw materials flow in rotating chute. Erosion on inner surface of rotating chute was predicted.

In chapter 8, general conclusions and prospects for future work are described.

The structure of works in this thesis is shown in Fig. 1.12.

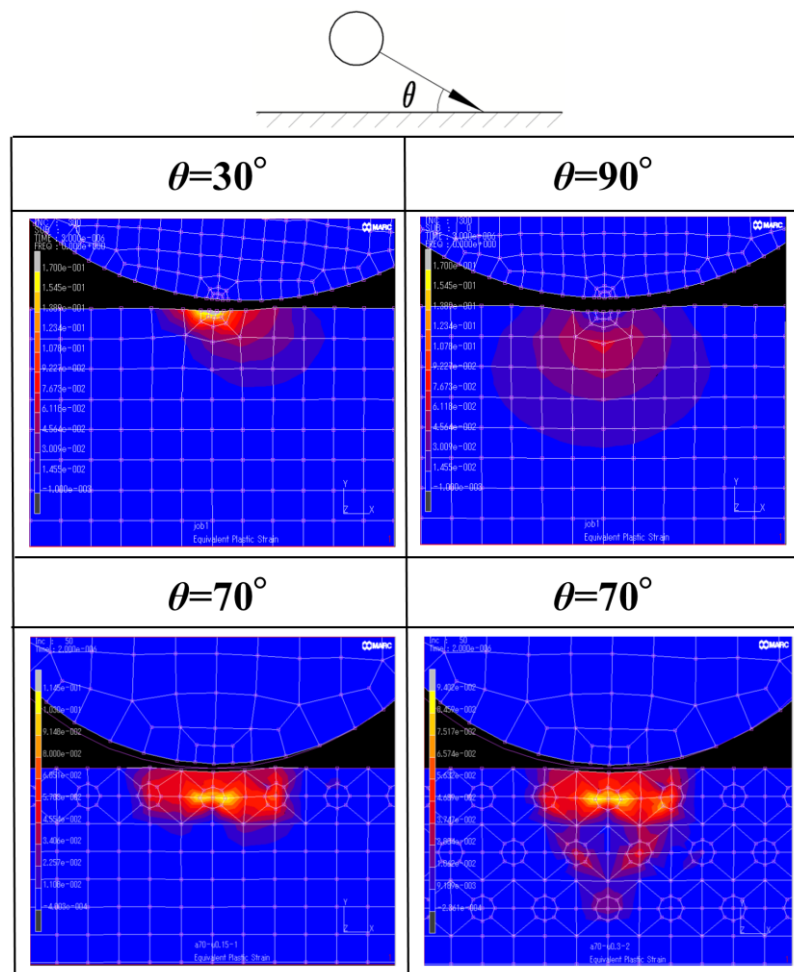


Fig. 1.11 Previous FE models of our laboratory [20-22]

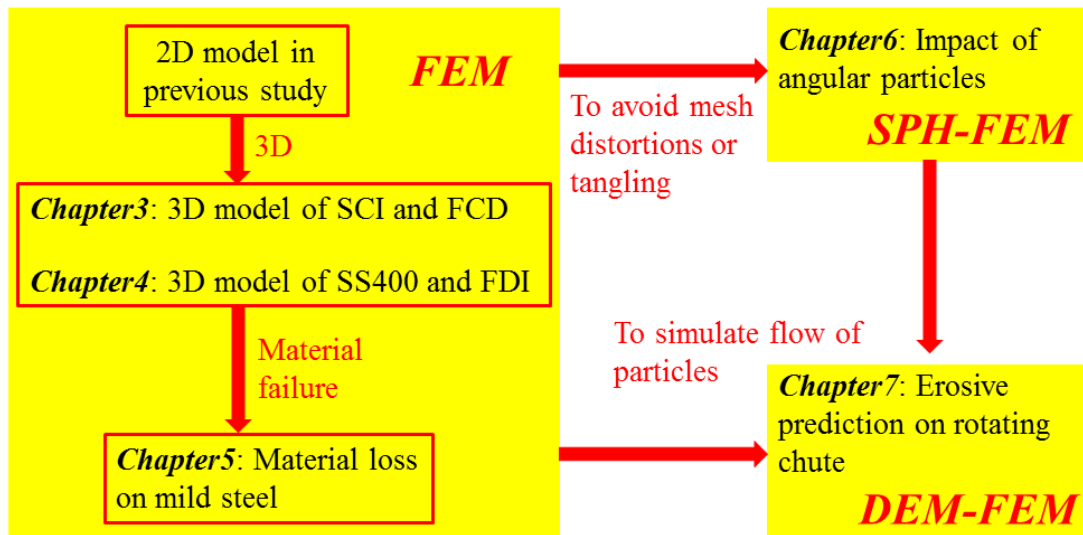


Fig. 1.12 Structure of works in this thesis

References

- [1] Bharat Bhushan, Introduction to tribology, John Wiley & Sons, 2013.
- [2] Khaled Taher Elalem, Development of a micro-scale dynamic model for wear simulation, Master's Thesis, University of Alberta, 2000.
- [3] V. K. Jain, Advanced machining processes, Allied publishers, 2009.
- [4] Standard terminology related to erosion and wear, Annual Book of Standards, Vol. 3.02, ASTM, Philadelphia.
- [5] T. S. Eyre, Wear characteristics of metals, Tribology International, 9, (1976) 203-212.
- [6] P. J. Blau, Fifty years of research on the wear of metals, Tribology International, 30, (1997) 321-331.
- [7] ASTM, Standard terminology related to erosion and wear, America Society of Testing Materials, Philadelphia, (2005) G40-05.
- [8] D. E. Alman, J. H. Tylczak, J. A. Hawk, M. G. Hebsur, Solid particle erosion behavior of an $\text{Si}_3\text{N}_4\text{-MoSi}_2$ composite at room and elevated temperatures, Materials Science and Engineering, A 261, (1999) 245-251.
- [9] D. Aquaro, E. Fontani, Erosion of ductile and brittle materials, Meccanica, 36, (2001) 651-661.

- [10] Japan society of corrosion engineering, *Erosion and Corrosion*, (1987) 6.
- [11] H. C. Meng, K. C. Ludema, *Wear models and predictive equations: their form and content*, *Wear*, 181, (1995) 443-457.
- [12] I. Finnie, *Erosion of surfaces by solid particles*, *Wear*, 3, (1960) 87-103.
- [13] J. G. A. Bitter, *A study of erosion phenomena part I*. *wear*, 6, (1963) 5-21.
- [14] J. G. A. Bitter, *A study of erosion phenomena part II*, *wear*, 6, (1963) 169-190.
- [15] I. M. Hutchings, R. E. Winter, *Particle erosion of ductile metals: a mechanism of material removal*, *Wear*, 27, (1974) 121-128.
- [16] R. E. Winter, I. M. Hutchings, *Solid particle erosion studies using single angular particles*, *Wear*, 29, (1974) 181-194.
- [17] I. M. Hutchings, R. E. Winter, J. E. Field, *Solid particle erosion of metals: the removal of surface material by spherical projectiles*. *Proceedings of the Royal Society of London A: Mathematical, Physical and Engineering Sciences*. Vol. 348, No. 1654, The Royal Society, 1976.
- [18] A. V. Levy, *The platelet mechanism of erosion of ductile metals*, *Wear*, 108, (1986) 1-21.
- [19] G. P. Tilly, *A two stage mechanism of ductile erosion*. *Wear*, 23, (1973) 87-96.
- [20] K. Shimizu, T. Noguchi, H. Seitoh, E. Murakami, *FEM analysis of the dependency on impact angle during erosive wear*, *Wear*, 233, (1999) 157-159.
- [21] K. Shimizu, T. Noguchi, H. Seitoh, M. Okada, Y. Matsubara, *FEM analysis of erosive wear*, *Wear*, 250, (2001) 779-784.
- [22] K. Shimizu, T. Noguchi, M. Okada, *FEM analysis of the dependency on angle during erosive wear for cast iron*, *Japan Foundry Engineering Society, Journal of Japan Foundry Engineering (Japanese Journal)*, 73, (2001) 362-366.
- [23] J. F. Molinari, M. Ortiz, *A study of solid-particle erosion of metallic targets*, *International Journal of Impact Engineering*, 27, (2002) 347-358.
- [24] D. Griffin, A. Daadbin, S. Datta, *The development of a three-dimensional finite element model for solid particle erosion on an alumina scale/MA956 substrate*, *Wear*, 256, (2004) 900-906.
- [25] M. S. ElTobgy, E. Ng, M. A. Elbestawi, *Finite element modeling of erosive wear*,

- International Journal of Machine Tools and Manufacture, 45, (2005) 1337-1346.
- [26] D. Aquaro, E. Fontani, Models of erosion analysis for brittle and ductile materials, Proceedings of WTC 2001 2nd World Tribology Congress, 2001.
- [27] D. Aquaro, Erosion due to the impact of solid particles of materials resistant at high temperature, *Meccanica*, 41, (2006) 539-551.
- [28] Y. F. Wang, Z. G. Yang, Finite element model of erosive wear on ductile and brittle materials, *Wear*, 265, (2008) 871-878.
- [29] Z. G. Liu, S. Wan, V. B. Ngye, A numerical study on the effect of particle shape on the erosion of ductile materials, *Wear*, 313, (2014) 135-142.
- [30] M. Takaffoli, M. Papini, Numerical simulation of solid particle impacts on Al6061-T6 part I: Three-dimensional representation of angular particles, *Wear*, 292, (2012) 100-110.
- [31] M. Takaffoli, M. Papini, Numerical simulation of solid particle impacts on Al6061-T6 Part II: Materials removal mechanisms for impact of multiple angular particles, *Wear*, 296, (2012) 648-655.
- [32] M. Takaffoli, M. Papini, Material deformation and removal due to single particle impacts on ductile materials using smoothed particle hydrodynamics, *Wear*, 274, (2012) 50-59.
- [33] V. Hadavi, M. Papini, Numerical modeling of particle embedment during solid particle erosion of ductile materials, *Wear*, 342, (2015) 310-321.
- [34] Y. F. Wang, Z. G. Yang, A coupled finite element and meshfree analysis of erosive wear, *Tribology international*, 42, (2009) 373-377.
- [35] Y. Gong, Z. G. Yang, Y. F. Wang, Impact simulation on ductile metal pipe with polymer coating by a coupled finite element and meshfree method, *Journal of failure analysis and prevention*, 12, (2012) 267-272.
- [36] Khaled Elalem, D. Y. Li, Dynamical simulation of an abrasive wear process, *Journal of computer-aided materials design*, 6, (1999) 185-193.
- [37] Q. Chen, D. Y. Li, Computer simulation of solid particle erosion, *Wear*, 254, (2003) 203-210.
- [38] Q. Chen, D. Y. Li, Computer simulation of solid-particle erosion of composite

- materials, *Wear*, 255, (2003) 78-84.
- [39] Q. Chen, D. Y. Li, Computer simulation of erosion–corrosion of a non-passive alloy using a micro-scale dynamic model, *Materials Science and Engineering*, A369, (2004) 284-293.
- [40] J. Hu, D. Y. Li, R. Llewellyn, Computational investigation of microstructural effects on abrasive wear of composite materials, *Wear*, 259, (2005) 6-17.
- [41] J. Hu, D. Y. Li, R. Llewellyn, Synergistic effects of microstructure and abrasion condition on abrasive wear of composites—A modeling study, *Wear*, 263, (2007) 218-227.
- [42] Q. Chen, D. Y. Li, Bruce Cook, Is porosity always detrimental to the wear resistance of materials?—A computational study on the effect of porosity on erosive wear of TiC/Cu composites, *Wear*, 267, (2009) 1153-1159.
- [43] D. Y. Li, Q. Chen, Bruce Cook, A further simulation study on the dual role of porosity in solid-particle erosion of materials, *Wear*, 271, (2011) 1325-1330.
- [44] Chenxin. Ouyang, Shigen. Zhu, D. Y. Li, Experimental and simulation studies on the solid-particle erosion of WC-MgO composites, *Tribology Letters*, 52, (2013) 501-510.
- [45] M. Junkar, B. Jurisevic, M. Fajdiga, M. Grah, Finite element analysis of single-particle impact in abrasive water jet machining, *International Journal of Impact Engineering*, 32, (2006) 1095-1112.
- [46] Naresh Kumar, Mukul Shukla, Finite element analysis of multi-particle impact on erosion in abrasive water jet machining of titanium alloy, *Journal of computational and applied mathematics*, 236, (2012) 4600-4610.
- [47] Akbar Jafari, Vahid Saljooghi Nezhad, Employing DEM to study the impact of different parameters on the screening efficiency and mesh wear, *Powder Technology*, 297, (2016) 126-143.
- [48] Markus Varga, Christoph Goniva, Karl Adam, Ewald Badisch, Combined experimental and numerical approach for wear prediction in feed pipes, *Tribology International*, 65, (2013) 200-206.
- [49] M. Y. Zang, Z. Lei, S. F. Wang, Investigation of impact fracture behavior of

automobile laminated glass by 3D discrete element method, *Computational Mechanics*, 41, (2007) 73-83.

[50] L. Zhou, M. Y. Zang, An approach to combining 3D discrete and finite element methods based on penalty function method, *Computational Mechanics*, 46, (2010) 609-619.

[51] W. Gao, M. Y. Zang, W. Xu, An approach to freely combining 3D discrete and finite element methods, *International Journal of Computational Methods*, 11, (2014) 1350102.

[52] W. Gao, Y. Q. Tan, M. Y. Zang, A cubic arranged spherical discrete element model, *International Journal of Computational Methods*, 11, (2014) 1350102.

Chapter 2

Experiments

2.1 Introduction

In this chapter, experiments for this thesis are described. The specimens, apparatus, and experimental methods are given in detail. In order to compare experimental results and simulation results conveniently, experimental results are not given in this chapter, but will be given in the following chapters successively.

2.2 Materials

Three kinds of common steel were used as test materials in the works of this thesis, they are spheroidal graphite cast iron (hereinafter FCD in chapter 3 and FDI in chapter 4), spheroidal carbide cast iron (hereinafter SCI) and mild steel JIS SS400 (hereinafter SS400). The reason to choose these 3 kinds of material is that the material matrix of FCD (or FDI) and SCI are similar to SS400, so FCD (or FDI) can be seen as combination of matrix and spheroidal graphite, and SCI can be seen as combination of matrix and spheroidal carbide, therefore it is convenient to compare the results of whether spheroidal graphite or spheroidal carbide presents or not, and how the spheroidal graphite or spheroidal carbide influences erosion performances of steels. The chemical compositions of FCD and SCI are listed in Table 2.1, chemical compositions and mechanical properties of FDI and SS400 are listed in Table 2.2. Photographs of microstructure for FCD and SCI are shown in Fig. 2.1. Test specimens were manufactured as cuboid with dimension of 50mm×50mm×10mm, test surfaces were ground to make roughness reach to Ra0.2mm. Appearance of specimen is shown in Fig. 2.2.

Two kinds of shapes of steel grits were used as impact particles, they were spherical grits and angular grits. The average diameter of these two kinds of steel grits

were both 700 μm , the hardness of steel grits were 420Hv0.01. The photographs of steel grits are shown in Fig. 2.3.

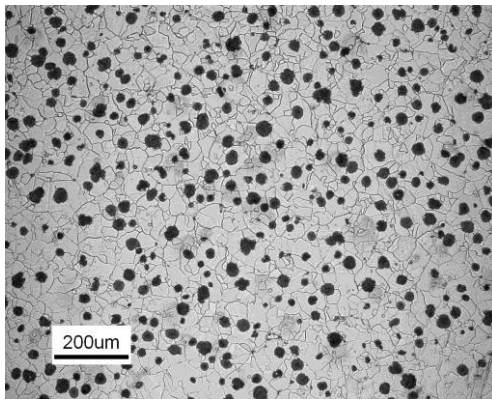
Table 2.1 Chemical compositions (mass%) of FCD and SCI

	C	Si	Mn	Mo	V	Fe	others
FCD	3.75	2.15	0.22	—	—	Bal.	P, S
SCI	2.79	0.96	0.54	3.06	12.7	Bal.	P, S

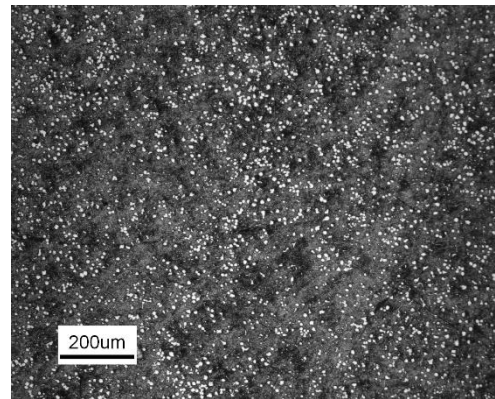
Table 2.2 Chemical composition (mass%) and mechanical properties of FDI and SS400 ^a

	C	Si	Mn	P	S	Cu	Mg	σ_B	φ	HB
FDI	3.75	2.08	0.34	0.011	0.007	0.04	0.037	400	25.8	140
SS400	0.12	0.13	0.46	0.022	0.028	—	—	491	19.7	150

^a σ_B : Tensile strength (MPa); φ : Elongation (%); HB: Brinell hardness;



(a) FCD



(b) SCI

Fig. 2.1 Microstructure of FCD and SCI

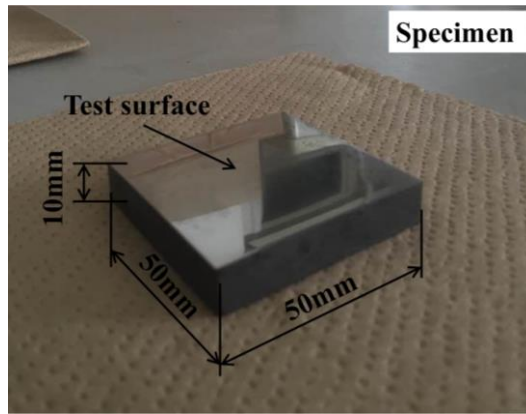
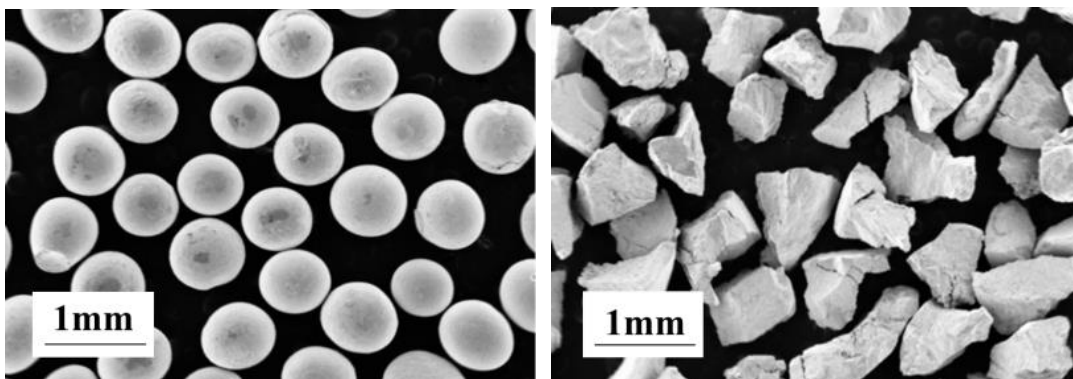


Fig. 2.2 Appearance of specimen



(a) Spherical grits

(b) Angular grits

Fig. 2.3 Appearance of impact particles

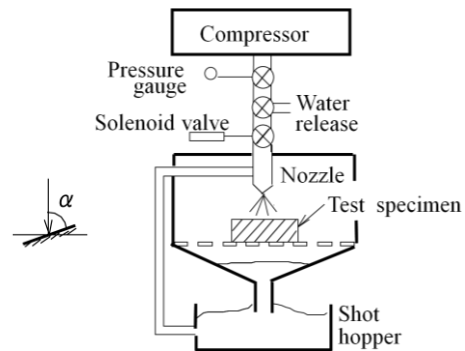
2.3 Experimental method

2.3.1 Apparatus

Experiments were carried out by using blasting machine, whose photograph and schematic view is shown in Fig. 2.4. During tests, compressor increased the air pressure up to 5kgf/cm^2 , forming air flow with velocity of 100m/s , impact particles entrained in air flow were ejected from nozzle, velocity of impact particles were measured as 20m/s . Specimen was mounted on the stage of blasting machine, different impact angles can be got by adjusting the tilting direction of stage. The photograph of test stage is shown in Fig. 2.5.



(a) Photograph



(b) Schematic view

Fig. 2.4 Blasting machine

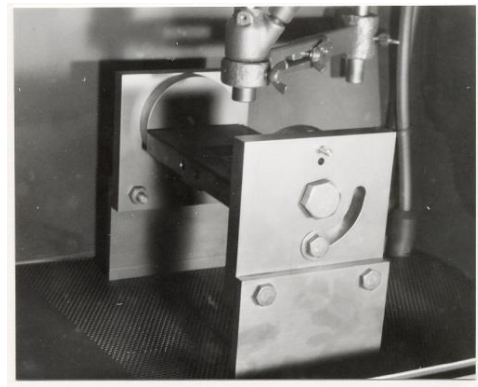
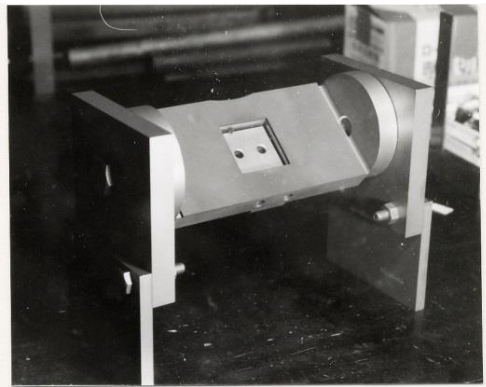


Fig. 2.5 Test stage

2.3.2 Erosion test

In erosion test, specimen was impacted by a large number of particles under a duration time. Erosion test were conducted at impact angles ranging from 10deg. to 90deg. in increment of 10deg.. The erosion test duration was 3600s and the amount of impact particles was 2kg/test. All the tests were conducted under room temperature.

Erosion rate was used as assessment. Mass loss for each specimen was weighed using an electronic scale. It's more accurate to evaluate material loss by volumetric loss than by mass loss because specimens have different densities. Erosion rate was calculated using following formulas [1-2],

$$\text{Volumetric loss per second (cm}^3\text{/s)} = \frac{\text{mass loss per second (g/s)}}{\text{average density of specimen (g/cm}^3\text{)}} \quad (2-1)$$

$$\text{Erosion rate (cm}^3\text{/kg)} = \frac{\text{Volumetric loss per second (cm}^3\text{/s)}}{\text{mass amount of solid particles per second (kg/s)}} \quad (2-2)$$

2.3.3 Single particle impact test

In this kind of test, specimen was impacted by single particle under three impact angles of 30deg., 60deg. and 90deg.. After test, the indentation depths of craters under these 3 impact angles were measured using microscope (VHX-2000, KEYENCE, Japan). 10 different indentation depths of craters were measured and then the mean value of these indentation depths were calculated and used for discussion in the following chapters.

2.4 Summarization

In this chapter, experiments are introduced in detail. The experimental results will be given successively in the following chapters and used as verification for simulation results.

References

- [1] Xinba Yaer, Kazumichi Shimizu, Hideto Matsumoto, Tadashi Kitsudo, Tadashi Momono, Erosive wear characteristics of spheroidal carbides cast iron, *Wear*, 264, (2008) 947-957.
- [2] K. Shimizu, T. Naruse, Y. Xinba, K. Shimizu, K.Minami, H. Matsumoto, Erosive wear properties of high V–Cr–Ni stainless spheroidal carbides cast iron at high temperature, *Wear*, 267, (2009) 104-109.

Chapter 3

Impact angle dependence of erosion for spheroidal carbide cast iron

3.1 Introduction

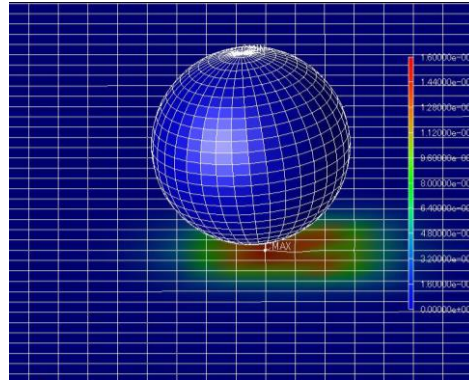
In this chapter, 3D single particle impact model for spheroidal carbide cast iron (SCI) was built, spheroidal graphite cast iron (FGI) was also built and used as comparative material. The impact angle dependence of erosion was discussed from viewpoint of stress and equivalent plastic strain on the surface of impacted material.

3.2 FEM analysis

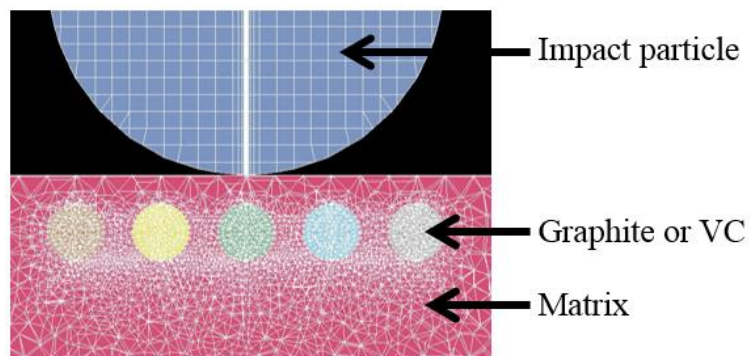
The 3D single particle impact FEM models were established using LS-DYNA 971 (Livermore Software Technology Corporation, Livermore, CA, USA), which is suitable for contact problems. Simulations of single particle impact (1 particle in each impact) using spherical particle were conducted. The FEM model is shown in Fig. 3.1. The velocity of impact particle was set as 20m/s, equaling to the actual velocity of impact particles in erosion tests. Simulation time was set as 0.01ms, target material was built as 10×10×10mm. Material parameters were set according to the mechanical properties of spheroidal carbide cast iron (SCI) and spheroidal graphite cast iron (FGI). In the simulation, diameters of spheroidal carbide (VC) and spheroidal graphite were set as 100μm, they were assigned in a line in the target material with same adjacent interval. Sphere with diameter 700μm was built as impact particle, impact angle were changed from 10deg. to 90deg. in increment of 10deg.. Because impact particles have no deformation approximately during erosion, the impact particle was set as rigid body, but target material is still set as elastic material. The material parameters of impact particle and target material are listed in Table 3.1 [1, 2].

The tests of single particle impact were also conducted to verify the simulation results. The results of tests and simulation were compared and verified through

discussing the correlation of crater depths gotten by simulation and test.



(a) Appearance of 3D model



(b) Cross sectional view of 3D model

Fig. 3.1 FEM model

Table 3.1 Material parameters for simulation [1, 2]

	SCI		FCD		Impact particle
	Target material	Carbide(VC)	Target material	Graphite	
Mass density, kg/mm ³	8.0×10 ⁻⁶	1.5×10 ⁻⁵	8.0×10 ⁻⁶	1.6×10 ⁻⁶	8.0×10 ⁻⁶
Young's modulus, GPa	200	530	161	7	210
Poission ratio	0.30	0.22	0.25	0.10	0.3
Yield stress, MPa	500	6000	230	30	—

3.3 Results

3.3.1 Simulation results

The craters of single particle impact simulation under impact angle 30deg. are shown in Fig. 3.2. It is found that along the impact direction, tiny material piled up at the color change region from blue to red, which were in agreement with the phenomenon of tiny pile-up material on specimens due to rotation of impact particle at impact moment in tests. The simulation results under 3 impact angles of 30deg., 60deg. and 90deg. are shown in Fig. 3.3. It is found that surface deformation occurred at all target materials, and it is also found that obvious deformation occurred on spheroidal graphite, but no deformation occurred on spheroidal carbide.

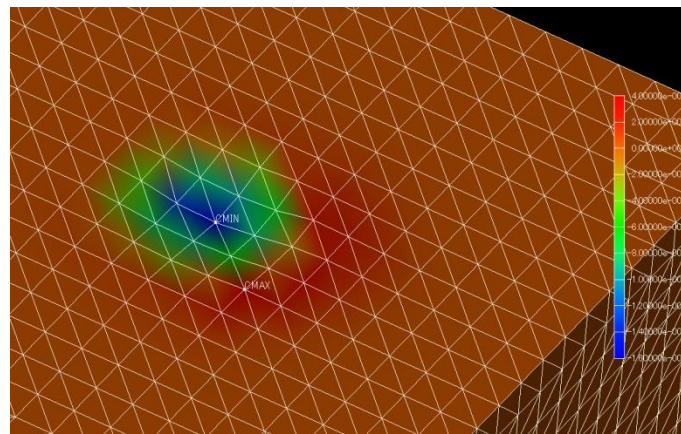
The indentation depth of craters from simulation under 3 impact angles of 30deg., 60deg. and 90deg. were measured. The relationship between simulation time and the indentation depth at the deepest point on target material after simulation were shown in Fig. 3.4. In Fig. 3.4, horizontal axis is simulation time (From the moment that impact particle contacted with target material to the moment that impact particle entirely departed away from target material), vertical axis is indentation depth. It is found that indentation became deeper along the sequence of impact angle 30deg., 60deg. and 90deg.. In addition, it is also found that deformation recovered a little at all impact angles.

3.3.2 Results of single particle impact tests

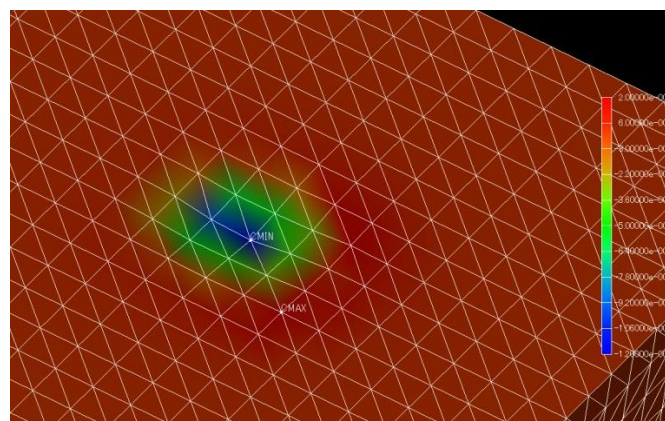
The appearances of crater and indentation depth after single particle impact tests were observed and measured using microscope. The photographs of typical craters are shown in Fig. 3.5. It is found that tiny material piled up on specimens at impact angles 30deg. and 60deg., which is in agreement with the simulation results. The indentation depth of spheroidal graphite cast iron became deeper with increasing of impact angle, they were 7.62 μm , 14.88 μm and 18.70 μm at impact angle 30deg., 60deg. and 90deg. respectively. Similar tendency were also found on the indentation depth of spheroidal carbide cast iron, they are 3.00 μm , 10.38 μm and 15.48 μm at impact angle 30deg., 60deg. and 90deg. respectively.

3.3.3 Discussion of correlation between test results and simulation results

The correlation diagram between indentation depths from simulation in section 3.3.1 and those from single particle impact tests in section 3.3.2 are shown in Fig. 3.6. The correlation coefficient of indentation depth between simulation results and test results on FCD and SCI were calculated, both are 0.99, close to 1, demonstrating strong correlation between simulation results and test results. Therefore, in the following section, impact angle dependence of erosion are explained from view point of equivalent plastic strain and stress from single particle impact simulation.



(a) FCD



(b) SCI

Fig. 3.2 3D observation of indentation depth on target material surface for FEM model

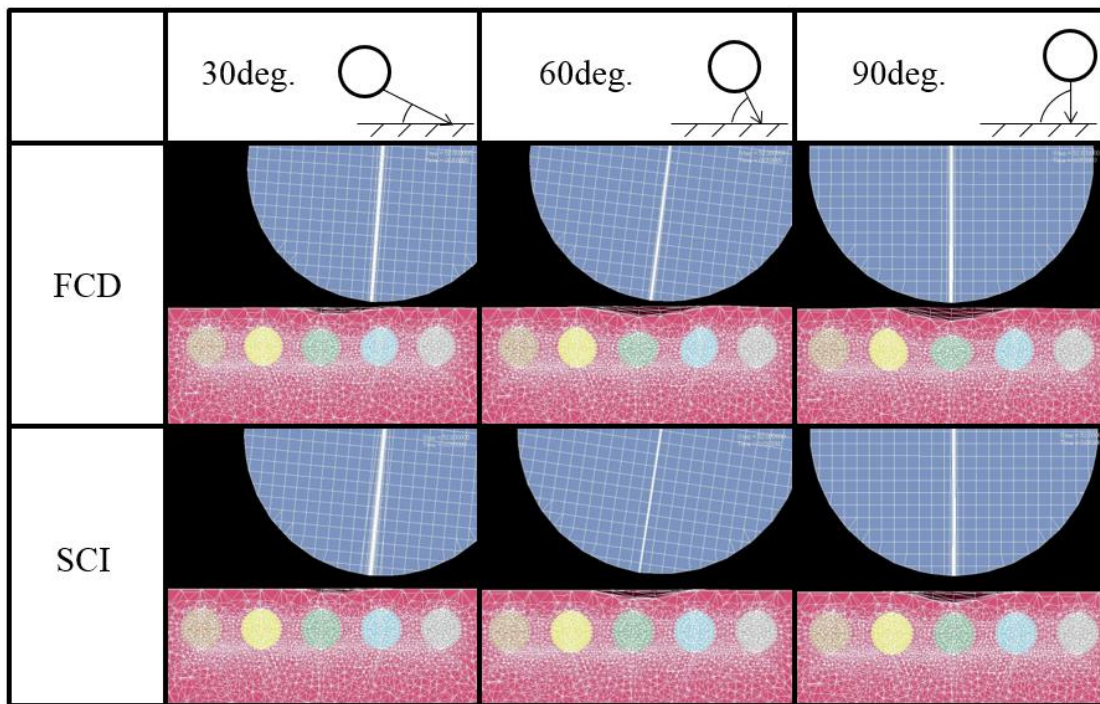


Fig. 3.3 Results of 3D FEM simulation for single particle impact

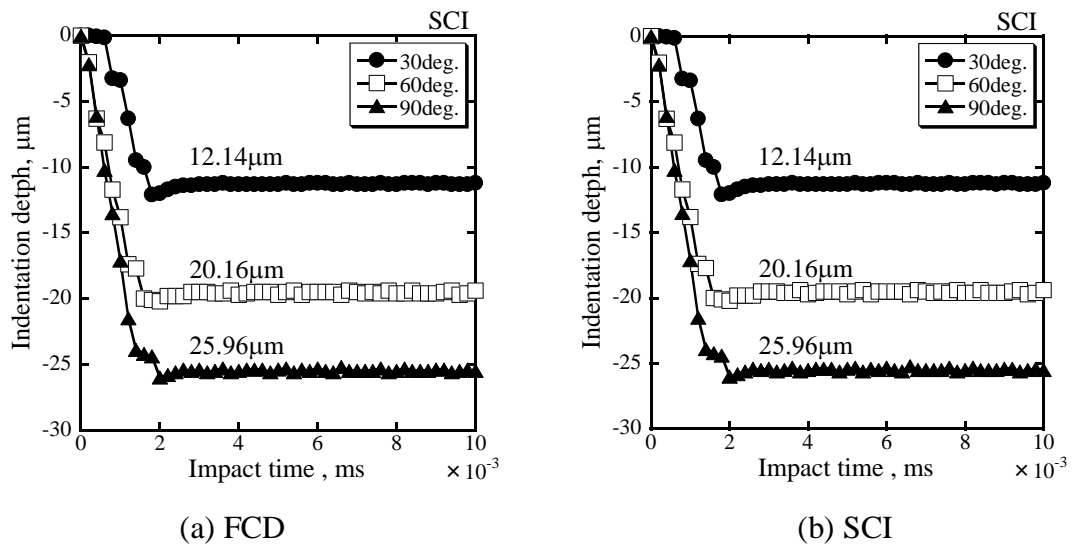
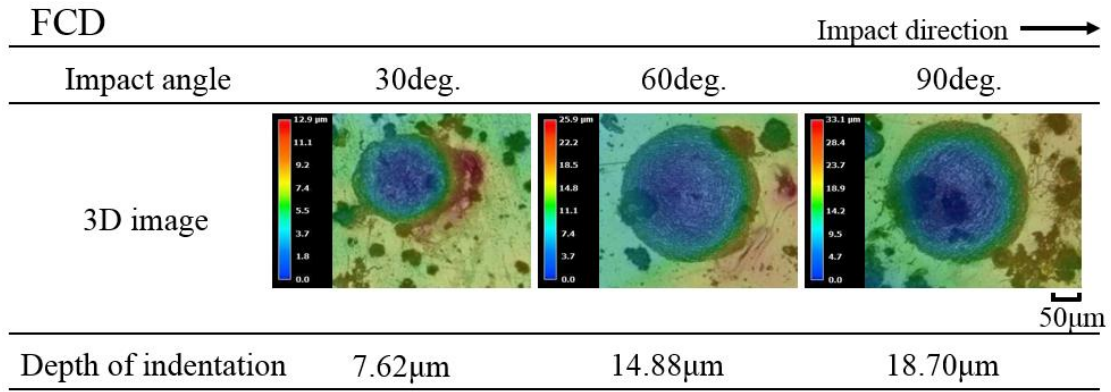
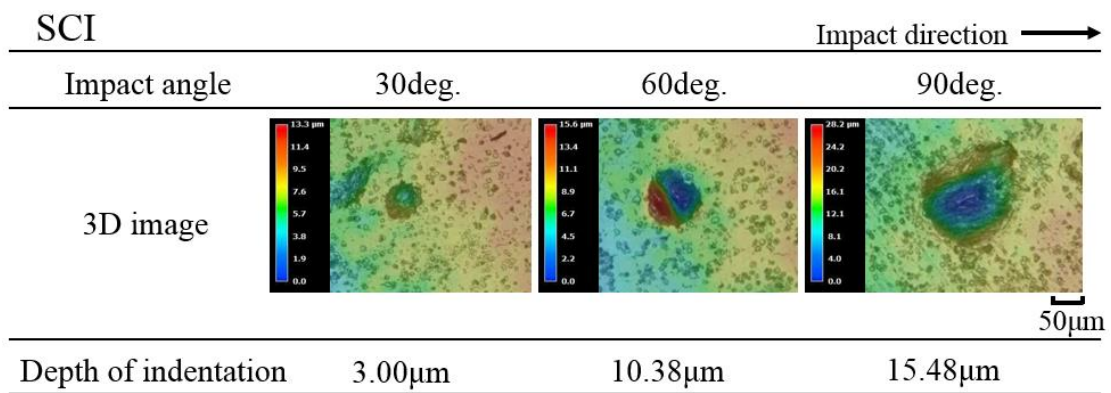


Fig. 3.4 Indentation depth as function of impact time for specimens



(a) FCD



(b) SCI

Fig. 3.5 Observation of indentation on specimens in single particle impact tests

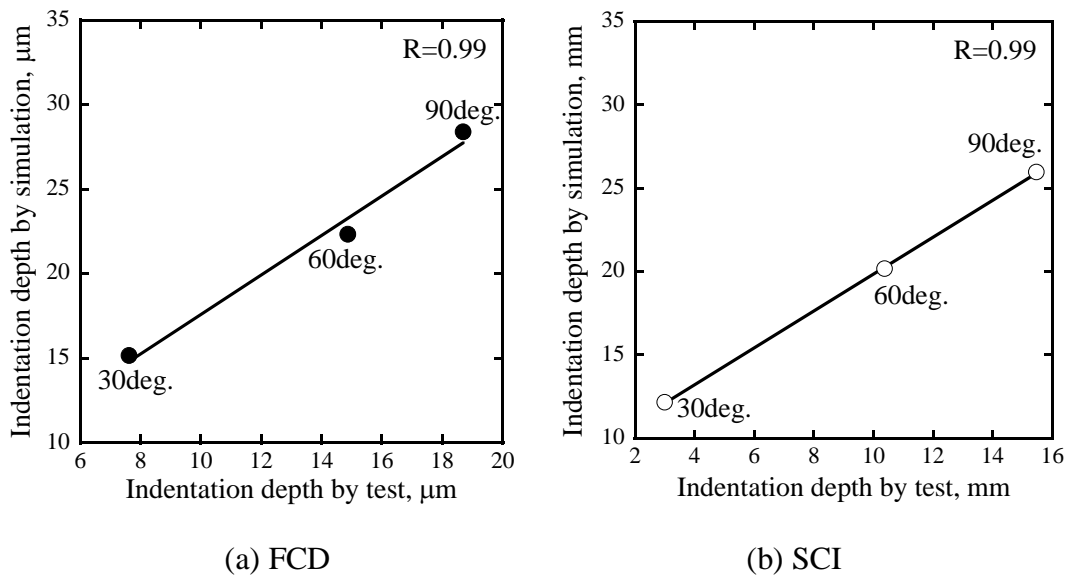


Fig. 3.6 Correlation diagram of indentation depth between simulation results and test results

3.4 Discussion

3.4.1 Discussion of von mises stress

According to shear strain energy theory when the shear strain energy in the actual case exceeds shear strain energy at the time of failure the material fails. Von mises stress is in proportion to the square root of shear strain energy. Von mises stress is expressed by a combination of three principal stress, so it can be used as an evaluation of mechanical state for iron and steel materials. The Von mises stress by simulation are shown in Fig. 3.7. It is found that, as for spheroidal graphite cast iron, obvious deformation occurred on spheroidal graphite, obvious von mises stress also occurred at thick places of target materials besides material surface, and von mises stress on spheroidal graphite were lower than those on matrix around spheroidal graphite. Meanwhile, as for spheroidal carbide cast iron, von mises stress on spheroidal carbide were higher than those on matrix around spheroidal carbide, which is because the yield stress of spheroidal carbide is very high, up to around 6000MPa.

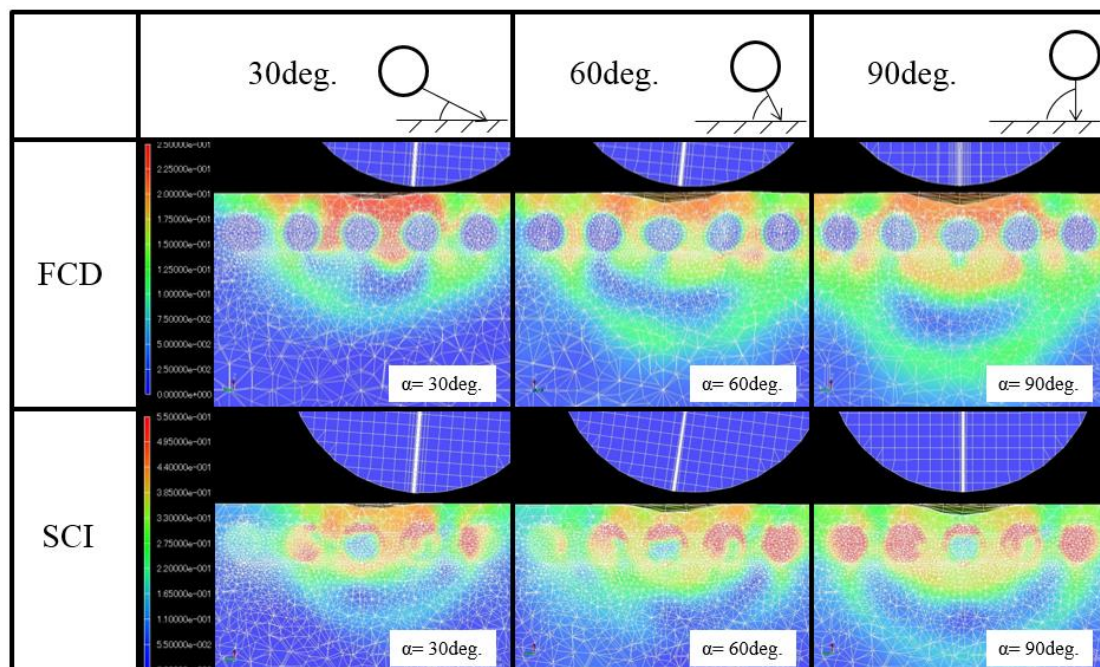


Fig. 3.7 Von mises stress distribution of specimens by FEM simulation

3.4.2 Discussion of impact angle dependence based on equivalent plastic strain

Erosion is a phenomena of material deformation and loss caused by repeated impact of solid particles, it can be seen as the results of deformation accumulation on material surface by single particle impact. So impact angle dependence of erosion can be explained through equivalent plastic strain on material surface. The cross sectional view of equivalent plastic strain distribution on spheroidal graphite cast iron and spheroidal carbide cast iron under impact angles of 30deg., 60deg. and 90deg. are shown in Fig. 3.8. It is found that equivalent plastic strain distribution of 90deg. is axisymmetric, and equivalent plastic strain of 30deg. is obvious in a small region. In addition, it is also found that equivalent plastic strain on the spheroidal graphite were larger than those on matrix around spheroidal graphite, and equivalent plastic strain on the spheroidal carbide were smaller than those on matrix around spheroidal carbide. The ratio of total equivalent plastic strain on FCD and SCI (total equivalent plastic strain on FCD and SCI were divided by total equivalent plastic strain on FCD at impact angle 90deg.) under different impact angles are shown in Fig. 3.9, and relationship between erosion rate and impact angle are shown in Fig. 3.10. It is found that both equivalent plastic strain and erosion rate increased firstly and then decreased, maximum value occurs around a higher impact angle, showing a similar tendency. In addition, it is also found that equivalent plastic strain and erosion rate of SCI changed much less at different impact angles comparing to FCD, showing that the impact angle dependence is very small. But the tendencies of both SCI curves are different, which is because the arrangement of VC in specimens for tests are much more complex than those in target material for simulation. According to discussions above, equivalent plastic strain at different impact angles can be regarded as a method to explain the features of impact angle dependence that erosion of FCD increases firstly and then decreases with maximum value occurring at a higher impact angle, and erosion of SCI changes a little at different impact angles. In other word, impact angle dependence of erosion can be approximately discussed through equivalent plastic strain of single particle impact.

The difference between impact angle of erosion for FCD and SCI is due to the

influence of spheroidal graphite and spheroidal carbide in target material. Yield strength of spheroidal carbide is much higher than that of spheroidal graphite, up to 5500MPa or higher. So it is inferred that the existence of spheroidal carbide with high yield strength in target material can largely restrain the impact angle dependence of erosion.

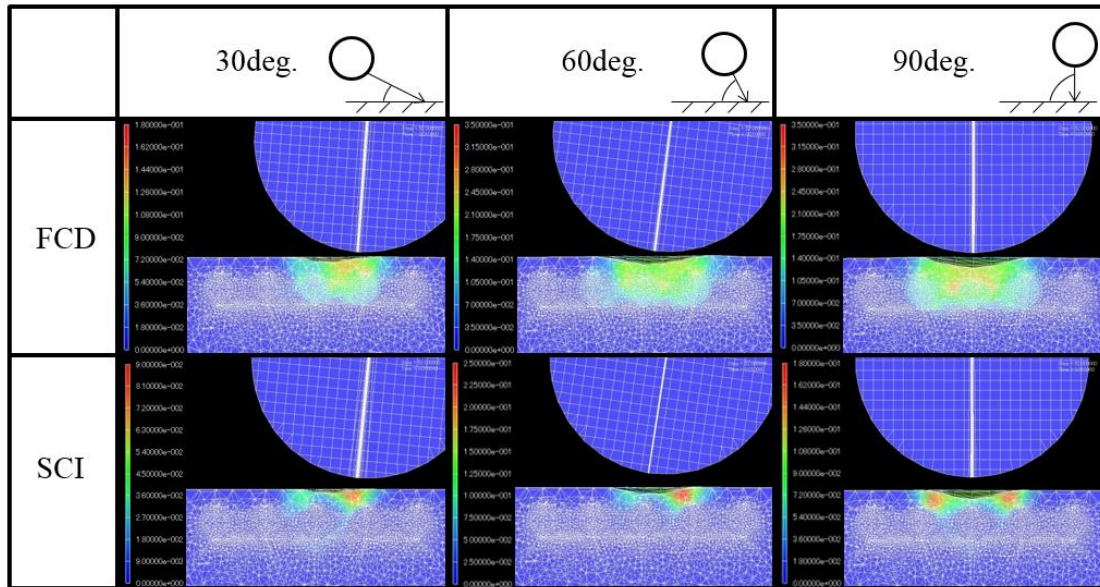


Fig. 3.8 Equivalent plastic strain distribution of specimens by FEM simulation

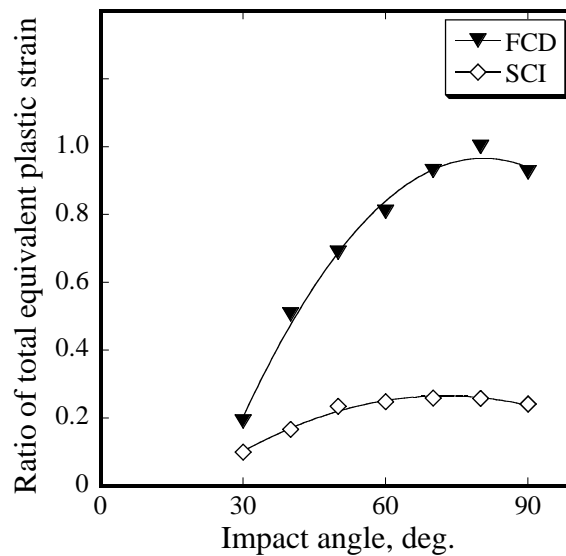


Fig. 3.9 Total equivalent plastic strain as function of impact angle for specimens

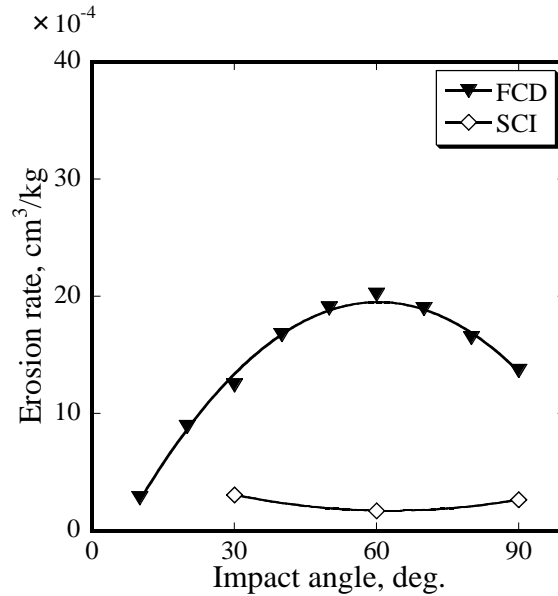


Fig. 3.10 Erosion rate as function of impact angle for specimens

3.5 Conclusions

In this chapter, 3D FEM models were built, and the impact angle dependence of erosion on spheroidal carbide cast iron were verified using simulation results from view point of stress and equivalent plastic strain.

(i) As for spheroidal graphite cast iron, obvious deformation was found on the spheroidal graphite in target material. And von mises stress in matrix was higher than that on spheroidal graphite.

(ii) As for spheroidal carbide cast iron, von mises stress on the spheroidal carbide was higher than that on the matrix around spheroidal carbide, but no deformation was found on the spheroidal carbide. The plastic deformation on spheroidal carbide cast iron was largely restrained because of the existence of spheroidal carbide with much higher yield stress comparing to spheroidal graphite in spheroidal graphite cast iron.

(iii) There are similar curves for impact angle dependence of erosion and that of equivalent plastic strain, so impact angle dependence of erosion can be explained with that of equivalent plastic strain.

References

[1] K. Shimizu, T. Noguchi, H. Seitoh, M. Okada, Y. Matsubara, FEM analysis of

erosive wear, *Wear*, 250, (2001) 779-784.

[2] Michael F. Ashby, David R. H. Jones, *Engineering materials: an introduction to their properties and applications*, Pergamon press, 31, (1980) 78.

Chapter 4

Finite element analysis of single particle impact on mild steel and spheroidal graphite cast iron

4.1 Introduction

In the previous study of our laboratory, Prof. K. Shimizu and his coworkers built FE models of single particle impact to investigate erosion mechanisms on spheroidal graphite cast iron (FDI) and mild steel SS400 [1-3]. However, there were 2 obvious shortages in the models, (i) due to 2-dimensional way, impact particles were simplified as cylinder rather than sphere, so the models were different from actual condition, (ii) only plastic strain was discussed, so the erosion mechanisms were only explained from viewpoint of deformation effect, cutting effect was not considered, therefore it was insufficient to explain the erosion mechanisms completely. Hence, the work in this chapter extended the FE models of [1-3], FE models of single particle impact on FDI and SS400 were built by 3D way, and the erosion mechanisms were explained from viewpoint considering combination of plastic strain and shear stress.

4.2 Finite element modeling

The impact process was simulated by means of explicit dynamic analysis software ANSYS/LS-DYNA. The FE models were built by using APDL (ANSYS Parametric Design Language) code to create K-file in ANSYS 15.0, and then the K-file were computed in LS-DYNA 971. The simulation time was set as 5×10^{-3} ms, time step was set as 1×10^{-4} ms.

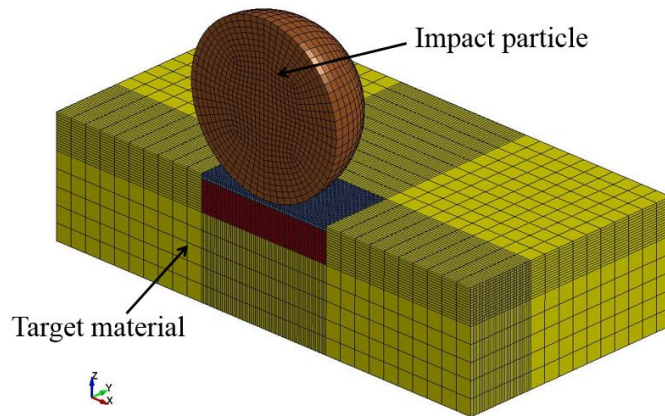
The FE models for SS400 and FDI are shown in Fig. 4.1 and Fig 4.2 respectively. Due to symmetry of whole models, only half of the models were built to improve computing speed, and y-displacement of nodes on symmetrical areas were fixed. Sphere stands for impact particle, initial velocity of impact particle was 20m/s, same

with velocity of steel grits in erosion tests. The diameter of impact particles were 700 μm , also same with average diameter of spherical steel grits in erosion tests. Impact angle ranged from 10deg. to 90deg. in increment of 10deg.. Cuboid stands for target material, the dimension of whole target material was 2mm \times 1mm \times 0.5mm. The models were meshed by using 8-node brick element solid164. The contact region on target material was meshed by finer grid, the dimension of finer grid region was 0.6mm \times 0.3mm \times 0.15mm. The horizontal and vertical edge length of each element in finer grid region was 0.01mm. All freedom degrees of nodes on the bottom and outside areas were fixed.

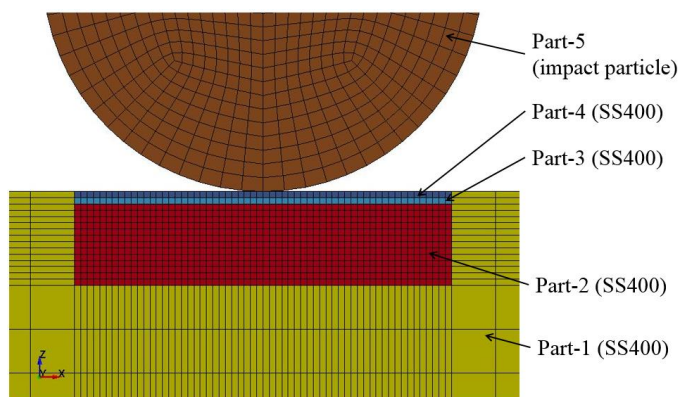
Target material of FDI was built as combination of matrix and spheroidal graphite particles. Material parameter of matrix is same with that of SS400. The diameter of spheroidal graphite particles was set as 30 μm , same with the actual average diameter of spheroidal graphite according to observation on ground surfaces of FDI specimens. Totally 39 spheroidal graphite particles were built in the models, they were arranged in two layers (layer A and layer B). The interval distance between two adjacent spheroidal graphite particles in same layer was 80 μm . The vertical distance between centers of spheroidal graphite particles in two layers was 60 μm . The arrangement of spheroidal graphite particles in layer A and layer B are shown in Fig. 4.3. Considering complexities of graphite position in real FDI, the positions of spheroidal graphite particles in this study were classified into 4 kinds, namely A-30, B-30, A-50 and B-50, which are shown in Fig. 4.4. "A" means that layer A was placed as the first layer in the model so that a graphite particle was just under impact particle. Similarly, "B" means that layer B were placed as the first layer so that 2 graphite particles were locating in two sides under impact particle. "30" or "50" means that the distance between centers of spheroidal particles in first layer and upper surface of target material was 30 μm or 50 μm .

In order to discuss simulation results of finer grid surface with different thickness conveniently, target material was divided into different parts. The parts were assigned with material according to Fig. 4.1 (b) and Fig. 4.2 (b). Material parameters were listed in Table 4.1. During simulation for FDI, although graphite is a material with

strong anisotropy, they were still set as isotropic material to improve the convergence speed and reduce the computation complexity, hourglass control needed to be switched on and hourglass coefficient was set as 0.15 to avoid “negative volume” error. Impact particles were set as rigid bodies to save CPU time. The contact between impact particle and target material was defined by using ESTS (Eroding-Surface-To-Surface), impact particle was set as master part, target material was set as slave part, both static and dynamic friction coefficient were set as 0.1.

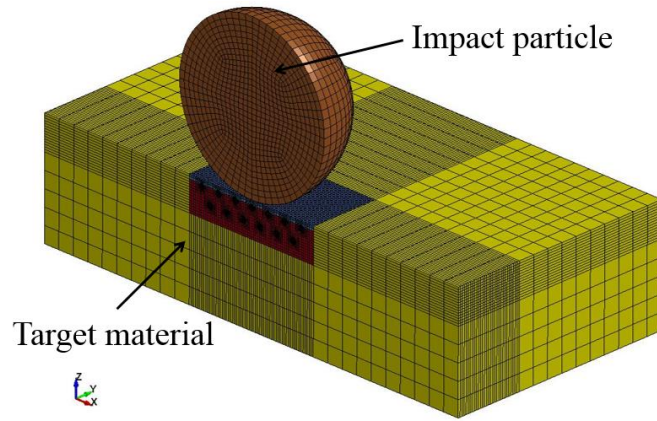


(a) Whole view

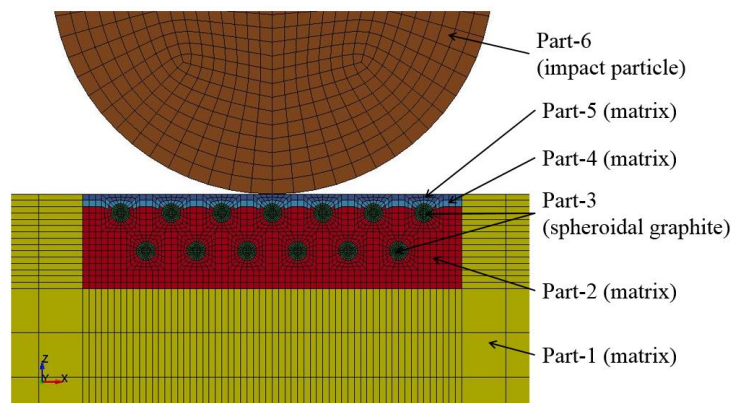


(b) View in y-direction

Fig. 4.1 FE model for SS400

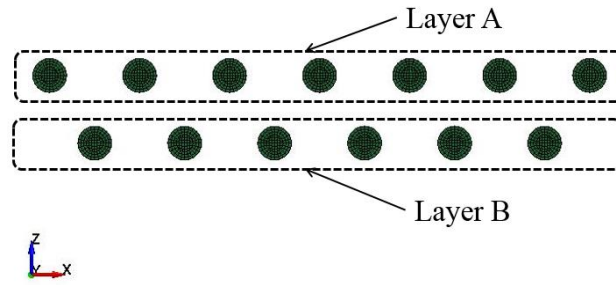


(a) Whole view

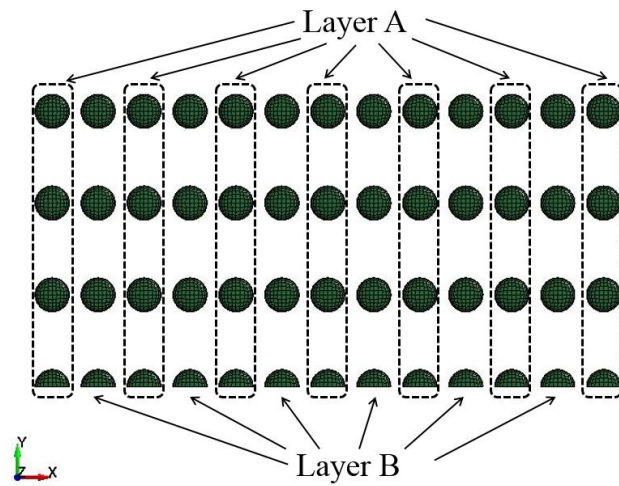


(b) View in y-direction

Fig. 4.2 FE model for FDI

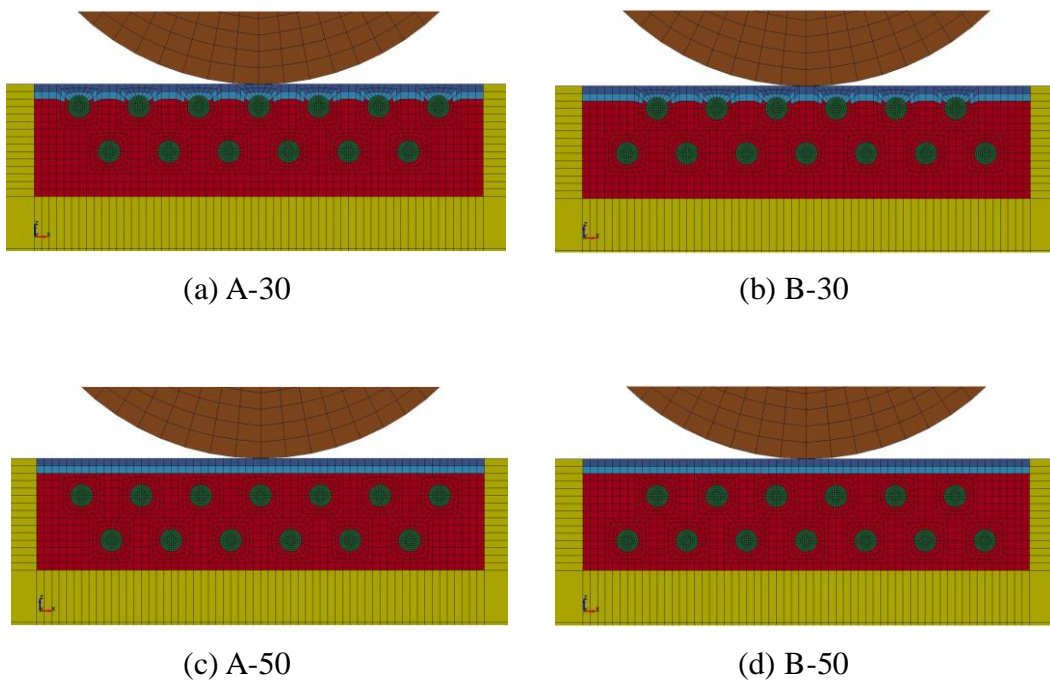


(a) View in y-direction



(b) View in z-direction

Fig. 4.3 Arrangement of spheroidal graphite particles in layer A and layer B



(a) A-30

(b) B-30

(c) A-50

(d) B-50

Fig. 4.4 Positions of spheroidal graphite particles in FDI

Table 4.1 Material Parameters

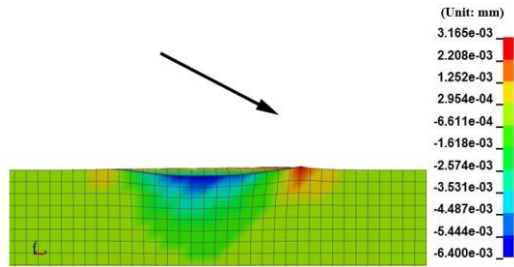
	Density (kg/m ³)	Young's Modulus (GPa)	Possion's ratio	Yield stress (MPa)
Impact Particle	8000	210	0.3	—
SS400	8000	206	0.3	491
Matrix	8000	206	0.3	491
Spheroidal graphite	2300	20	0.25	30

4.3 Results and discussion

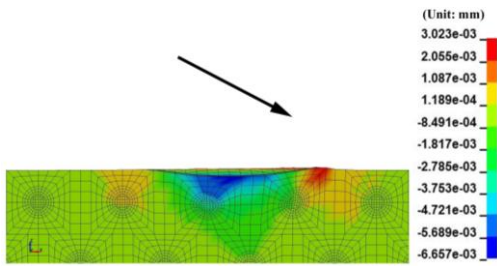
4.3.1 Crater

The distribution in z-direction at impact angle 30deg. from FE simulation is shown in Fig. 4.5. The craters at impact angle 30deg., 60deg. and 90deg. after single particle impact test is shown in Fig. 4.6. It can be seen that shapes of craters on SS400 and FDI showed same, but crater depth on FDI was apparently deeper than that on SS400.

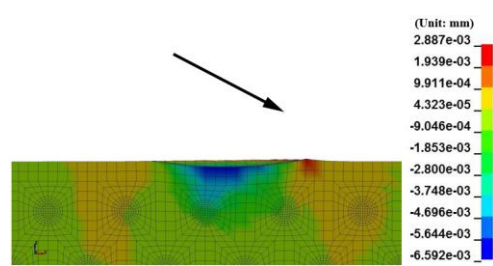
The crater depth of FDI under 4 different positions of spheroidal graphite particles was extremely close, so crater depth due to these 4 different graphite positions were not listed in detail here, but the mean values of crater depths on FDI under 4 different graphite positions were calculated and used in Fig. 4.7. Meanwhile, crater depths of 10 different craters on each specimen at impact angle 30deg., 60deg., 90deg. were measured and the mean values of these 10 crater depths at each impact angle were calculated and used in Fig. 4.7. Fig. 4.7 shows the relationships between crater depth and impact angle. It was found that crater depths increased with increasing of impact angle in the form of quadratic curve, and craters of FDI were deeper than those of SS400. That was because yield stress of graphite was much lower than that of SS400 (equivalent to matrix of FDI), so the presence of soft material graphite made craters deeper. It was also found that difference of crater depths between SS400 and FDI from FEM was larger than that from test, which was because the amounts, shapes, sizes and arrangements of graphite in actual FDI are much more complicated than FE models here, but the trends of test curves and FEM curves were so similar that it was still considered that FE results were acceptable.



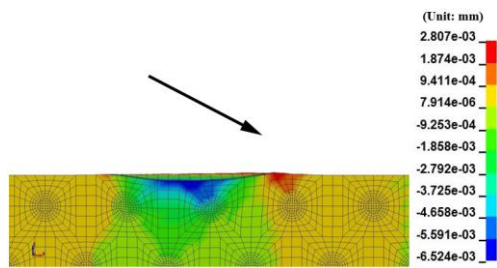
(a) SS400



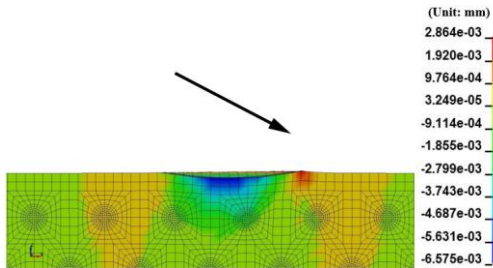
(b) FDI (A-30)



(c) FDI (A-50)



(d) FDI (B-30)



(e) FDI (B-50)

Fig. 4.5 Distribution of z-displacement at impact angle 30deg. from FE simulation

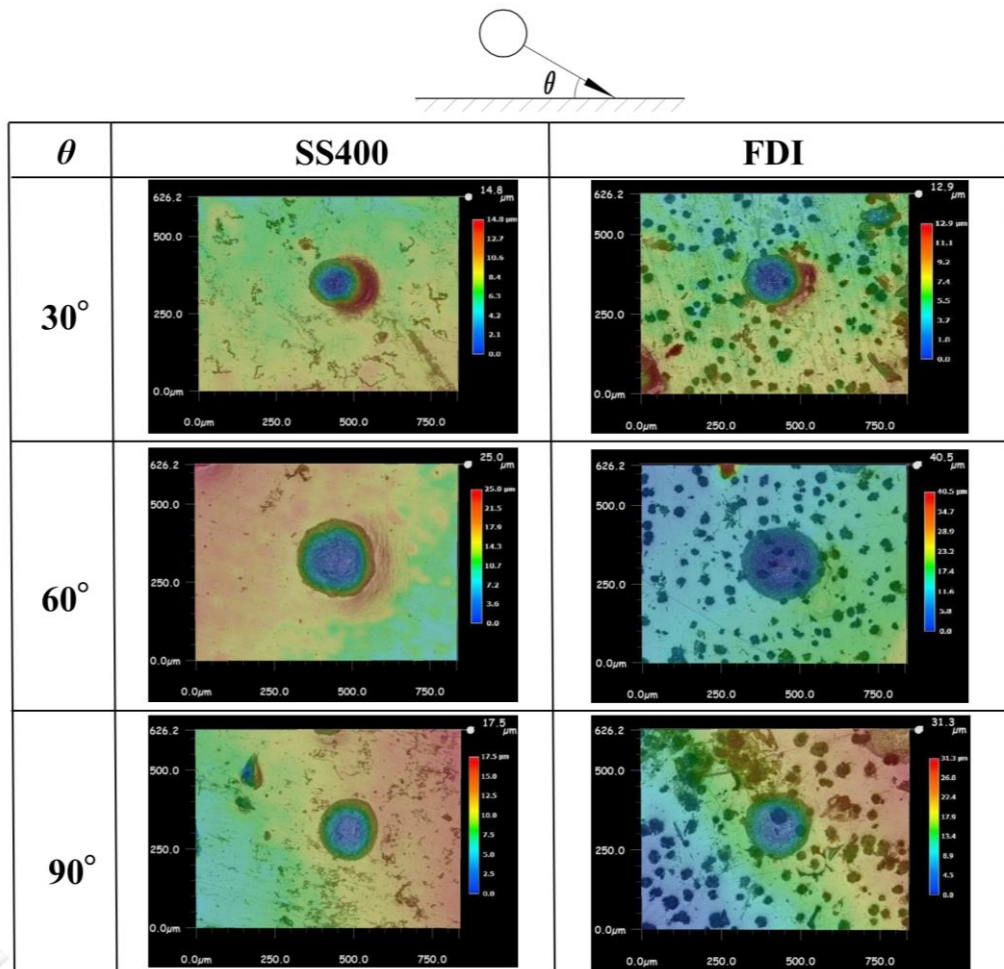


Fig. 4.6 Appearance of crater from single particle impact test

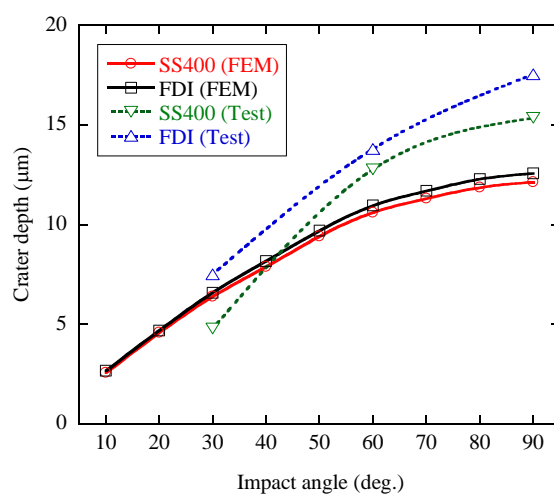


Fig. 4.7 Crater depth vs impact angle

4.3.2 Dependence of impact angle from test

The relationships between erosion rate and impact angle after erosion tests were shown in Fig. 4.8. It can be seen that erosion rate of FDI was higher than that of SS400, and maximum erosion rate occurred at impact angle 20deg. for SS400 and 60deg. for FDI, demonstrating typical dependence of impact angle for ductile material and cast iron respectively. In section 4.4.3, the dependence of impact angle are explained from FE results.

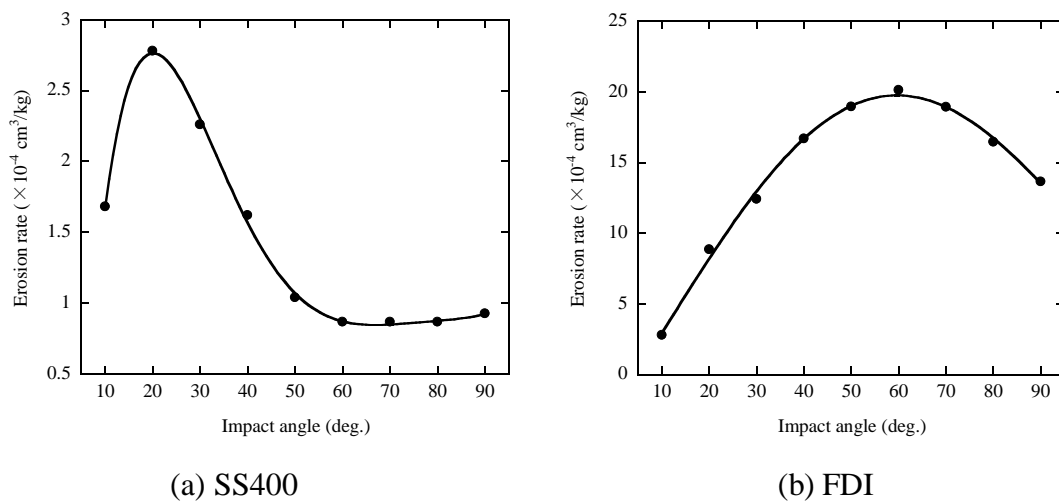


Fig. 4.8 Erosion rate vs impact angle from test

4.3.3 Dependence of impact angle from FE simulation

It is well known that erosion occurs due to the combination of deformation and cutting effect on material surface. Meanwhile, deformation effect mainly comes from plastic strain, and cutting effect mainly comes from shear stress. An example of distribution of plastic strain and shear stress for SS400 and FDI are shown in Fig. 4.9 and Fig. 4.10 respectively (impact angle is 30deg.). Erosion is occurred on the material surface, so maximum plastic strain and shear stress on material surface at the final simulation time were discussed in this section.

Distribution of plastic strain and shear stress on material surface with thickness 0~20 μm for SS400 and FDI are shown in Fig. 4.11 and Fig. 4.12 respectively (impact angle is 30deg.). Maximum plastic strain and maximum shear stress on material

surface with thickness 0~20 μm could be seen. In the same way, we could also get the maximum plastic strain and maximum shear stress at other impact angles and material surface with thickness 0~10 μm . The maximum plastic strain and maximum shear stress were used in following discussion.

Fig. 4.13 shows the relationship between plastic strain as well as shear stress and impact angle on material surfaces of SS400 and FDI (A-30) with different thickness 0~10 μm and 0~20 μm . It can be seen that plastic strain with different thicknesses was same, meaning that the maximum plastic strain occurs at areas with thickness 0~10 μm , where is extremely close to the places impacted by impact particle. Meanwhile, shear stress with different thicknesses showed a little different, shear stress of 0~20 μm is a little higher than those of 0~10 μm at some impact angles, meaning that at these impact angles maximum shear stress occurs at thickness of 10~20 μm , but the overall trends were similar and curves with thickness 0~20 μm changed more obviously. Therefore, maximum plastic strain and shear stress on material surface with 0~20 μm for SS400 and 4 different FDI models were shown in Fig. 4.14 for further discussion.

It can be seen that as for plastic strain, curves of FDI (A-30) and FDI (B-30) changed obviously at different impact angles, and curves of SS400, and FDI (A-50) and FDI (B-50) changed relatively less obviously. Meanwhile, as for shear stress, curves of FDI (A-30) and FDI (B-30) kept almost constant at different impact angles, curves of FDI (A-50) and FDI (B-50) changed a little obvious, and curve of SS400 changed more obvious. Besides, in real experiments, spheroidal graphite could be observed on the ground surfaces of FDI specimens, meaning that FDI (A-30) and FDI (B-30) were more similar to actual FDI specimens than those of FDI (A-50) and FDI (B-50). From a whole view on Fig. 4.14, as for SS400, plastic strain changed small and shear stress changed large, so shear stress plays main role on erosion of SS400. Meanwhile as for FDI, plastic strain changed large and shear stress changed small, so plastic strain plays main role on erosion of FDI.

Therefore it was inferred that shear stress and plastic strain play main role on erosion of SS400 and FDI respectively, and maximum shear stress occurred at impact angle 20deg. on SS400 and maximum plastic strain occurred at 50deg. and 80deg. on

FDI (A-30) and FDI (B-30) respectively, which agreed with erosion rate curve of SS400 and FDI in Fig. 4.8. Furthermore, except that plastic strain curve of FDI (A-50) and FDI (B-50) showed a little smaller than that of SS400, plastic strain and shear stress of FDI were all larger than those of SS400, which can explain the phenomena that erosion rate of FDI was higher than that of SS400.

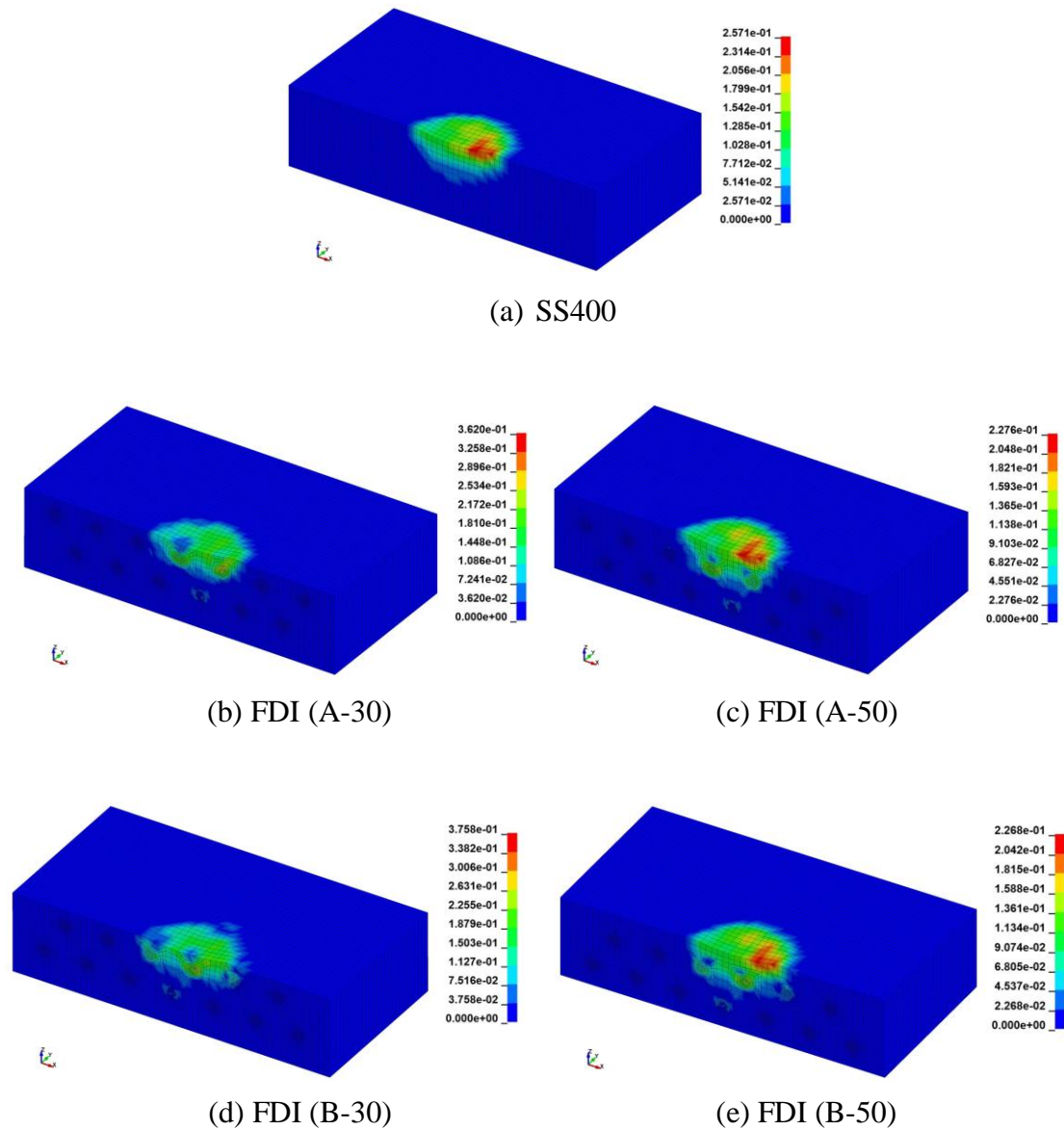
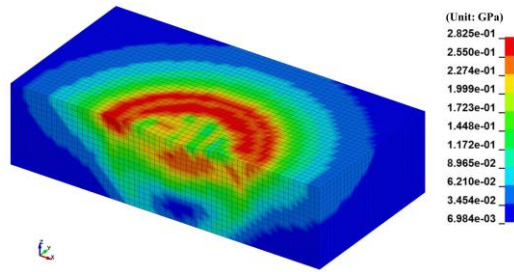
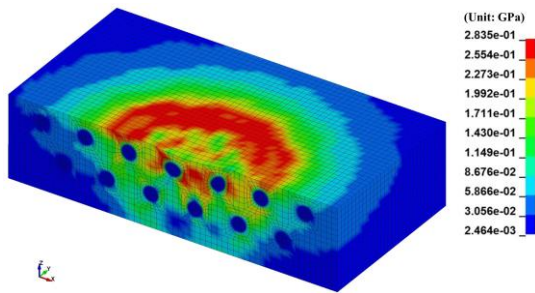


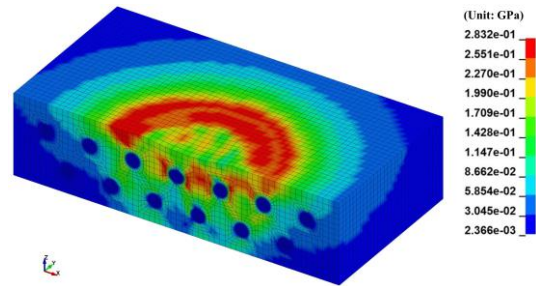
Fig. 4.9 Distribution of plastic strain at impact angle 30deg.



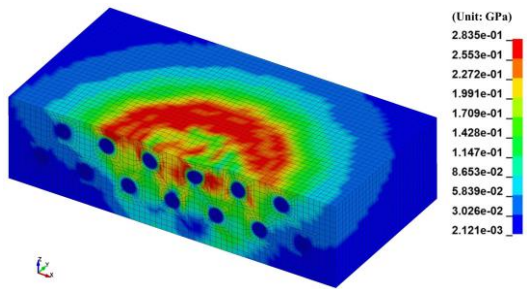
(a) SS400



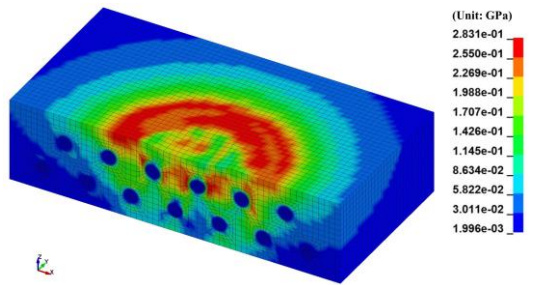
(b) FDI (A-30)



(c) FDI (A-50)

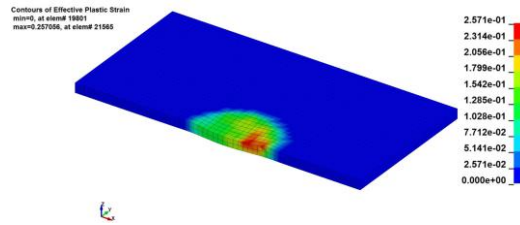


(d) FDI (B-30)

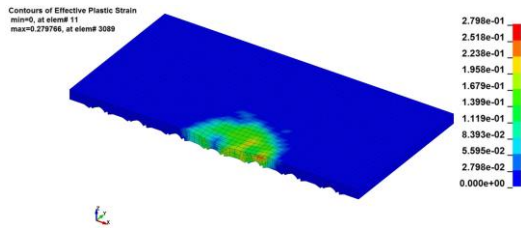


(e) FDI (B-50)

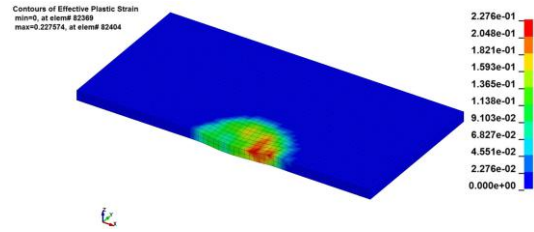
Fig. 4.10 Distribution of shear stress at impact angle 30deg.



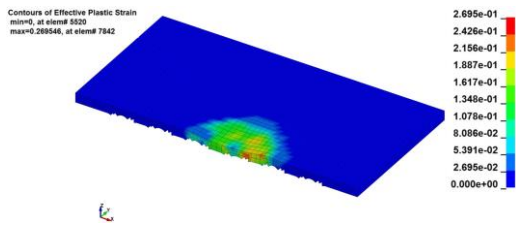
(a) SS400



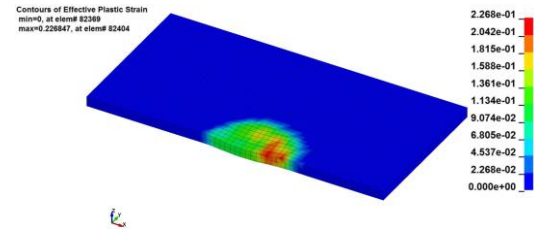
(b) FDI (A-30)



(c) FDI (A-50)



(d) FDI (B-30)



(e) FDI (B-50)

Fig. 4.11 Distribution of plastic strain on material surface with thickness 0~20 μ m at impact angle 30deg.

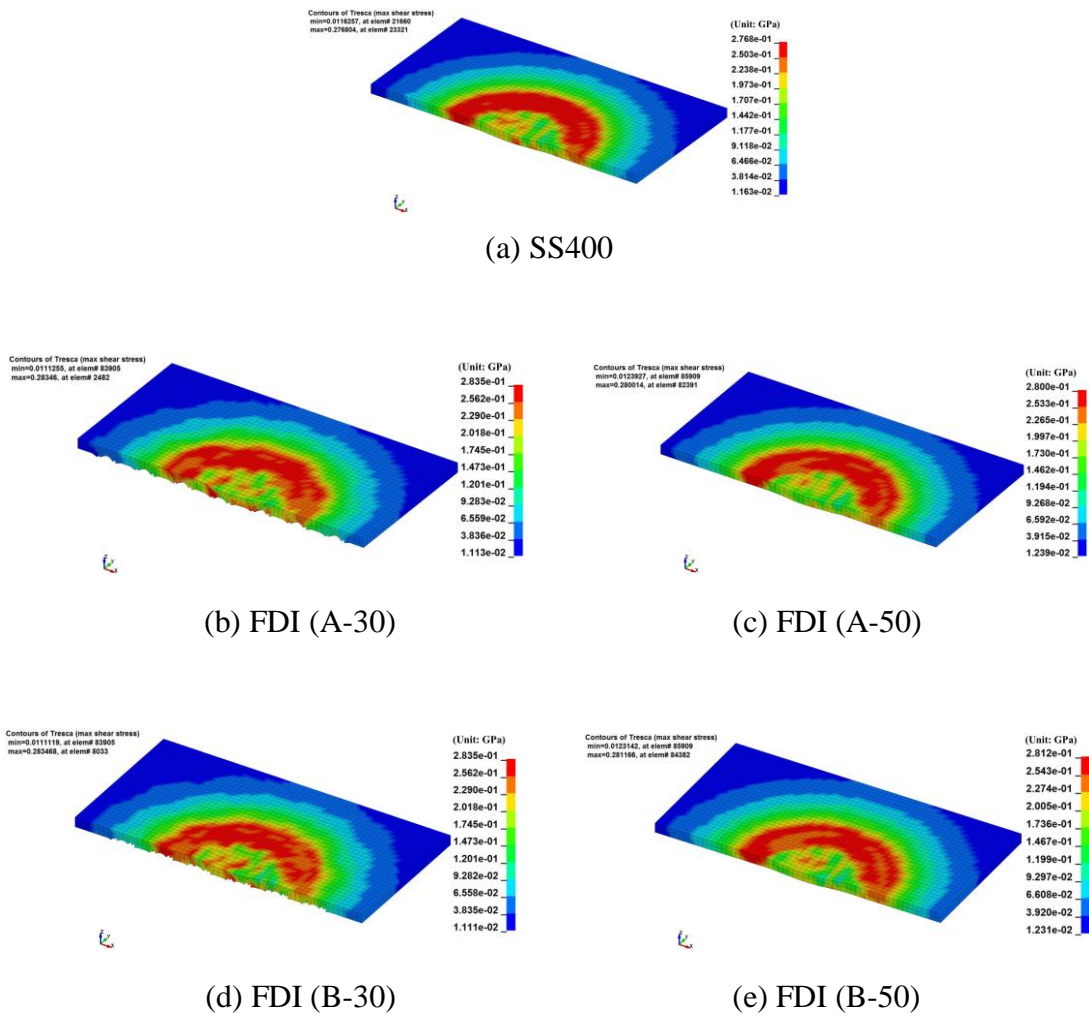


Fig. 4.12 Distribution of shear stress on material surface with thickness 0~20 μ m at impact angle 30deg.

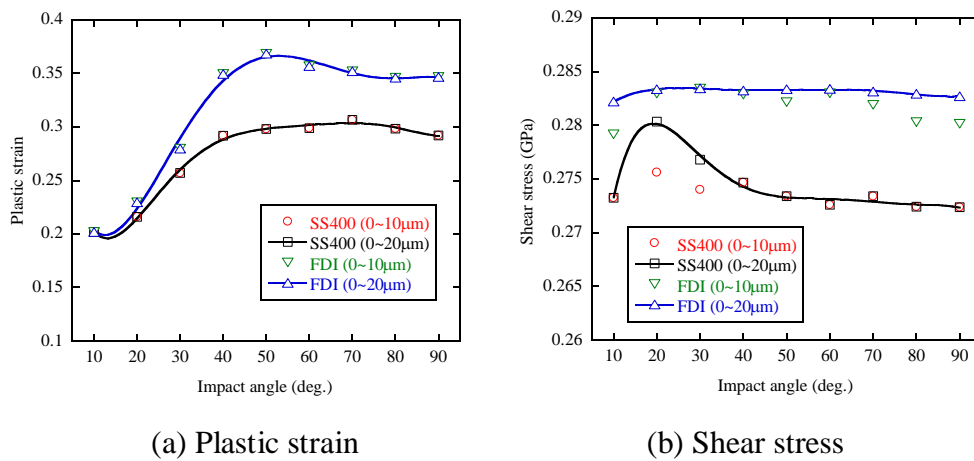


Fig. 4.13 Plastic strain and shear stress vs impact angle on material surface with different thickness of SS400 and FDI (A-30)

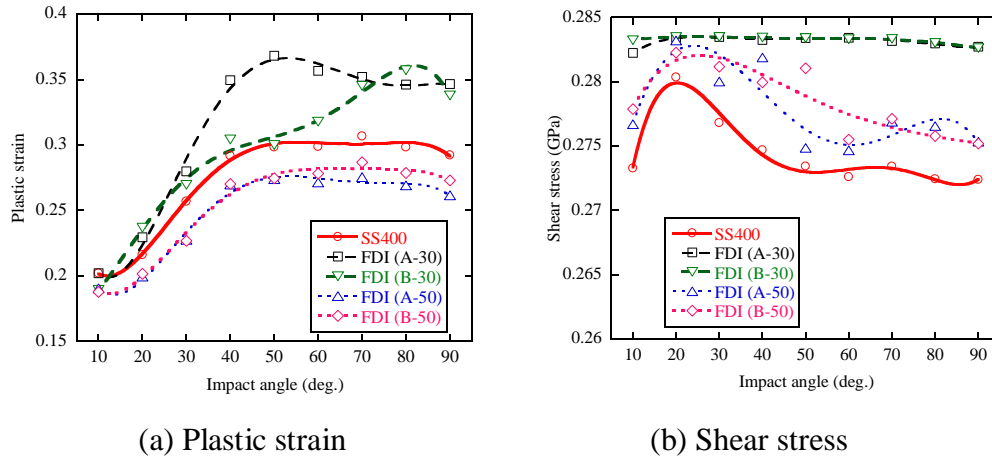


Fig. 4.14 Plastic strain and shear stress vs impact angle on material surface of SS400 and FDI with different graphite positions

4.4 Conclusions

3D FE models of single particle impact on mild steel SS400 and spheroidal graphite cast iron FDI were built. The mechanisms of erosion on SS400 and FDI were discussed.

(i) Craters of SS400 and FDI after single particle impact showed similar shapes, however, the presence of much softer material graphite made craters of FDI deeper than that of SS400.

(ii) Erosion tests indicated that erosion of FDI was higher than that of SS400, and maximum erosion occurred at impact angle 20deg. for SS400, and 60deg. for FDI respectively. Considering the combination of deformation and cutting effect, erosion tests results could be explained from viewpoint of plastic strain and shear stress on material surfaces from FE simulation.

(iii) Simulation results indicated that except a little smaller plastic strain of FDI (A-50) and FDI (B-50) than that of SS400, both plastic strain and shear stress on FDI were generally higher than those on SS400. As for FDI, plastic strain reached to maximum at 50deg. for FDI (A-30) and 80deg. for FDI (B-50), shear stress was unchanged at different impact angles. While, as for SS400, plastic strain changed little at different impact angles, shear stress changed obviously with maximum shear stress at 20deg.. So plastic strain and shear stress play main role on erosion of FDI and

SS400 respectively, which explained the dependence of impact angle for erosion rate curves gotten from erosion tests.

References

- [1] K. Shimizu, T. Noguchi, H. Seitoh, E. Murakami, FEM analysis of the dependency on impact angle during erosive wear, *Wear*, 233, (1999) 157-159.
- [2] K. Shimizu, T. Noguchi, H. Seitoh, M. Okada, Y. Matsubara, FEM analysis of erosive wear, *Wear*, 250, (2001) 779-784.
- [3] K. Shimizu, T. Noguchi, M. Okada, FEM analysis of the dependency on angle during erosive wear for cast iron, Japan Foundry Engineering Society, *Journal of Japan Foundry Engineering (Japanese Journal)*, 73, (2001) 362-366.

Chapter 5

A comparative study of material loss and crater deformation on ductile material during erosion simulation using 2 different material models

5.1 Introduction

In the studies from chapter 3 to chapter 4, erosion simulation were conducted by FE model of single particle impact, plastic strain and stress after impact were discussed, but material loss did not appear on the material surface, which did not agree with the actual phenomenon of erosion.

Reviewing the previous studies of published papers, it is found that if a certain material damage criterion is applied into the material model, material damage or crack could be got during simulation. In the areas of erosion research, there have been several simulations involving material loss [1-11]. The material models of these studies could be simply classified into 2 types: (i) using complex material models such as Johnson-Cook or Johnson-Holmquist material models [4-6], and (ii) using yield stress or tensile strength directly [1-3, 7-11].

For ductile material, Johnson-cook (J-C) [12, 13] was mainly used due to its fully considering various effects such as strain hardening, plastic strain rate and thermal-softening into material behaviors. However, large numbers of experiments have to be done to get appropriate J-C material parameters, besides, the J-C material parameters depend strongly on steel suppliers and experimental conditions, greatly limiting its application. Conversely, yield stress is surely to be marked for each type of steel, so simple material model considering only yield stress could be seen as an effective substitute for Johnson-Cook material model, and has also been used in some

previous simulations.

Hence, in this chapter, we established a 3D FE model of target material impacted by 5 serial particles, Johnson-cook material model and simple material model together with “shear failure” criterion were applied to target material respectively. Through investigating results of erosion simulation on mild steel ASTM A36 (similar with SS400), the difference of erosion performance on ductile material using these two different material models were discussed. Experimental results were used to verify simulation results.

5.2 Simulation

5.2.1 Material models

5.2.1.1 Johnson-Cook material model [12, 13]

Johnson-Cook material model consists of Johnson-Cook (J-C) constitutive equation and failure equation. The Johnson-Cook (J-C) constitutive equation is expressed as Eq. (5-1),

$$\bar{\sigma} = (A + B\bar{\epsilon}^n)(1 + C\ln(\frac{\dot{\bar{\epsilon}}}{\dot{\bar{\epsilon}}_0}))(1 - (\frac{T - T_r}{T_m - T_r})^m) \quad (5-1)$$

Where, $\bar{\sigma}$ is yield stress. The first, second and third bracket account for the effect of plastic strain, plastic strain rate and thermal-softening respectively. $\dot{\bar{\epsilon}}$ and $\dot{\bar{\epsilon}}_0$ are equivalent plastic strain rate and reference strain rate respectively. T indicates current temperature. The meanings of other constants are listed in Table. 5.1.

The Johnson-Cook (J-C) failure equation is expressed as Eq. (5-2),

$$\bar{\epsilon}_f = (d_1 + d_2 \exp(d_3 \frac{p}{q}))(1 + d_4 \ln(\frac{\dot{\bar{\epsilon}}}{\dot{\bar{\epsilon}}_0}))(1 + d_5 (\frac{T - T_r}{T_m - T_r})) \quad (5-2)$$

Where, $\bar{\epsilon}_f$ is plastic strain at failure, p is the average of three principal stresses and q is Von-Mises stress.

ASTM A36 (similar with SS400) was used as target material with Johnson-Cook material models. The material parameters are listed in Table 5.1 [14, 15]. The reference strain rate $\dot{\bar{\epsilon}}_0$ of ASTM A36 was set as 1 s^{-1} in simulation.

5.2.1.2 Simple material model

In simple material model, the effect of strain hardening, plastic strain rate and thermal-softening on yield stress $\bar{\sigma}$ and plastic strain at failure $\bar{\varepsilon}_f$ are neglected. Yield stress $\bar{\sigma}$ is replaced by a constant value σ_f . “Shear failure”, also assumed as a constant value ε_f and replaced for $\bar{\varepsilon}_f$ in J-C failure equation, was used to simulate material failure. The simulation in this study were conducted under 5 different shear failure ε_f of 0.5, 0.7, 0.9, 1.1 and 1.03. The material parameters of SS400 with simple material model are also listed in Table 5.1.

5.2.1.3 Material failure

For both material models, material failure occurs due to the accumulation of individual damages, it is expressed as Eq. 5-3,

$$\omega = \frac{\bar{\varepsilon}_0^{pl} + \sum \Delta\bar{\varepsilon}^{pl}}{\bar{\varepsilon}_f^{pl}} \quad (5-3)$$

Where, ω is damage parameter, $\bar{\varepsilon}_0^{pl}$ is initial value of equivalent plastic strain, $\Delta\bar{\varepsilon}^{pl}$ is equivalent plastic strain at each individual damage, $\bar{\varepsilon}_f^{pl}$ is plastic strain at failure. When ω reaches to 1, material failure occurs, and failure elements remove from target material.

Table 5.1 Material parameters of ASTM A36 and SS400

Material parameters	Symbol	Unit	ASTM A36	SS400
Density	ρ	kg/m ³	7800	
Young's modulus	E	GPa	200	
Poisson's ratio	ν	—	0.3	
<i>Johnson-Cook material model</i>				
Yield stress at zero strain	A	MPa	283.86	—
J-C Hardening coefficient	B	MPa	496.2	—
J-C Strain-hardening index	n	—	0.2282	—
J-C strain rate constant	c	—	0.022	—
J-C thermal exponent	m	—	0.9168	—
Melting temperature	T_m	°C	1538	—
Specific heat capacity	C_p	J/(kg·K)	486	—
J-C failure constant	d_1	—	0.4025	—
J-C failure constant	d_2	—	1.107	—
J-C failure constant	d_3	—	-1.899	—
J-C failure constant	d_4	—	0.009607	—
J-C failure constant	d_5	—	0.3	—
<i>Simple material model</i>				
Yield stress	σ_f	MPa	—	491
Shear failure	ε_f	—	—	0.5~1.1, 1.03

5.2.2 Finite Element Modeling

The erosion simulation was conducted using a general commercial FEM software, ABAQUS/Explicit (Version 6.14). Fig. 5.1 shows the FE model, 5 impact particles were impacted serially to a same place on the target material one by one. Only half model was built to improve computing speed, so symmetric surfaces were fixed in Y direction. All of bottom and outside surfaces of target material were fixed in freedom degrees. The model were meshed using a 8-node linear brick element with reduced integration and hourglass control (C3D8R), the contact region of target material were meshed in finer grid to improve accuracy of results. The edge length of element in contact region was 0.0075mm. There were 1024 elements and 24640 elements for each impact particle and target material respectively. Impact particles were built as rigid bodies to save CPU cost. The density, Young's modulus and Poisson's ratio of

impact particles were 7800kg/m^3 , 200GPa and 0.3 , respectively. Coulomb friction was used to define the interaction between target material and impact particles, no interaction was defined between impact particles. Diameter and initial velocity of impact particles were $0.7\mu\text{m}$ and 20m/s respectively, same with those in erosion tests. Impact angles ranged from 10deg. to 90deg. in increment of 10deg. . The simulation time was set as 1.75×10^{-4} s, step time was set as 1.75×10^{-6} s. After each simulation, number of failure elements on target material were counted and used as material loss hereinafter.

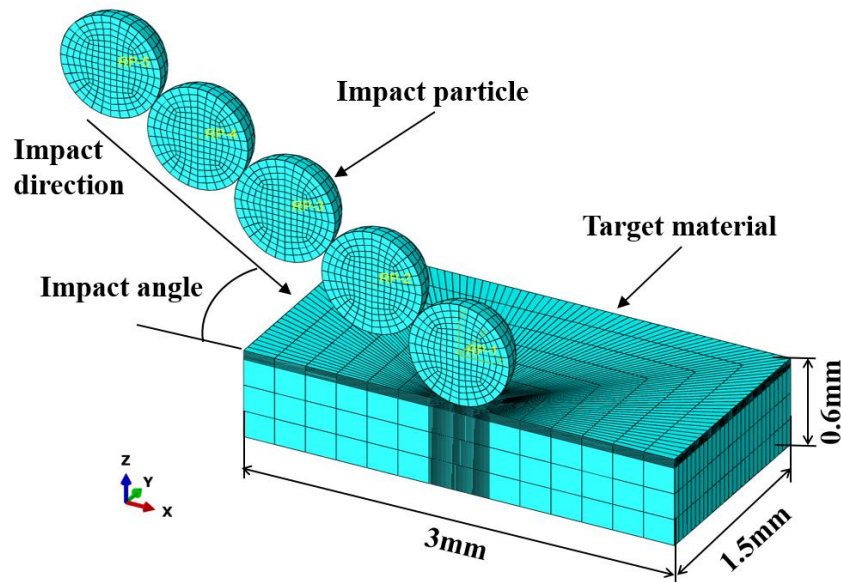


Fig. 5.1 FE model and mesh

5.3 Results and discussion

5.3.1 Effect of shear failure for simple material model

In this section, the simulations were conducted under friction coefficient $\mu=0.2$. Fig. 5.2 shows the relationship between material loss and impact angle under 5 different shear failure ε_f of 0.5, 0.7, 0.9, 1.1 and 1.03. It is seen that with increasing of shear failure, material loss decreased, otherwise, the impact angle for maximum material loss shifted from higher to lower. That is because that shear failure is an indicator for ductility of material, when shear failure decreases, ductility becomes poorer, material becomes more brittle and vulnerable to be fractured. In addition, it is

well-known that maximum erosion occurs at impact angle 80~90deg. for brittle material, 50~70deg. for cast iron and 20~40deg. for ductile material, meaning that with increasing of ductility, the impact angle for maximum erosion shifts from higher impact angle to lower one, which is consistent with the phenomenon as illustrated in Fig. 5.2. Through modifying the shear failure and then comparing material loss with Johnson-Cook model, it is found that maximum material loss using simple material model under shear failure $\epsilon_f=1.03$ was similar with that using Johnson-Cook material model, so $\epsilon_f=1.03$ was used in following discussion. Fig.5.3 shows the target material with maximum material loss using simple model under $\epsilon_f=1.03$ and Johnson-Cook model after 5 particles impact.

For both FEM results under 2 different material models, maximum material loss is normalized to 1, ratio of material loss at each impact angle with respect to maximum material loss were calculated using $ML(\theta)/ML_{max}$, here, $ML(\theta)$ is material loss at impact angle θ , ML_{max} is maximum material loss. In the same way, ratio of normalized erosion rate from erosion tests was also calculated. Ratio of erosion at different impact angles were shown in Fig. 5.4. No material loss at high impact angles of FEM was because only 5 solid particles were impacted to target material, insufficient to make material loss occur at high impact angle in simulation, but 3 curves have similar trend, so it was considered that FEM results using both different material models agreed well with erosion test results.

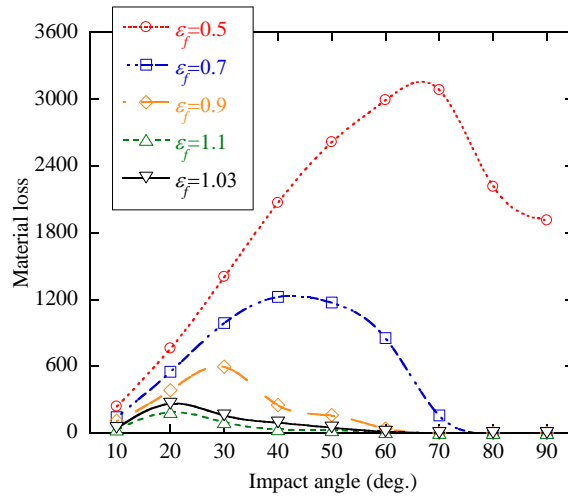
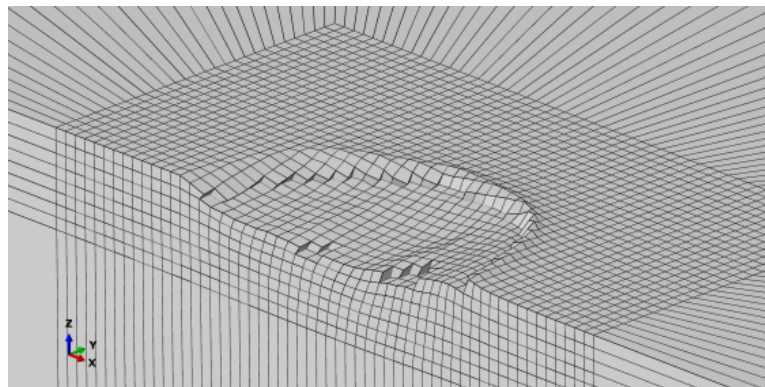
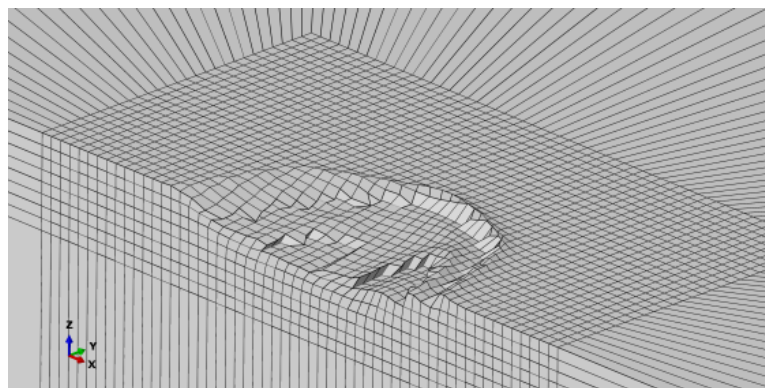


Fig. 5.2 Relationship between Material loss and impact angle under different shear failure ϵ_f for simple material model ($\mu=0.2$)



(a) Johnson-Cook model



(b) Simple material model ($\epsilon_f=1.03$)

Fig. 5.3 Target material with maximum material loss of 2 different material models ($\mu=0.2$)

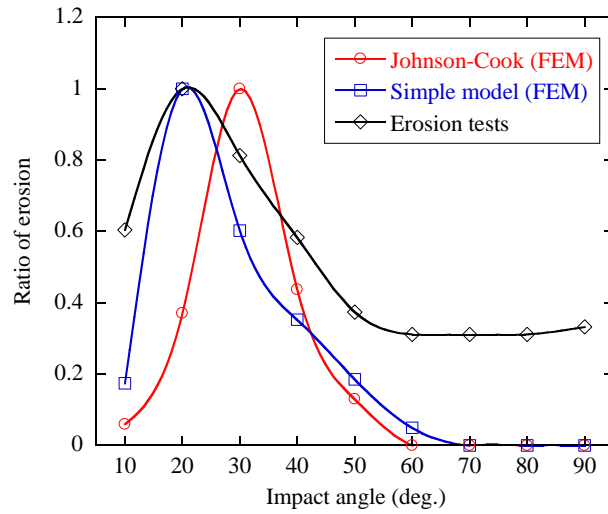


Fig. 5.4 Ratio of erosion vs impact angle from FEM and erosion tests

5.3.2 Effect of friction coefficient

The erosion surfaces from erosion tests were shown in Fig. 5.5. It can be seen that erosion surfaces at low impact angles was corrugate and wrinkled, whereas the erosion surfaces at high impact angle became smoother. The corrugate and wrinkled surfaces were vanishing with increasing of impact angle, indicating that erosion surfaces were torn more seriously at low impact angles than high impact angles. That was because there is friction between solid particles and material surfaces, the coarseness of particles exert much more scratching and tearing actions on material surface at low impact angles than those at high impact angles. The role of friction on erosion is shown in Fig. 5.6 schematically. So it is considered that friction plays an important role on erosion. Therefore, the effect of friction were discussed in this section.

The relationship between material loss and impact angle under different friction coefficients were shown in Fig. 5.7. It is found that for both material models, material loss increased with increasing of friction coefficient. Besides, the curves of $\mu=0.1$ and 0.2 were largely different with each other, also largely different with 3 curves of $\mu=0.3\sim 0.5$, and 3 curves of $\mu=0.3\sim 0.5$ were nearly overlapped, which indicates that increasing of friction coefficient had obvious increasing effect on

erosion at low friction coefficients, but had unobvious increasing effect on erosion at high friction coefficients.

Maximum material loss of 2 different material models under friction coefficients $\mu=0.1$ and 0.5 were shown in Fig. 5.8, so it is clearly seen that maximum material loss of Johnson-Cook model was a little higher than that of simple model under friction coefficient $\mu=0.1$, in contrast, became a little lower than that of simple model under friction coefficient $\mu=0.5$, indicating that increasing of friction coefficient exerts more obvious effect on increasing of erosion for simple material model than that for Johnson-Cook material model.

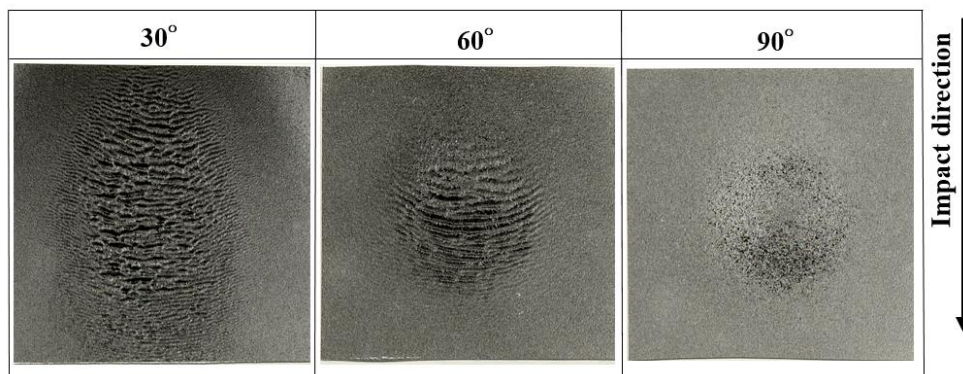


Fig. 5.5 Appearance of erosion surfaces for SS400

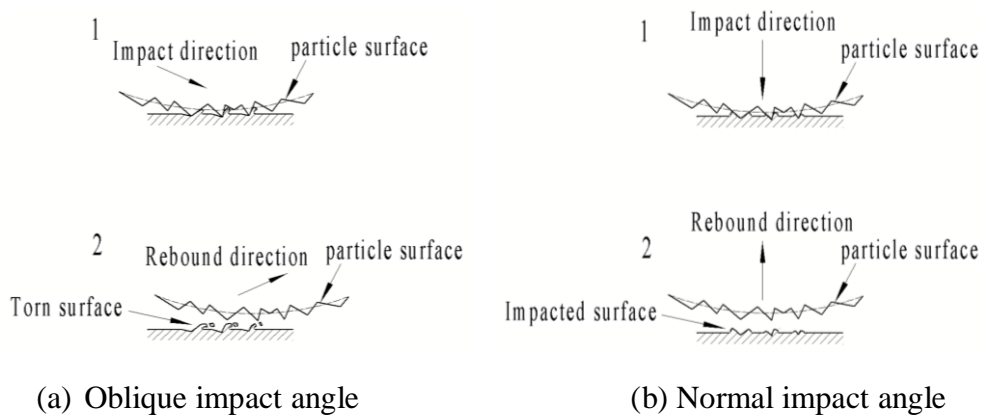


Fig. 5.6 Schematic of role of friction during erosion

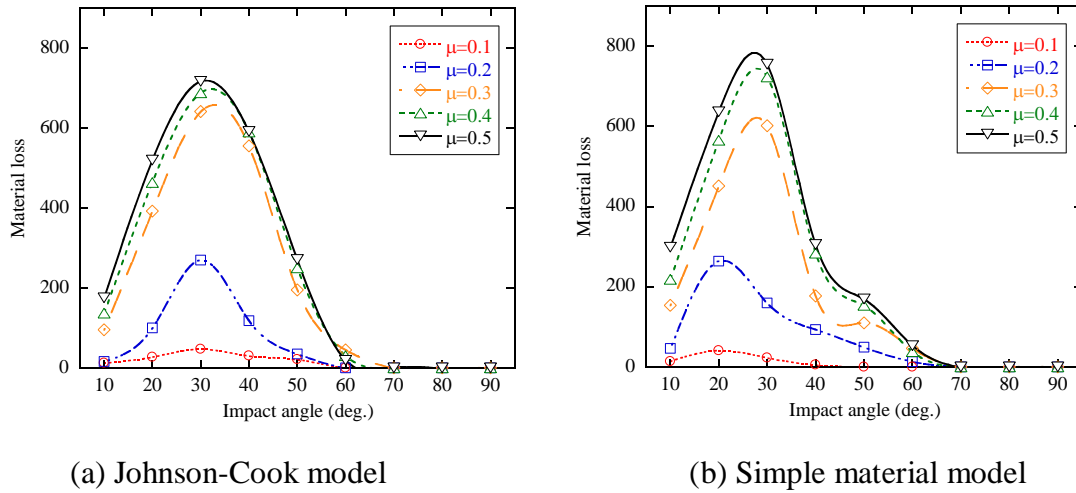


Fig. 5.7 Relationship between material loss and impact angle from FEM under different friction coefficients

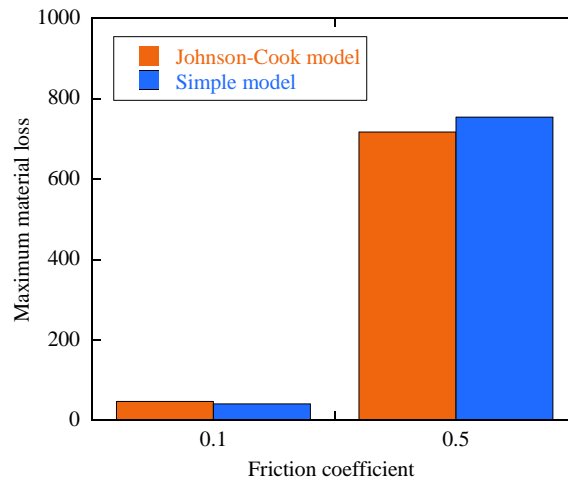


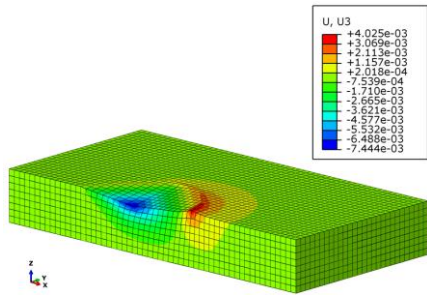
Fig. 5.8 Comparison of maximum material loss of 2 different material model under friction coefficients $\mu=0.1$ and 0.5

5.3.3 Craters of single particle impact

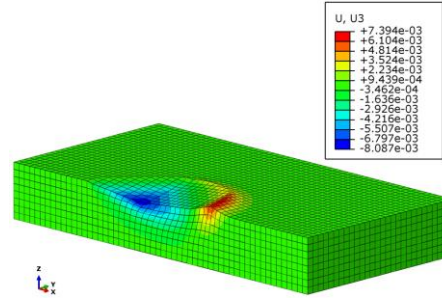
In this section, the deformation on target material at simulation time $t=2.8 \times 10^{-5}$ s are discussed, at this time, target material was impacted only by the first particle. Fig. 5.9 shows the distribution of displacement in Z direction under friction coefficient $\mu=0.2$. It can be seen that craters under Johnson-Cook and Simple material model has similar shapes, also similar with craters gotten from single particle impact tests

as shown in Fig. 5.10. However, the deformation of craters under 2 different material models showed a little different. In order to compare the differences clearly, crater depths and pile-up heights of a tiny material at rebound side at each impact angle under 2 different material models were shown in Fig. 5.11.

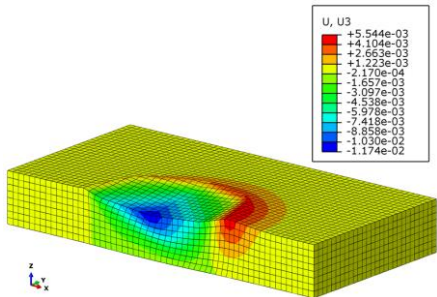
It is found that, crater depth increased with increasing of impact angle in a quadratic curve way, and all craters of simple model were deeper than those of Johnson-Cook model. Pile-up height increased firstly and then decreased with increasing of impact angle with maximum material pile-up occurring around the impact angles for maximum erosion, and all material pile-up of Johnson-Cook model were also higher than those of simple model. The curves of 2 different material models were verified with curves of test. These curves indicates that simple model could cause larger deformation than Johnson-Cook model during simulation, but 2 material models are both acceptable due to the consistence with test results.



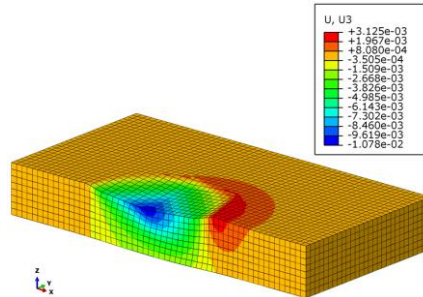
(a) 30deg., Johnson-Cook model



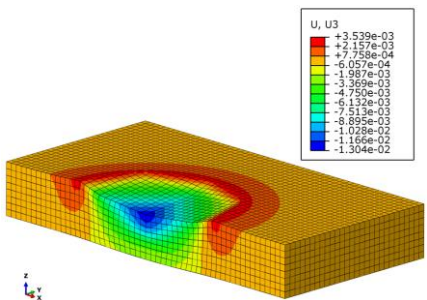
(b) 30deg., Simple model



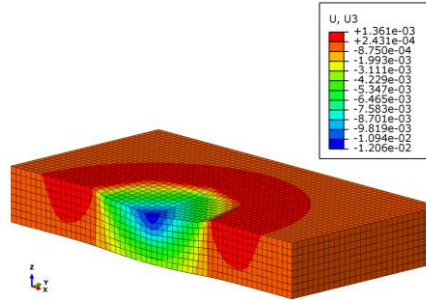
(c) 60deg, Johnson-Cook model



(d) 60deg, Simple model



(c) 90deg., Johnson-Cook model



(d) 90deg., Simple model

Fig. 5.9 Distribution of displacement in Z direction after first particle impact from FEM ($\mu=2$, impact direction is along positive x-axis)

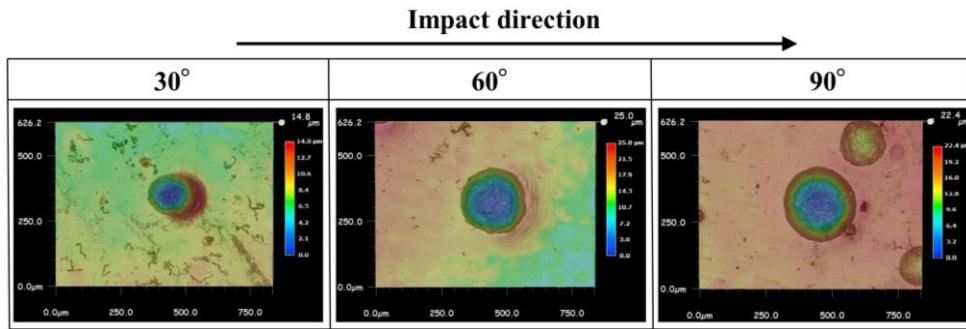


Fig. 5.10 Appearance of craters after single particle impact test

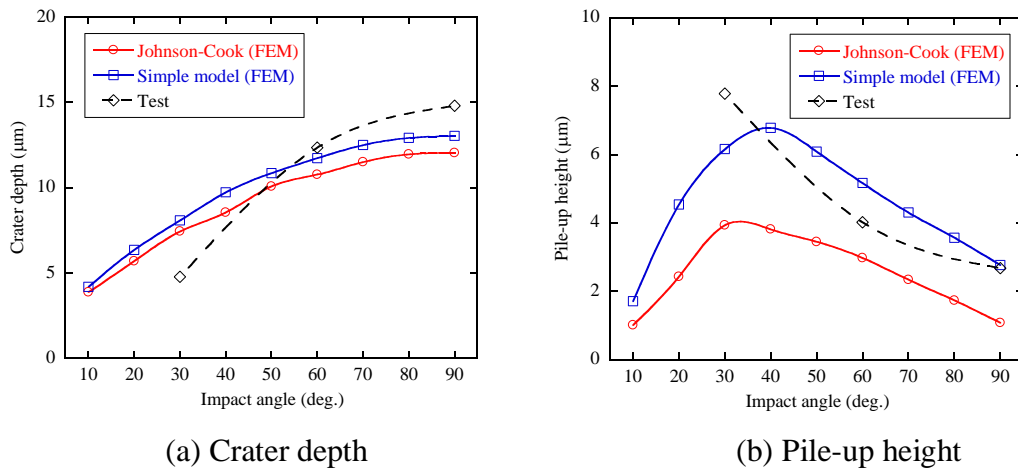


Fig. 5.11 Crater depth and pile-up height at different impact angle ($\mu=0.2$ for FEM)

5.4 Conclusions

In this chapter, FEM simulations for erosion on ductile material were conducted using 2 different material models, namely Johnson-Cook material model and simple material model. The differences of these 2 material models were discussed.

(i) For simple material model, increasing of shear failure not only can cause increasing of material loss, but also can cause the impact angle for maximum material loss shifting from higher to lower, indicating that increasing of shear failure can decrease the ductility of material. Material loss using simple model of shear failure $\epsilon_f=1.03$ was similar with that using Johnson-Cook model, so shear failure $\epsilon_f=1.03$ was used for following discussion.

(ii) Effect of friction coefficient on material loss for both material models showed similar, which was that increasing of friction coefficient cause more material loss, with obvious increasing effect under low friction coefficients $\mu=0.1\sim 0.3$ and

unobvious increasing effect under high friction coefficients $\mu=0.3\sim 0.5$. However, material loss increased a little more rapidly by using Johnson-Cook model than that by using simple model.

(iii) Through investigating the craters after single particle impact under both different material models, craters became deeper in a quadratic curve way with increasing of impact angle, material pile-up became highest around the impact angle for maximum erosion on ductile material, indicating that deformation under both material models showed similar. However, a little deeper crater and higher material pile-up under simple model than those under Johnson-Cook model indicated that simple model can cause larger deformation than Johnson-Cook model.

References

- [1] D. Aquaro, E. Fontani, Erosion of ductile and brittle materials, *Meccanica*, 36, (2001) 651-661.
- [2] D. Aquaro, Erosion due to the impact of solid particles of materials resistant at high temperature, *Meccanica*, 41, (2006) 539-551.
- [3] D. Griffin, A. Daadbin, S. Datta, The development of a three-dimensional finite element model for solid particle erosion on an alumina scale/MA956 substrate, *Wear*, 256, (2004) 900-906.
- [4] M. S. ElTobgy, E. Ng, M. A. Elbestawi, Finite element modeling of erosive wear, *International Journal of Machine Tools and Manufacture*, 45, (2005) 1337-1346.
- [5] Y. F. Wang, Z. G. Yang, Finite element model of erosive wear on ductile and brittle materials, *Wear*, 265, (2008) 871-878.
- [6] Z. G. Liu, S. Wan, V. B. Nguye, A numerical study on the effect of particle shape on the erosion of ductile materials, *Wear*, 313, (2014) 135-142.
- [7] Q. Chen, D. Y. Li, Computer simulation of solid particle erosion, *Wear*, 254, (2003) 203-210.
- [8] Q. Chen, D. Y. Li, Computer simulation of solid-particle erosion of composite materials, *Wear*, 255, (2003) 78-84.
- [9] Q. Chen, D. Y. Li, Computer simulation of erosion–corrosion of a non-passive

- alloy using a micro-scale dynamic model, *Materials Science and Engineering*, A369, (2004) 284-293.
- [10] J. Hu, D. Y. Li, R. Llewellyn, Computational investigation of microstructural effects on abrasive wear of composite materials, *Wear*, 259, (2005) 6-17.
- [11] J. Hu, D. Y. Li, R. Llewellyn, Synergistic effects of microstructure and abrasion condition on abrasive wear of composites—A modeling study, *Wear*, 263, (2007) 218-227.
- [12] G. R. Johnson, W. H. Cook, A constitutive model and data for metals subjected to large strains, high strain rates and high temperatures, *Proceedings of the 7th International Symposium on Ballistics*, 21, (1983) 541-547.
- [13] G. R. Johnson, W. H. Cook, Fracture characteristics of three metals subjected to various strains, strain rates, temperatures and pressures, *Engineering fracture mechanics*, 21, (1985) 31-48.
- [14] Jeremy D. Seidt, Amos Gilat, John R. Leach, High strain rate, high temperature constitutive and failure models for EOD impact scenarios, *Proceedings of the SEM Annual Conference & Exposition on Experimental and Applied Mechanics*. Society for Experimental Mechanics, 2007, 15.
- [15] Shawoon K. Roy, Mohamed Trabia, Brendan O'Toole, Robert Hixson, Steven Becker, Michael Pena, Richard Jennings, Deepak Somasundaram, Melissa Matthes, Edward Daykin, Eric Machorro, Study of Hypervelocity Projectile Impact on Thick Metal Plates, *Shock and Vibration*, 2016, 1-11.

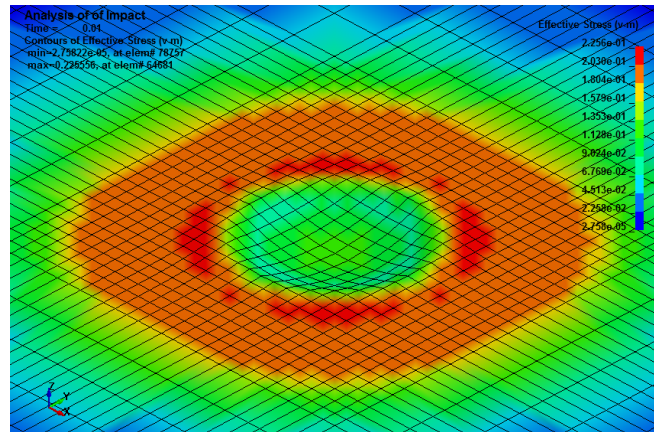
Chapter 6

Impact simulation of angular particles on mild steel using a coupled method of finite element and smoothed particle hydrodynamics

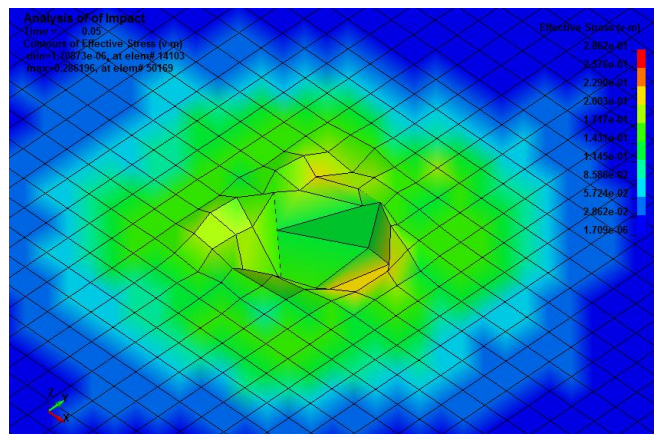
6.1 Introduction

In simulations from chapter 3 to chapter 5, Finite Element Method (FEM) was used to build the models of target material, FE models of target material were built using Lagrange meshes, which is appropriate for spherical particle impact, because their meshes kept regular after spherical particle impact. However, when target material is impacted by tip of angular particles, distortion or tangle meshes would occur on the target material, dramatically decreasing the accuracy of simulation results. The appearance of Lagrange mesh after spherical particle impact and angular particle impact are shown in Fig. 6.1. So a mesh-free method named as Smoothed Particles Hydrodynamics (SPH) has been used to overcome the shortage of Lagrange meshes. However, SPH method usually takes much more computational cost than FEM, as a result, a method coupling SPH and FEM was proposed to combine the respective advantages of FEM and SPH.

In this chapter, a 3D numerical model coupling SPH and FEM was built via ANSYS/LS-DYNA to study impact performance of angular particles on mild steel. Firstly, simulations of spherical particles impact were also conducted and the difference between angular particles impact and spherical particles impact were investigated. Secondly, angular particles with different shapes were built by varying the angularity but keeping the whole volume of angular particle unchanged, the effect of angularity of angular particles on mild steel during impact process were discussed.



(a) Spherical particle



(b) Angular particle

Fig. 6.1 Deformation on target material under spherical particle and angular particle impact using Lagrange meshes

6.2 Brief description of SPH theory

Smoothed Particles Hydrodynamics (SPH) is a mesh-free method invented by Lucy [1] and Gingold and Monaghan [2]. It was initially used for modeling astrophysical phenomena such as exploding stars and dust clouds without boundaries. With development of SPH theory, up to now, SPH method has been extensively used in a wide range of problems in both fluid and solid mechanics because of its strong ability to incorporate complex physical formulations into SPH simulation, such as multi-phase flow [3], heat conduction [4], explosion [5, 6], mechanical machining [7, 8] and high speed impact [9, 10] etc..

There are two basic steps for SPH formulations, first step is kernel approximation and second step is particle approximation [11].

For an arbitrary continuum function $f(\mathbf{x})$, it can be expressed as Eq. 6-1,

$$f(\mathbf{x}) = \int_{\Omega} f(\mathbf{x}')\delta(\mathbf{x} - \mathbf{x}')d\mathbf{x}' \quad (6-1)$$

Where $\delta(\mathbf{x})$ is Dirac delta function. Kernel approximation means that the $\delta(\mathbf{x})$ function is replaced with a certain smoothed function. The kernel approximation of a function $f(\mathbf{x})$ in SPH method is expressed as Eq. 6-2,

$$\langle f(\mathbf{x}) \rangle = \int_{\Omega} f(\mathbf{x}')W(\mathbf{x} - \mathbf{x}', h)d\mathbf{x}' \quad (6-2)$$

Where, $W(\mathbf{x}-\mathbf{x}', h)$ is a smoothing function, h is the smoothing length defining the influence or support area of the smoothing function W , and Ω is integral region. $W(\mathbf{x}-\mathbf{x}', h)$ should have a central peak value, satisfying with three conditions named as *even*, *unity* and *compact* [11]. The most common smoothing function is the cubic B-spline function [11, 12], which is originally used by Monaghan and Lattanzio [13],

$$W(R, h) = C \times \begin{cases} \frac{2}{3} - R^2 + \frac{1}{2} R^3 & 0 \leq R < 1 \\ \frac{1}{6} (2 - R)^3 & 1 \leq R < 2 \\ 0 & R \geq 2 \end{cases} \quad (6-3)$$

Where C is a constant which depends on space dimension, $C=1/h$, $15/7\pi h^2$ and $3/2\pi h^3$ are used in one-, two- and three-dimension respectively.

Particle approximation is second basic process for SPH formulations. Particle approximation is the process that computational domain is represented with a finite number of discrete particles, then the continuous form of kernel approximation in Eq. (6-2) can be written in discretized form of a summation of the neighboring particles as followed,

$$\langle f(\mathbf{x}) \rangle = \sum_{j=1}^N \frac{m_j}{\rho_j} f(\mathbf{x}_j)W(\mathbf{x} - \mathbf{x}_j, h) \quad (6-4)$$

Where, N is the total number of particles within computational domain, m_j and ρ_j are the mass and density of the particles j , respectively.

The process of SPH simulation should be satisfied with conservation equations for mass, momentum and energy [14]. The discretized form of three conservation equations can be written as followed,

$$\text{Conservation of mass:} \quad \frac{\partial \rho_j}{\partial t} = \sum_{j=1}^N m_j \mathbf{v}_{ij} \frac{\partial W_{ij}}{\partial \mathbf{x}_i} \quad (6-5)$$

$$\text{Conservation of momentum:} \quad \frac{\partial \mathbf{v}_j}{\partial t} = \sum_{j=1}^N m_j \left(\frac{\boldsymbol{\sigma}_i}{\rho_i^2} + \frac{\boldsymbol{\sigma}_j}{\rho_j^2} \right) \frac{\partial W_{ij}}{\partial \mathbf{x}_i} \quad (6-6)$$

$$\text{Conservation of energy:} \quad \frac{\partial \mathbf{u}_j}{\partial t} = \sum_{j=1}^N m_j \frac{\boldsymbol{\sigma}_i \boldsymbol{\sigma}_j}{\rho_i \rho_j} \mathbf{v}_{ij} \frac{\partial W_{ij}}{\partial \mathbf{x}_i} \quad (6-7)$$

Where $W_{ij}=W_{ij}(\mathbf{x}_j-\mathbf{x}_i, h)$, $\boldsymbol{\sigma}_i$ and $\boldsymbol{\sigma}_j$ are stress tensors for particles i and j respectively, and \mathbf{v}_{ij} is relative velocity vector between particle i and j .

6.3 Simulation

6.3.1 Johnson-Cook material model

6.3.1.1 Constitutive equation and failure equation [15-17]

Johnson-Cook constitutive equation was used to simulate flow stress behavior of target material. It is expressed as Eq. 6-8,

$$\bar{\sigma} = (A + B\bar{\varepsilon}^n)(1 + C \ln(\frac{\dot{\bar{\varepsilon}}}{\dot{\bar{\varepsilon}}_0}))(1 - (\frac{T - T_r}{T_m - T_r})^m) \quad (6-8)$$

Where, $\bar{\sigma}$ is Von-mises stress, $\bar{\varepsilon}$ is equivalent plastic strain, A is the yield stress at zero strain, B and n are strain-hardening constants, C is hardening strain rate constant, $\dot{\bar{\varepsilon}}$ and $\dot{\bar{\varepsilon}}_0$ are equivalent plastic strain rate and reference strain rate respectively, T , T_r and T_m are current temperature, room temperature and melting temperature respectively, m is temperature constant.

Johnson-Cook failure equation is expressed as Eq. 6-9,

$$\bar{\varepsilon}_f = (d_1 + d_2 \exp(d_3 \frac{p}{q}))(1 + d_4 \ln(\frac{\dot{\bar{\varepsilon}}}{\dot{\bar{\varepsilon}}_0}))(1 + d_5 (\frac{T - T_r}{T_m - T_r})) \quad (6-9)$$

Where, p is the average of three principal stresses and q is Von-Mises stress, d_1 , d_2 , d_3 , d_4 , d_5 are J-C material failure constants.

Material failure occurs due to accumulation of individual damages, as expressed in Eq. 6-10,

$$\omega = \sum \left(\frac{\Delta \bar{\varepsilon}}{\bar{\varepsilon}_f} \right) \quad (6-10)$$

Material failure occurs when ω reaches to 1.

6.3.1.2 Equation of State (EOS) [15]

The Mie Gruneisen equation of state is used to describe the volumetric compression behavior of ductile material under shockwave. It is expressed as Eq. 6-11,

$$p = \frac{\rho_0 C^2 \mu \left[1 + (1 - \gamma_0/2)\mu - (\alpha/2)\mu^2 \right]}{\left[1 - (S - 1)\mu \right]^2} + (\gamma_0 + \alpha\mu)E_0 \quad (6-11)$$

Where, p is pressure, E_0 is the internal energy per initial volume, C is the interception of the V_s (shock velocity)- V_p (particle velocity) curve, S is the coefficients of the slope of V_s - V_p curve, γ_0 is unitless Gruneisen constant, α is the first order volume correction to γ_0 . The compression factor μ is defined as Eq. 6-12,

$$\mu = \frac{\rho}{\rho_0} - 1 \quad (6-12)$$

Where, ρ and ρ_0 are current density and initial density respectively.

In the simulations, mild steel ASTM A36 (similar with SS400) was used as target material, the material parameters were listed in Table 6.1.

Table 6.1 Material parameters of ASTM A36 [15, 16]

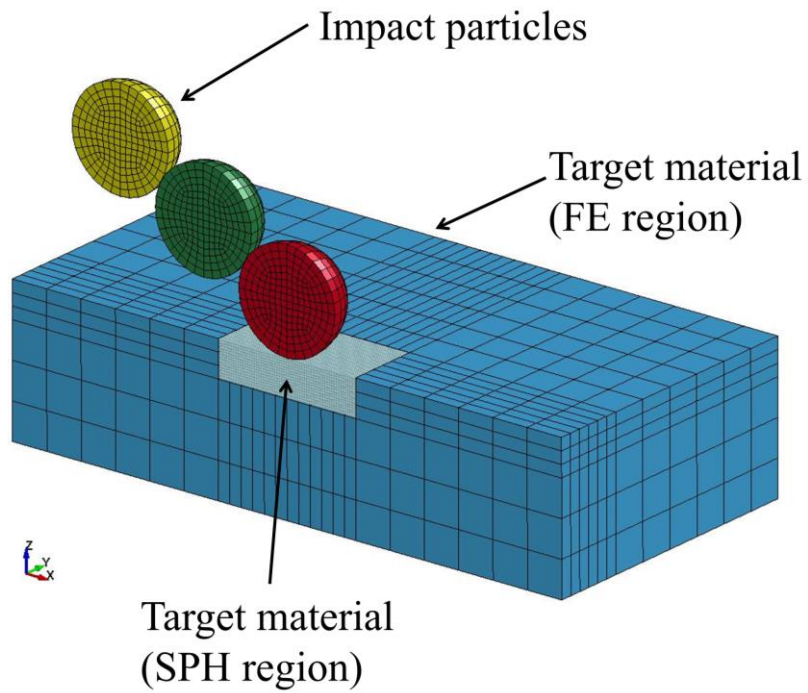
Material parameters	Symbol	Unit	ASTM A36
Density	ρ	kg/m ³	7800
Young's modulus	E	GPa	200
Poisson's ratio	ν		0.3
J-C yield stress at zero strain	A	MPa	283.86
J-C Hardening coefficient	B	MPa	496.2
J-C Strain-hardening index	n		0.2282
J-C strain rate constant	c		0.022
J-C thermal exponent	m		0.9168
Melting temperature	T_m	°C	1538
Specific heat capacity	C_p	J/(kg·K)	486
J-C failure constant	d_1		0.4025
J-C failure constant	d_2		1.107
J-C failure constant	d_3		-1.899
J-C failure constant	d_4		0.009607
J-C failure constant	d_5		0.3
Elastic bulk wave velocity	C_0	m/s	4570
Slope of V_s vs V_p curve	S		1.49
Gruneisen constant	γ_0		2.17

6.3.2 Numerical modeling

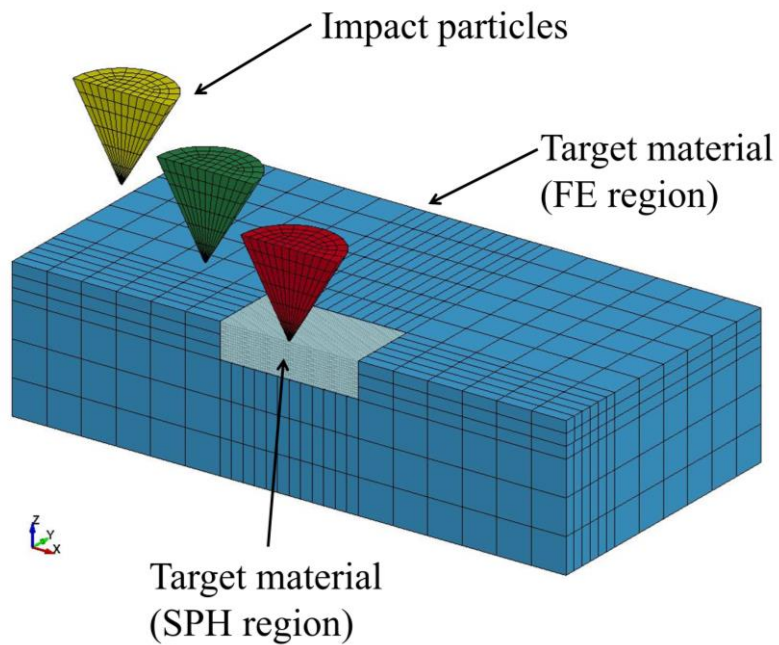
Numerical models are shown in Fig. 6.2, angular particles were simplified as cones in the simulations. Half models were built to save computing cost, so Y-displacement of nodes on symmetrical surfaces should be constrained. Target material consists of SPH region and FE region, two regions were tied using keyword `Contact_Tied_Nodes_To_Surface`. There were 27000 SPH particles in the model, mass of each SPH particle was 3.611×10^{-11} kg. Impact particles were set as rigid bodies to improve computing speed. Several impact particles were impacted to the center of SPH region serially one by one. Density, Young's modulus and Poisson's ratio of impact particles were set as 8000 kg/m^3 , 210GPa and 0.3 respectively. The

interactions between impact particles and SPH region were defined using keyword `Contact_Automatic_Nodes_To_Surface`, both static friction coefficient and dynamic coefficient were set as 0.1. The simulation time was set as $0.035\text{ms} \times N$, where N was the number of impact particles. All bottom and outside surfaces of target material were set as non-reflecting boundaries.

Diameter of spheres was $700\mu\text{m}$, same with the average diameter of steel grits in experiments. In terms of dimensions of cones, in order to investigate the effect of angularity, the cone with bottom diameter $D_{bottom}=700\mu\text{m}$ and conic angle $\theta=60\text{deg}$. was selected as standard cone, several shapes of cones were built by varying conic angle θ but with same volume of standard cone, the reason to build cones in this way is that cones with same volume have same kinetic energy before their impacts to target material. Conic angle were named as angularity here, the dimensions of cones were listed in Table 6.2. Roundness of angular tips of cones were 0.01mm . The cones with different angularity used in this work were shown in Fig. 6.3. In order to simplify the initial motion of cones, whole models should satisfy that the gravity center of first cone located in global origin.



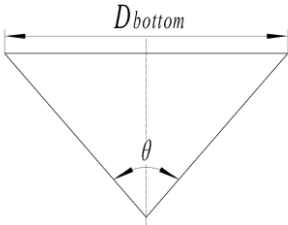
(a) Sphere impact

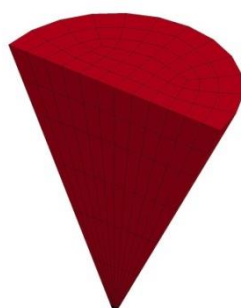


(b) Cone impact

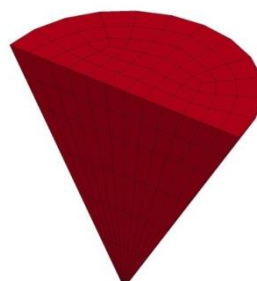
Fig. 6.2 Numerical models

Table 6.2 Dimensions of cones

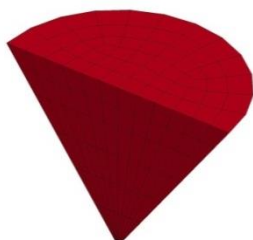
Axial cross section of cone	D_{bottom} (μm)	θ (deg.)
	651.89	50
	700	60
	746.50	70
	792.91	80
	840.66	90



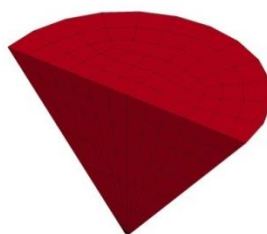
(a) $\theta=50\text{deg.}$



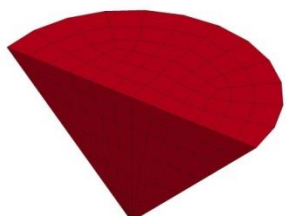
(b) $\theta=60\text{deg.}$



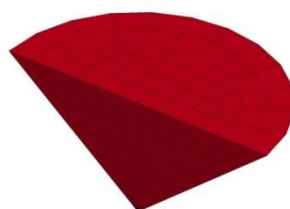
(c) $\theta=70\text{deg.}$



(d) $\theta=80\text{deg.}$



(e) $\theta=90\text{deg.}$



(f) $\theta=100\text{deg.}$

Fig. 6.3 Cones with different conic angle θ

6.4 Results and discussion

6.4.1 Comparison of sphere impact and cone impact

Material removal is caused by deformation on target material, when deformation reaches to a certain extent, material removal occurs. So plastic strain were chosen as the evaluator for following discussion. The distribution of plastic strain after 5 particles impact are shown in Fig. 6.4. The cone in this section is standard cone.

It is seen that, a crater appeared on the impact region after sphere impact, maximum plastic strain occurred on the crater surface of rebound side at low impact angle around 10~30deg., meanwhile, at impact angle 30deg., a little obvious plastic strain occurred at the subsurface of target material, with further increasing of impact angle, plastic strain at subsurface became more and more obvious, and when impact angle became higher than 50deg., maximum plastic strain occurred at subsurface of target material. In terms of cone impact, an inverted conic notch appeared at impact region, plastic strain mainly concentrated at the nearby region of notch at all impact angles. At low impact angle around 10~50deg., a tiny material protruded at the rebound side of notch, maximum plastic strain occurred at the root of protruded material. Material removal is most likely to occur due to fracture of protruded material by further particles impact, as shown in Fig. 6.5. Whereas at high impact angles such as 70~90deg., the notch became larger, but protruded material became vanishing, making material removal difficult at high impact angles, which explained why erosion at high impact angles is smaller than that at low impact angles. As shown in Fig. 6.4 (j), at normal impact angle 90deg., notch had a similar shape with tip of cone, maximum plastic strain occurred at the side wall of notch, demonstrating that plastic strain at normal impact causes due to friction between cone and side wall of notch.

Relationship between plastic strain and impact angle are shown in Fig. 6.6. For sphere impact, maximum plastic strain of SPH particles on the crater surfaces were used in Fig. 6.6, which is because although maximum plastic strain of whole SPH region occurred at subsurface at high impact angles, it is impossible for material removal to occur there. For cone impact, maximum plastic strain were used in Fig. 6.6, which is because maximum plastic strain just occurred at the nearby region of notch.

The curves in Fig. 6.6 have same trend with curves of erosion rate and impact angle as shown in Fig. 6.7, so the simulation were acceptable.

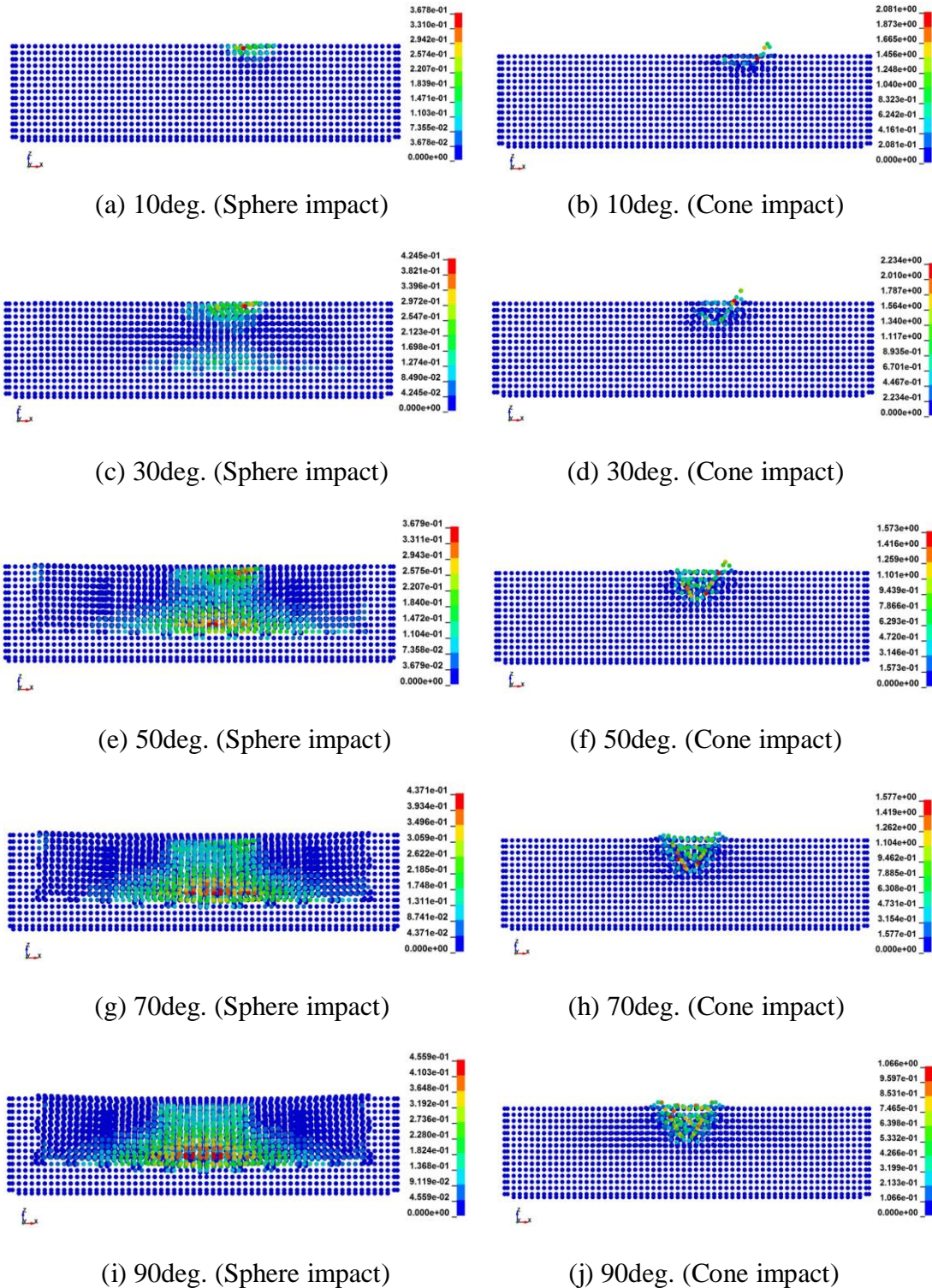
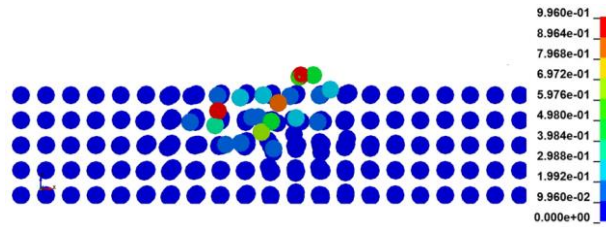
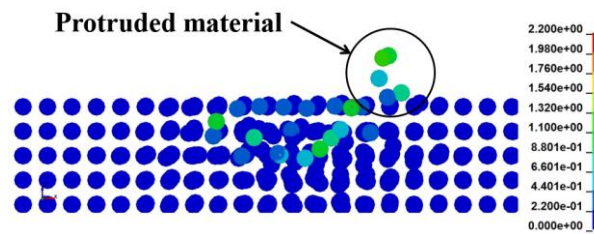


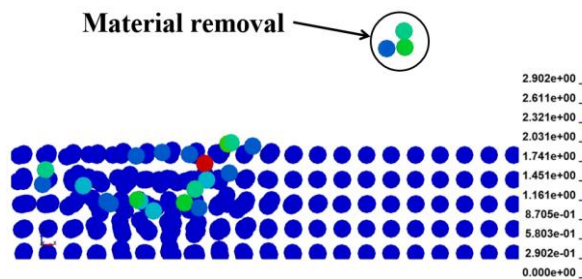
Fig. 6.4 Plastic strain on target material after 5 particle impact at impact angles 10deg., 30deg., 50deg., 70deg. and 90deg. (impact direction was from left to right for 10deg., 30deg., 50deg. and 70deg.)



(a) 2 particles



(b) 5 particles



(c) 7 particles

Fig. 6.5 Process of material removal for cone impact after 2, 5 and 7 particles impact at impact angle 20deg.

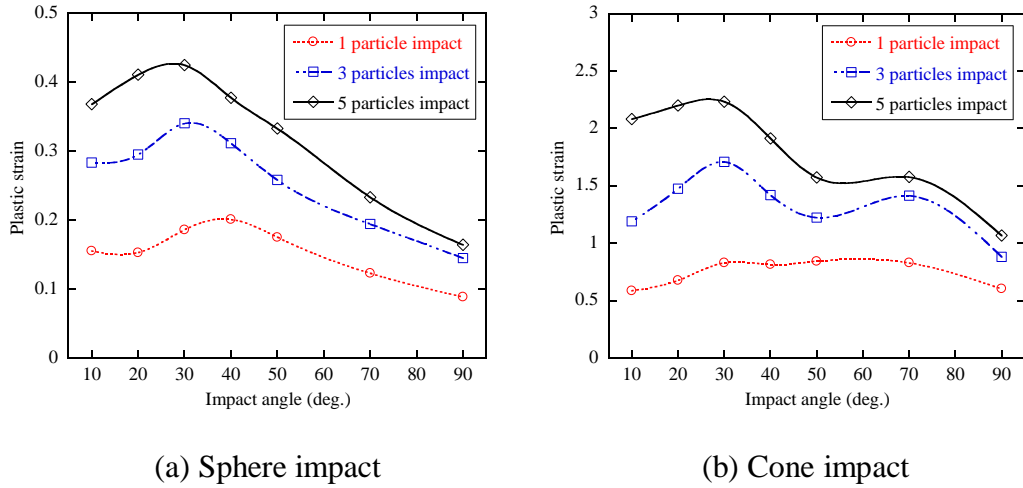


Fig. 6.6 Relationship between plastic strain and impact angle from simulation

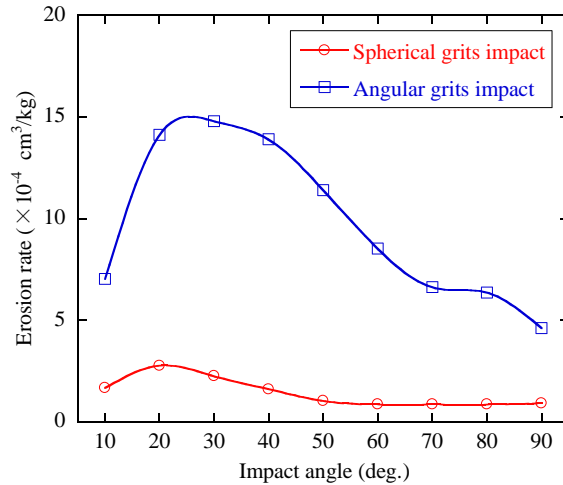


Fig. 6.7 Relationship between erosion rate and impact angle from experiment

6.4.2 Effect of angularity for single cone impact

When target material were impacted with one cone, the target material was damaged, making shape of target material different for subsequent cones impact, in order to keep simulation conditions in common for different cones, target material without damage after single cone impact were discussed in this section, the simulations were at oblique impact angle 30deg. and normal impact angle 90deg., simulation time was 0.035ms.

Energy evolution of single standard cone impact are shown in Fig. 6.8. It is seen that during impact process, kinetic energy decreased whereas internal energy

increased, meaning that kinetic energy of particle converted into internal energy, of course, sliding energy due to friction were also converted from kinetic energy, but it was too small to be shown here. Therefore, the reduction of kinetic energy could be seen as an evaluator of breakage for particle impact on material, and was used to discuss the effect of angularity of cone combining with penetration depth and plastic strain. The simulation results under different cones impact are shown in Fig. 6.9.

As shown in Fig. 6.8 and Fig. 6.9 (a), kinetic energy of normal impact decreased much more obviously than that of oblique impact, which is because cone rotated after oblique impact however no rotation existed for cone after normal impact, as illustrated in Fig. 6.10. And with increasing of angularity of cone, rotation of cone became difficult thus leading to an increase for reduction of kinetic energy for cone under oblique impact, however angularity almost have no influence on reduction of kinetic energy for cone under normal impact. So from Fig. 6.9 (a), it is concluded that breakage of cone under normal impact on target material was much larger than that under oblique impact, and larger angularity also exerted more breakage than smaller angularity.

Fig. 6.9 (b) shows relationship between penetration depth and angularity. It is seen that with increasing of angularity, penetration depth became shallower, which is because cone with larger angularity had larger contact area, so larger resistance to vertical motion were generated, causing shallower penetration depth. And, it is also seen that penetration depth under normal impact were deeper than those under oblique impact, which is because normal component of velocity was larger than that under oblique impact.

Cone impact at oblique angle exerted more ploughing action than that at normal angle, leading to more plastic strain at oblique angle than that at normal angle. As for oblique impact, with increasing of angularity, cone became difficult to rotate, so cone with larger angularity gave more ploughing action on material than that with smaller angularity, which can explain the phenomena that plastic strain increased with increasing of angularity at oblique impact as shown in Fig. 6.9 (c). As for normal impact, when angularity became larger, the normal force to the side wall of notch F_n

also became larger so that friction force between cone and side wall of notch became larger, meanwhile larger angularity made shallower penetration so that relative motion between cone and side wall of notch became lower, meaning that the duration time of the friction would decrease. So there is a critical angularity between F_n and relative motion to make the friction biggest so as to make a peak value of plastic strain, Fig. 6.9 (c) showed the critical angularity is 70deg..

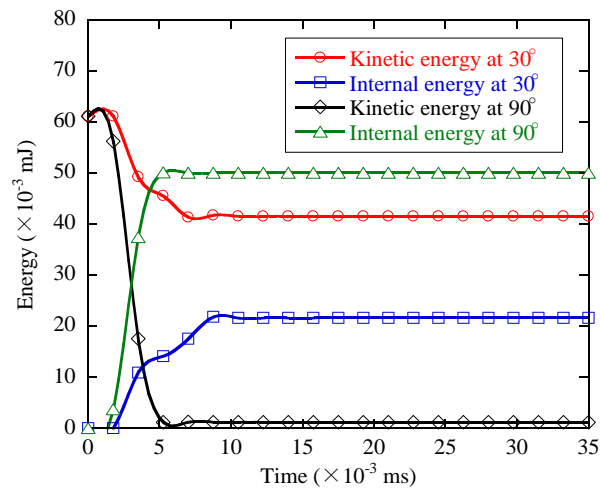
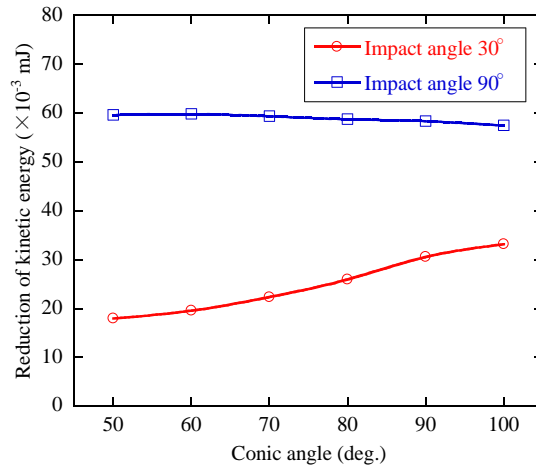
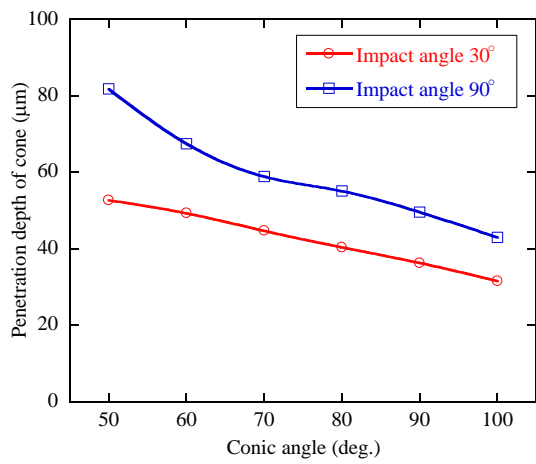


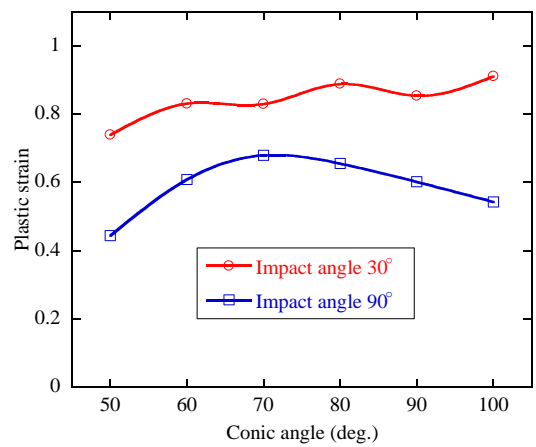
Fig. 6.8 Energy evolution of single standard cone impact at impact angle 30deg. and 90deg.



(a) Reduction of kinetic energy



(b) Penetration depth of cone



(c) Plastic strain

Fig. 6.9 Simulation results under single cone impact with different conic angles

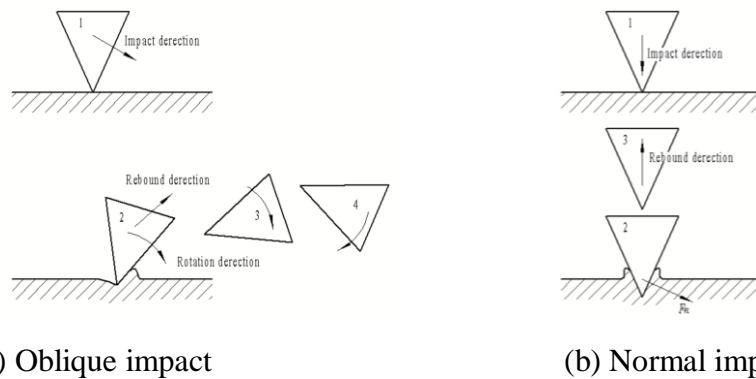


Fig. 6.10 Schematic of movement of single cone for oblique and normal impact

6.5 Conclusions

A coupled method of SPH and FEM was applied into numerical models of angular particles impact on mild steel. The difference comparing with spherical particles impact and the effect of angularity were discussed. Angular particles were simplified as cones.

(i) For spherical particles impact, maximum plastic strain occurs at the surfaces of rebound side of craters at low impact angles (about $<50\text{deg.}$), and at the subsurface of impact region at high impact angles (about $\geq 50\text{deg.}$). But for cone impact, maximum plastic strain always occurs at the nearby region of impact region at all impact angles, a tiny material protrudes from the impact region due to cone impact, with repeated impacted, protruded material grows and finally removes from material surface.

(ii) Through investigating reduction of kinetic energy, whole breakage of cones on target material at normal impact angle (90deg.) are higher than those at oblique impact angle (30deg.), with increasing of angularity of cones, kinetic energy decreases obviously under oblique impact, and approximately keep unchanged under normal impact. Plastic strain under oblique impact are higher than those under normal impact, and larger angularity increases plastic strain under oblique impact, and a peak value of plastic strain under normal impact occurs at angularity 70deg. . Cones under normal impact penetrates deeper than those under oblique impact, and larger angularity makes penetration depth shallower.

References

- [1] L. B. Lucy, A numerical approach to the testing of the fission hypothesis, *The astronomical journal*, 82, (1977) 1013-1024.
- [2] R. A. Gingold, J. J. Monaghan, Smoothed particle hydrodynamics: theory and application to non-spherical stars, *Monthly notices of the royal astronomical society*, 181, (1977) 375-389.
- [3] Andrea Colagrossi, Maurizio Landrini, Numerical simulation of interfacial flows by smoothed particle hydrodynamics, *Journal of Computational Physics*, 191, (2003) 448-475.
- [4] J. K. Chen, J. E. Beraun, T. C. Carney, A corrective smoothed particle method for boundary value problems in heat conduction, *International Journal for Numerical Methods in Engineering*, 46, (1999) 231-252.
- [5] M. B. Liu, G. R. Liu, Z. Zong, K. Y. Lam, Computer simulation of high explosive explosion using smoothed particle hydrodynamics methodology, *Computers & Fluids*, 32, (2003) 305-322.
- [6] M. B. Liu, G. R. Liu, K. Y. Lam, Z. Zong, Smoothed particle hydrodynamics for numerical simulation of underwater explosion, *Computational Mechanics*, 30, (2003) 106-118.
- [7] J. Limido, C. Espinosa, M. Salaün, J. L. Lacombe, SPH method applied to high speed cutting modelling, *International journal of mechanical sciences*, 49, (2007) 898-908.
- [8] M. Calamaz, J. Limido, M. Nouari, C. Espinosa, D. Coupard, M. Salaün, F. Girot, R. Chieragatti, Toward a better understanding of tool wear effect through a comparison between experiments and SPH numerical modelling of machining hard materials, *International journal of refractory metals and hard materials*, 27, (2009) 595-604.
- [9] M. B. Liu, G. R. Liu, K. Y. Lam, Adaptive smoothed particle hydrodynamics for high strain hydrodynamics with material strength, *Shock Waves*, 15, (2006) 21-29.

- [10] C. E. Zhou, G. R. Liu, K. Y. Lou, Three-dimensional penetration simulation using smoothed particle hydrodynamics, *International Journal of Computational Methods*, 4, (2007) 671-691.
- [11] M. B. Liu, G. R. Liu, Smoothed particle hydrodynamics (SPH): an overview and recent developments, *Archives of computational methods in engineering*, 17, (2010) 25-76.
- [12] J. O. Hallquist, LS-DYNA. Keyword User's Manual Verision 971, Livermore Software Technology Corporation, CA, 2007.
- [13] J. J. Monaghan, J. Lattanzio, A refined particle method for astrophysical problems, *Astronomy and astrophysics*, 149, (1985) 135-143.
- [14] G. R. Liu, M. B. Liu, Smoothed particle hydrodynamics: a meshfree particle method, World Scientific, Singapore, 2003.
- [15] G. R. Johnson, W. H. Cook, A constitutive model and data for metals subjected to large strains, high strain rates and high temperatures, *Proceedings of the 7th International Symposium on Ballistics*, 21, (1983) 541-547.
- [16] G. R. Johnson, W. H. Cook, Fracture characteristics of three metals subjected to various strains, strain rates, temperatures and pressures, *Engineering fracture mechanics*, 21, (1985) 31-48.
- [17] J. O. Hallquist, LS-DYNA. Keyword User's Manual Verision 971, Livermore Software Technology Corporation, CA, 2007.

Chapter 7

Erosive prediction on liners of rotating chute using a coupled simulation of DEM and FEM

7.1 Introduction

Rotating chute is an important apparatus to discharge raw materials into blast furnace in iron-making industry. Generally, the inner surface of rotating chute is installed with arrays of liners. In working process, rotating chute is placed above the blast furnace, raw materials including ore and coke are charged into blast furnace under gravity through rotating chute, so impacts between raw materials and liners become unavoidable, making serious erosion on the surface of liners, therefore the liners have to be maintained or exchanged regularly, greatly affecting work efficiency and running cost of production. Hence, in order to reduce production risks and improve economic benefits, it is necessary to conduct researches of erosion on the liners of rotating chute.

The trajectory of raw materials in rotating chute is difficult to be described, they not only move along the longitudinal direction of rotating chute due to gravity, but also move in opposition to the rotating direction due to rotation. In addition, the size of raw material particles, rotating velocity, inclination angle of chute, surface conditions of liners also have great influences on the trajectory of raw materials flow. Some mathematical models have been developed to describe the motion of raw materials particles [1, 2], but some actual working conditions were ignored for simplicity in these models so that they still could not correctly reflect the motion of raw materials in rotating chute, so the prediction of which liners in rotating chute are under erosion is still an urgent and practical problem. Therefore, in this work, a method was proposed to handle this problem.

Discrete Element Method (DEM) has become an effective way to simulate granular particles flows since its original invention by P. A. Cundall [3]. In this work, the movement of raw materials in rotating chute was simulated using DEM, and then pressure of raw materials on surface of rotating chute was transferred into Finite Element (FE) Model of rotating chute, finally, the stress status of rotating chute were obtained by FE calculation. This work provides a useful and efficient guideline for erosive prediction on rotating chute.

7.2 Brief description of DEM theory [4-8]

The motion of a particle in DEM simulation can be classified into translational and rotational motions. All motions are governed by Newton's second law of motion. During simulation, a particle of granular system collides with wall and neighboring particles. Fig. 7.1 shows a schematic view of interaction between two neighboring particles i and j . The governing equations for particle i are expressed as Eq. 7-1 and Eq. 7-2,

$$m_i \frac{d\mathbf{u}_i}{dt} = \sum_{j=1}^K (\mathbf{F}_{cn,ij} + \mathbf{F}_{dn,ij} + \mathbf{F}_{ct,ij} + \mathbf{F}_{dt,ij}) + m_i \mathbf{g} \quad (7-1)$$

$$I_i \frac{d\boldsymbol{\omega}_i}{dt} = \sum_{j=1}^K (\mathbf{T}_{t,ij} + \mathbf{T}_{r,ij}) \quad (7-2)$$

Where m_i , I_i , \mathbf{u}_i and $\boldsymbol{\omega}_i$ are mass, moment of inertia, translational velocity and angular velocity of particle i , respectively. K is the total number of its neighboring particles. Particle i is under gravitational force ($m_i \mathbf{g}$) and sum forces generated from interaction with neighboring particles. Fig. 7.2 shows schematic view of particle i under interactions by neighboring particles around it. The forces generated from interaction between particle i and particle j can be classified into 4 types: normal elastic force ($\mathbf{F}_{cn,ij}$), normal damping force ($\mathbf{F}_{dn,ij}$), tangential elastic force ($\mathbf{F}_{ct,ij}$) and tangential damping force ($\mathbf{F}_{dt,ij}$). These 4 types of forces are dependent on normal (δ_n) and tangential deformation (δ_t). The torques generated from interaction between particle i and particle j can be classified into 2 types: $\mathbf{T}_{t,ij}$ and $\mathbf{T}_{r,ij}$. $\mathbf{T}_{t,ij}$ arises from tangential force, and $\mathbf{T}_{r,ij}$ arises from rolling friction.

The normal elastic force ($\mathbf{F}_{cn,ij}$) is expressed as Eq. 7-3,

$$\mathbf{F}_{cn,ij} = -k_n \delta_n^{3/2} \mathbf{n} \quad (7-3)$$

Where $\delta_n = |\delta_{n,ij}|$, normal vector \mathbf{n} is calculated from the normal deformation ($\delta_{n,ij}$), $\mathbf{n} = \delta_{n,ij} / |\delta_{n,ij}|$. k_n is expressed as Eq. 7-4,

$$k_n = \frac{4}{3} \sqrt{R_{ij}} E^* \quad (7-4)$$

R_{ij} and E^* are expressed as Eq. 7-5,

$$R_{ij} = \frac{R_i R_j}{R_i + R_j}; \quad E^* = \left[\frac{1 - \nu_i^2}{E_i} + \frac{1 - \nu_j^2}{E_j} \right]^{-1} \quad (7-5a, b)$$

Where R_i , E_i and ν_i are radius, Young's modulus and Poisson's ratio of particle i respectively.

The normal damping force ($\mathbf{F}_{dn,ij}$) is expressed as Eq. 7-6,

$$\mathbf{F}_{dn,ij} = -\eta_n \mathbf{u}_{n,ij}; \quad \eta_n = 2 \sqrt{\frac{5}{6}} \frac{\ln e}{\sqrt{\ln^2 e + \pi^2}} \sqrt{2E^* m_{ij} \sqrt{R_{ij} \delta_n}};$$

$$m_{ij} = \frac{m_i m_j}{m_i + m_j} \quad (7-6a, b, c)$$

Where e is restitution coefficient. The velocity in normal ($\mathbf{u}_{n,ij}$) and tangential direction ($\mathbf{u}_{t,ij}$) are expressed as Eq. 7-7,

$$\mathbf{u}_{n,ij} = (\mathbf{u}_{ij} \cdot \mathbf{n}) \cdot \mathbf{n}; \quad \mathbf{u}_{t,ij} = \mathbf{u}_{ij} - \mathbf{u}_{n,ij};$$

$$\mathbf{u}_{ij} = \mathbf{u}_j - \mathbf{u}_i + \omega_j \times R_j \mathbf{n} - \omega_i \times R_i \mathbf{n} \quad (7-7a, b, c)$$

The tangential elastic force ($\mathbf{F}_{ct,ij}$) is expressed as Eq. 7-8,

$$\mathbf{F}_{ct,ij} = -k_t \delta_t \mathbf{i}_{ij}; \quad k_t = 8G_{ij} \sqrt{R_{ij} \delta_n}; \quad G_{ij} = \frac{G_i G_j}{G_i + G_j} \quad (7-8a, b, c)$$

Where δ_t is the tangential overlap and G_i is shear modulus of particle i .

The tangential damping force ($\mathbf{F}_{dt,ij}$) is expressed as Eq. 7-9,

$$\mathbf{F}_{dt,ij} = -\eta_t \mathbf{u}_{t,ij}; \quad \eta_t = 2 \sqrt{\frac{5}{6}} \frac{\ln e}{\sqrt{\ln^2 e + \pi^2}} \sqrt{8G_{ij} \sqrt{R_{ij} \delta_n} m_{ij}} \quad (7-9a, b)$$

The tangential elastic force ($\mathbf{F}_{ct,ij}$) and tangential damping force ($\mathbf{F}_{dt,ij}$) are under

the condition below,

$$\mathbf{F}_{ct,ij} + \mathbf{F}_{dt,ij} \leq \mu_s \mathbf{F}_{cn,ij} \quad (7-10)$$

Where μ_s is the static friction.

The torque by rolling forces ($\mathbf{T}_{t,ij}$) is expressed as Eq. 7-11,

$$\mathbf{T}_{t,ij} = \mathbf{R}_i \mathbf{n} \times (\mathbf{F}_{ct,ij} + \mathbf{F}_{dt,ij}) \quad (7-11)$$

The torque by friction forces ($\mathbf{T}_{r,ij}$) is expressed as Eq. 7-12,

$$\mathbf{T}_{r,ij} = -\mu_r |\mathbf{F}_{cn,ij}| \boldsymbol{\omega}'; \quad \boldsymbol{\omega}' = \boldsymbol{\omega}_i / |\boldsymbol{\omega}_i| \quad (7-12)$$

Where μ_r is the rolling friction.

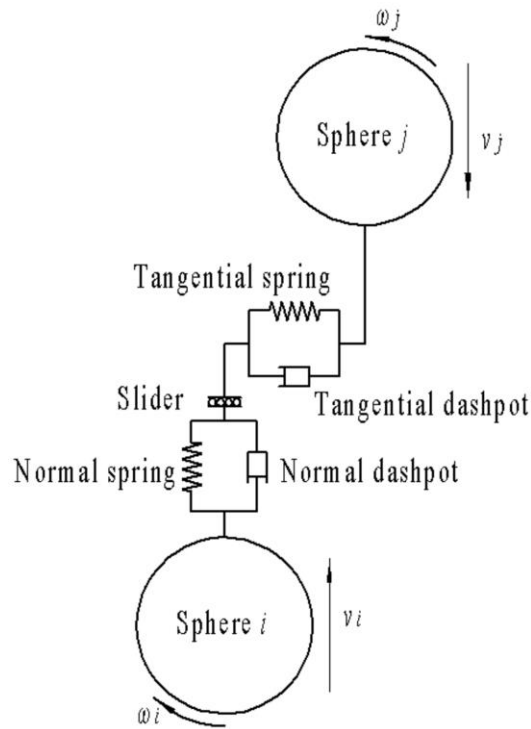


Fig. 7.1 Schematic view of interaction between two particles

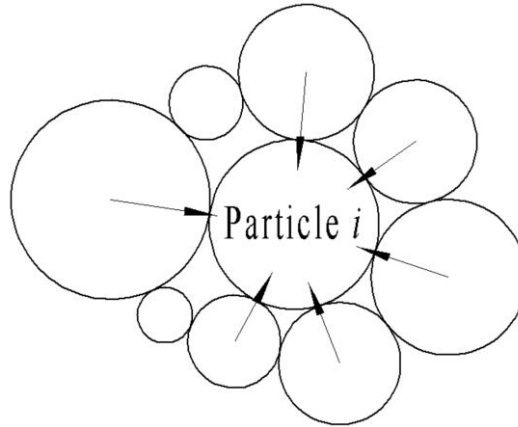


Fig. 7.2 Schematic view of sum forces by neighboring particles on particle i

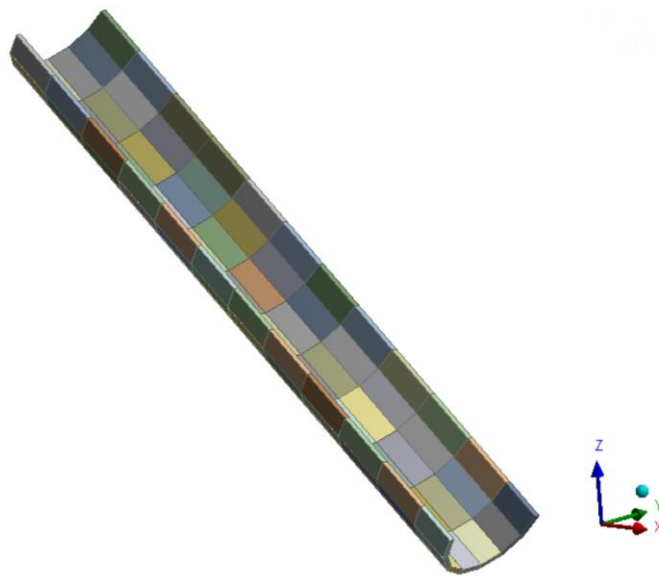
7.3 Numerical model

EDEM and ANSYS workbench were used for DEM and FEM simulation in this work respectively. The inner surface of rotating chute is installed with array of liners. Only erosion on liners was investigated, so it is not necessary to build the whole assembly model of rotating chute, only array of liners in rotating chute was built in the simulation, the actual array of liners and numerical one are shown in Fig. 7.3. The size of rotating chute and liners is shown in Fig. 7.4, which is based on an actual one. In order to explain which liner is under erosion hereinafter conveniently, the liners on the rotating chute are numbered as shown in Fig. 7.5. Ore was used as solid particles of raw materials, cast steel was used as material of liners. The material properties are listed in Table. 7.1 [9].

Simulation conditions were categorized into 3 cases to discuss the effect of diameter of raw material particles d , inclination angle of chute θ , rotating velocity ω respectively, as shown in Table 7.2. The particles generator in the simulation is placed at center of inclination, initial vertical velocity of particles is set as 6m/s (along negative direction of z-axis), which is calculated from the actual distance between center of inclination and feeding inlet. The discharging mass rate of particles was 100kg/s. Simulation time of DEM was set as 2s.

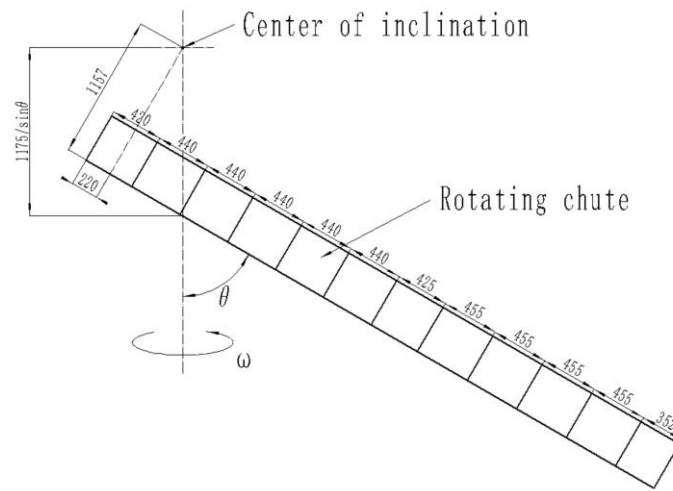


(a) Actual

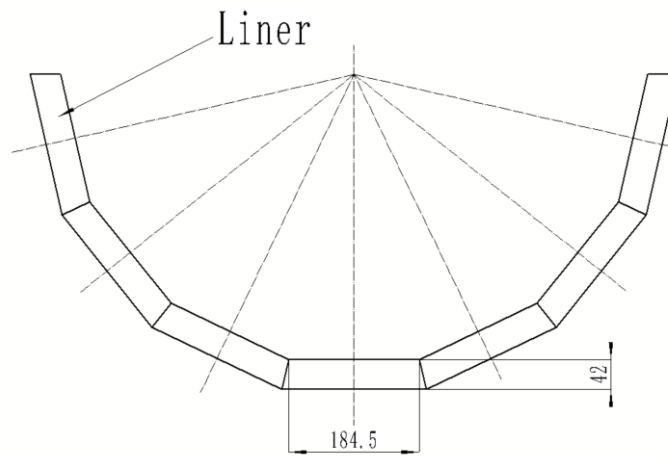


(b) Numerical

Fig. 7.3 Arrays of liners in rotating chute



(a) Side view



(b) Sectional view

Fig. 7.4 Size of rotating chute

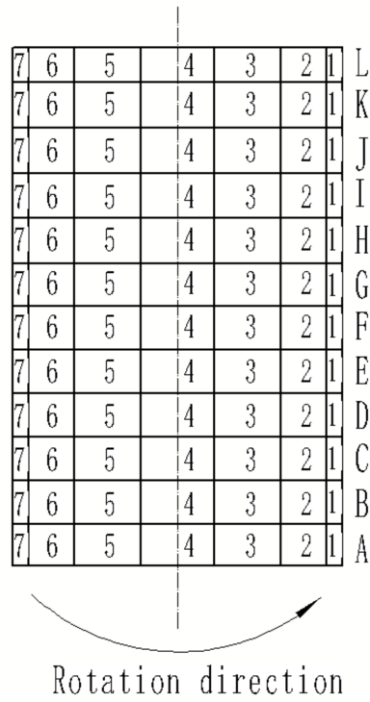


Fig. 7.5 Number of liners of rotating chute

Table 7.1 Material properties [9]

	Unit	Ore	Liner
Density	kg/m ³	2890	7800
Shear Modulus	GPa	2.4	70
Possion's ratio	—	0.28	0.3
Restitution coefficient	—	0.4	0.4
Static friction coefficient	—	0.4	0.6
Rolling friction coefficient	—	0.01	0.01

Where restitution coefficient of ore and liner indicates the coefficient of ore-ore and ore-liner, so do the static friction coefficient and rolling friction coefficient

Table 7.2 Simulation conditions

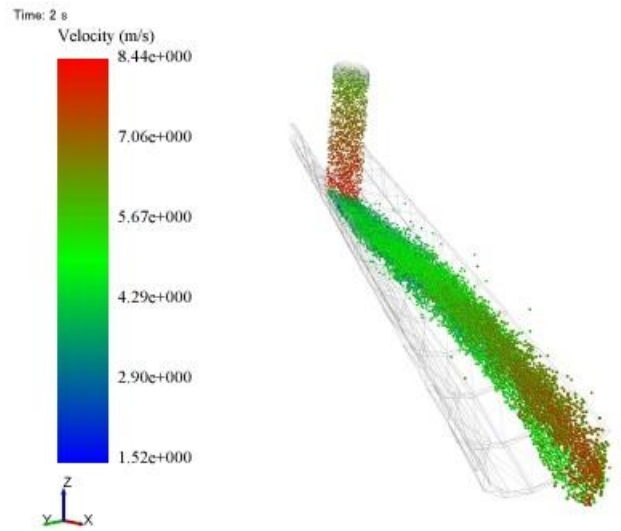
	Symbol	Unit	Case 1	Case 2	Case 3
Diameter of particles	d	mm	10~50	20	20
Inclination angle of chute	θ	deg.	50	30~70	50
Rotating velocity	ω	rpm	8	8	4~12

7.4 Results and discussion

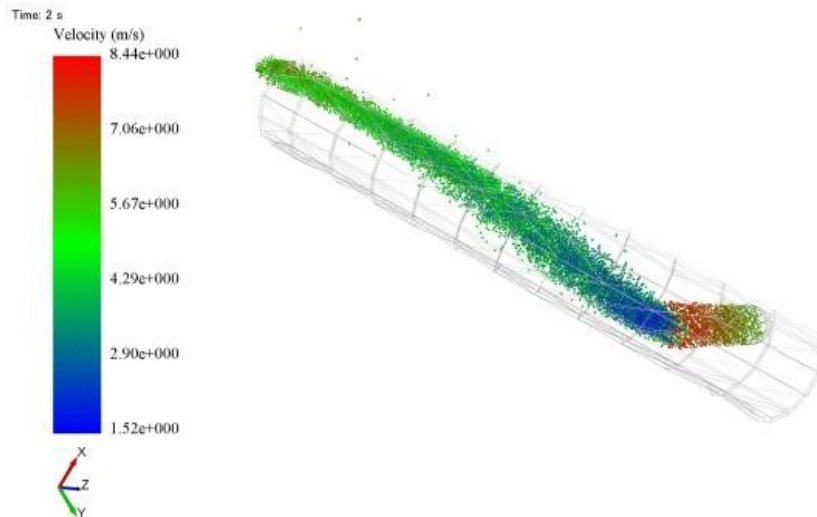
7.4.1 Flow of raw materials

An example of velocity distribution of raw materials flow is shown in Fig.7.6. It is seen that the stream of raw materials flow is not along the longitudinal direction of rotating chute, but have a deviation to the inner side wall opposition to rotating direction. According to this figure, we can get the No. of liners along the stream of raw materials flow so as to get which liners would be under erosion. As shown in Fig. 7.6, the No. of liners with obvious erosion under simulation condition $d=20\text{mm}$, $\theta=50\text{deg.}$, $\omega=8\text{rpm}$ were C4, D4, E4, E3, F3, G3, G2, H2, I2, J2, J2, K2, K1, L2, L1. Of course, we can also get the No. of liners under other simulation conditions.

The pressure on liners of rotating chute from these particles were saved as a file with “.axdt” form, and then imported into ANSYS workbench for FE calculation to get the stress state of these liners.



(a) Side view



(b) Bottom view

Fig. 7.6 Velocity distribution of raw materials flow in rotating chute ($d=20\text{mm}$, $\theta=50\text{deg.}$, $\omega=8\text{rpm}$)

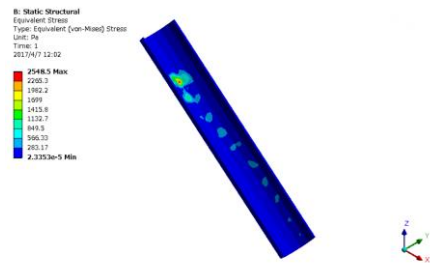
7.4.2 Stress state on liners

The distribution of von mises stress on liners of case 1 are shown in Fig. 7.7, the distribution of von mises stress on liners of case 2 are shown in Fig. 7.8, and the distribution of von mises stress on liners of case 3 are shown in Fig. 7.9. It is seen that the largest von mises stress occurred on the liner right beneath the vertical falling flow of raw materials, and obvious erosion on liners of rotating chute were along the

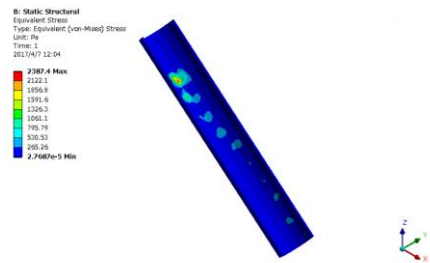
stream of raw materials flow.

The relationship between largest von mises stress on rotating chute and diameter of solid particles d (inclination angle θ and rotating velocity ω) are shown in Fig. 7.10, so influences of these three factors on largest erosion of rotating chute due to raw materials flowing can be found clearly. It is seen that largest von mises stress under different solid particles diameter d were around 2300~3000MPa, largest von mises stress under different inclination angle θ ranged from 1000 to 3300MPa, largest von mises stress under different rotating velocity ω were around 2000~2900MPa, meaning that inclination angle θ influences erosion of rotating chute much more obvious than solid particles diameter d and rotating velocity ω .

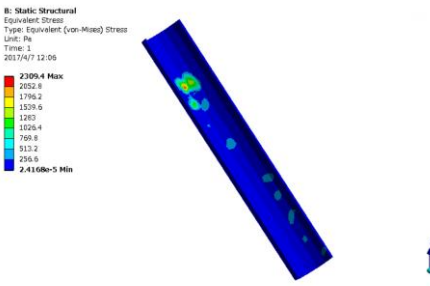
It is found that with increasing of inclination angle θ , erosion decreased firstly and then increased with lowest value at inclination angle $\theta=40\text{deg.}$. The increase of θ shortened the distance between inclination center and impact point (the length is $1175/\sin\theta$ in this model), making impact between liners and raw materials weaker, which can explain why the von mises stress decreased from 30~40deg. But with increasing of θ , raw materials became easy to pile up at the impact region on rotating chute, so the amount of raw materials at impact region increased, causing an increase of von mises stress. Velocity distribution of raw material particles at low inclination angle $\theta=30\text{deg.}$ and high inclination angle 70deg. of case 2 are shown in Fig. 7.11, it is found that no raw materials pile-up occurred at $\theta=30\text{deg.}$, meanwhile obvious raw materials pile-up occurred at $\theta=70\text{deg.}$.



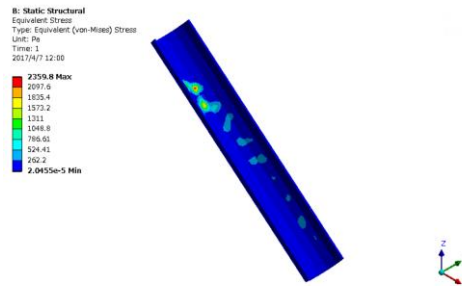
(a) $d=10\text{mm}$



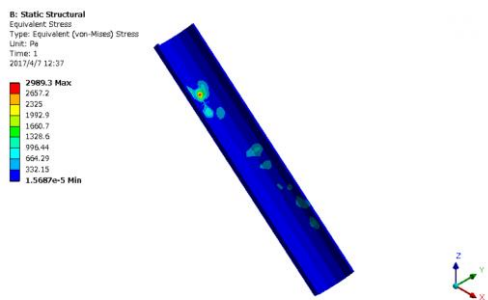
(b) $d=20\text{mm}$



(c) $d=30\text{mm}$

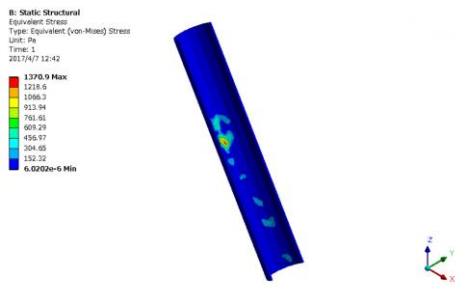


(d) $d=40\text{mm}$

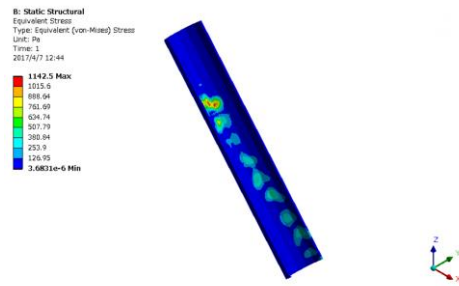


(e) $d=50\text{mm}$

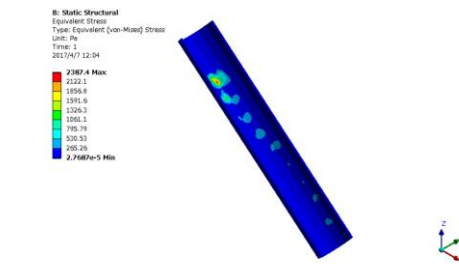
Fig. 7.7 Stress distribution of case 1



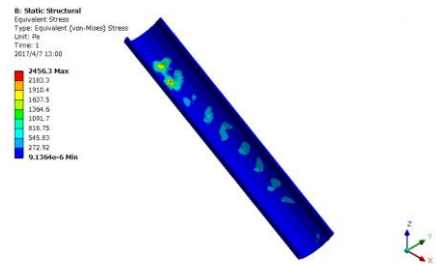
(a) $\theta=30\text{deg.}$



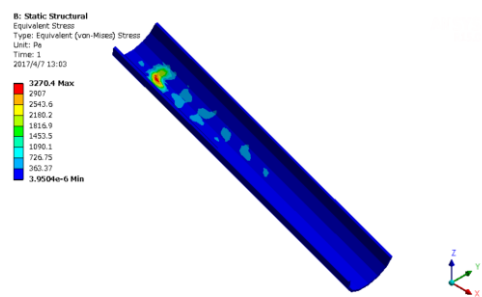
(b) $\theta=40\text{deg.}$



(c) $\theta=50\text{deg.}$

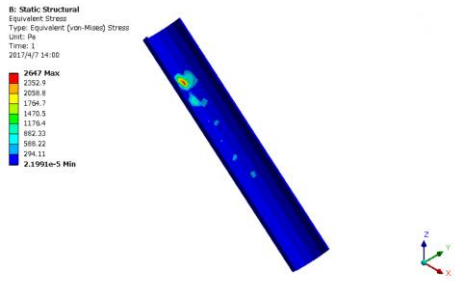


(d) $\theta=60\text{deg.}$

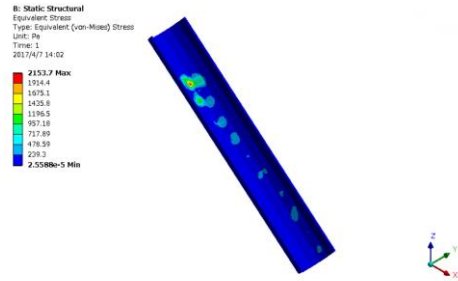


(e) $\theta=70\text{deg.}$

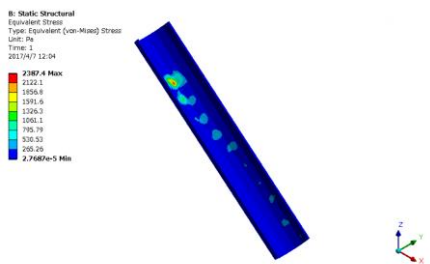
Fig. 7.8 Stress distribution of case 2



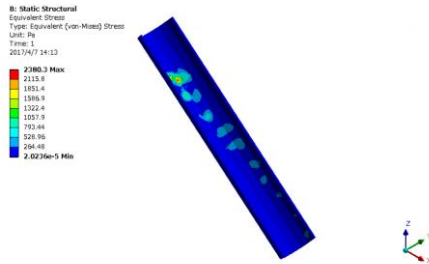
(a) $\omega=4\text{rpm}$



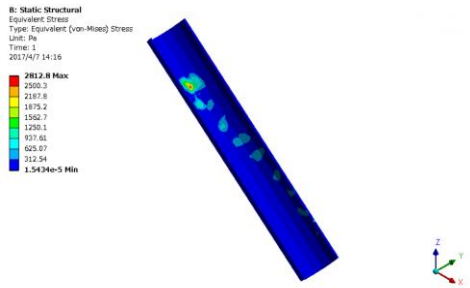
(b) $\omega=6\text{rpm}$



(c) $\omega=8\text{rpm}$

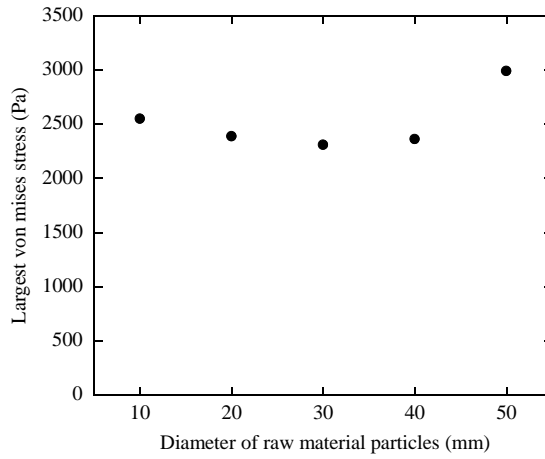


(d) $\omega=10\text{rpm}$

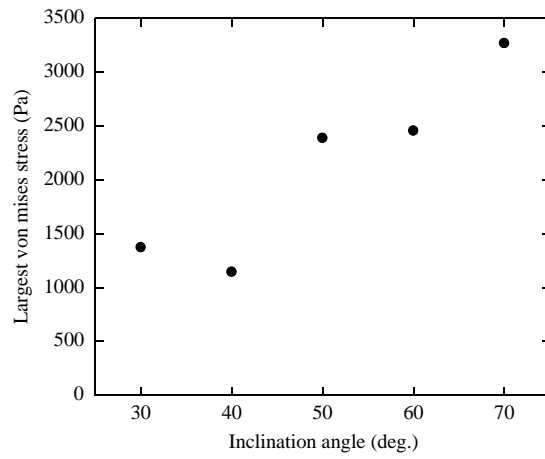


(e) $\omega=12\text{rpm}$

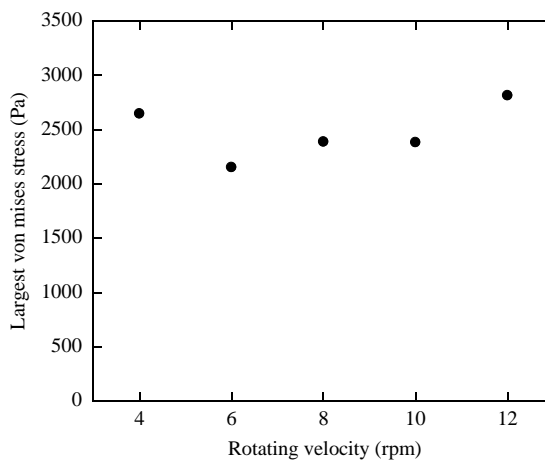
Fig. 7.9 Stress distribution of case 3



(a) Diameter of raw material particles

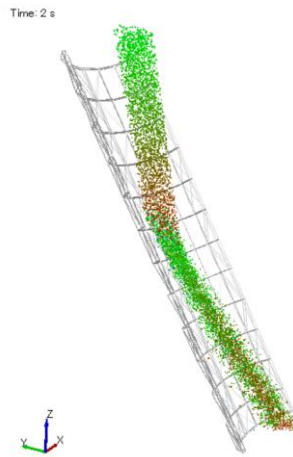


(b) Inclination angle

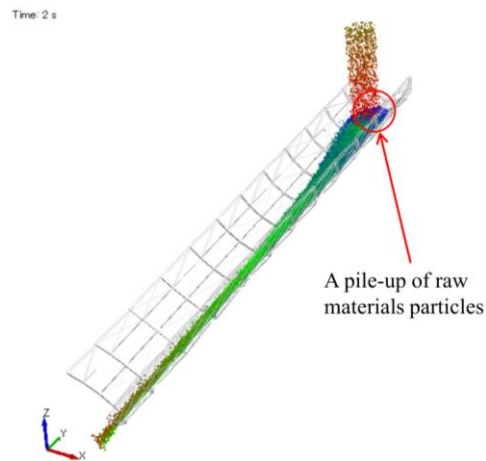


(c) Rotating velocity

Fig. 7.10 The relationship between largest von mises stress on rotating chute and diameter of solid particles d , inclination angle θ , rotating velocity ω



(a) $\theta=30\text{deg.}$



(b) $\theta=70\text{deg.}$

Fig.7.11 Velocity distribution of raw materials flow in rotating chute under low inclination angle $\theta=30\text{deg.}$ and high inclination angle $\theta=70\text{deg.}$

($d=20\text{mm}$, $\omega=8\text{rpm}$)

7.5 Conclusions

A coupled simulation of Discrete Element Method (DEM) and Finite Element Method (FEM) was used to predict the erosion on rotating chute. The movement of raw materials in rotating chute was simulated using DEM, and pressure of discrete particles on rotating chute were imported into FE model of rotating chute, and the stress state of rotating chute could be got. This work offered a useful and efficient way to predict erosion on rotating chute.

References

- [1] S. Nag, V. M. Koranne, Development of material trajectory simulation model for blast furnace compact bell-less top, *Ironmaking & Steelmaking*, 36, (2009) 371-378.
- [2] Zhao-jie TENG, Shu-sen CHENG, Guo-lei ZHAO, Peng-yu DU, Effect of Chute Rotation on Particles Movement for Bell-less Top Blast Furnace, *Journal of Iron and Steel Research, International*, 20, (2013) 33-39.
- [3] P. A. Cundall, Otto DL Strack, A discrete numerical model for granular assemblies, *Geotechnique*, 29, (1979) 47-65.
- [4] Jiayuan Zhang, Ziguo Hu, Wei Ge, Yongjie Zhang, Tinghua Li, Jinghai Li, Application of the discrete approach to the simulation of size segregation in granular chute flow, *Industrial & engineering chemistry research*, 43, (2004) 5521-5528.
- [5] Z. Y. Zhou, H. P. Zhu, A. B. Yu, B. Wright, P. Zulli, Discrete particle simulation of gas–solid flow in a blast furnace, *Computers & Chemical Engineering*, 32, (2008) 1760-1772.
- [6] Zongyan Zhou, Haiping, Zhu, Aibing Yu, Paul Zulli, Numerical investigation of the transient multiphase flow in an ironmaking blast furnace, *ISIJ international* 50, (2010) 515-523.
- [7] Yaowei Yu, Henrik Saxén, Experimental and DEM study of segregation of ternary size particles in a blast furnace top bunker model, *Chemical Engineering Science*, 65, (2010) 5237-5250.
- [8] Yaowei Yu, Henrik Saxén, Effect of DEM parameters on the simulated inter-particle percolation of pellets into coke during burden descent in the blast furnace, *ISIJ international*, 52, (2012) 788-796.
- [9] Zirun Wang, Weimin Dong, Hui Yao, Yi Chen, Study on variation of stress of ball mill liner at various rotating speed ratio based on EDEM-FEM coupling, *Mining & Processing Equipment (Chinese Journal)*, 44, (2016) 29-33.

Chapter 8

General conclusions and prospects for future work

8.1 General conclusions

In this thesis, an important material damage mode, erosion, is studied by using numerical simulations. The whole work can be classified into 5 individual studies. The conclusions of this work are summarized as follows:

1. 3D Finite Element (FE) model of single spherical particle impact on spheroidal carbide cast iron (SCI) and spheroidal graphite cast iron (FCD) were built via LS-DYNA. The erosion performances for these two materials were discussed using equivalent plastic strain and von mises stress on target material after single spherical particle impact. The simulation results showed no difference in equivalent plastic strain on SCI at different impact angles, but largest equivalent plastic strain occurred around 60~80deg. on FCD. The tendency of equivalent plastic strain at different impact angles is same with that of erosion rate at different impact angles obtained from erosion tests. Therefore, it is possible to verify impact angle dependence of erosion by discussing plastic deformation on materials. The phenomenon of lower erosion on SCI than that on FCD as well as almost no difference for erosion on SCI at different impact angles can be explained by the existence of spheroidal carbides with high yield stress in SCI, indicating that spheroidal carbides can restrain the plastic deformation on the eroded surface.

2. 3D Finite Element (FE) model of single spherical particle impact on mild steel (SS400) and spheroidal graphite cast iron (FDI) were built via ANSYS/LS-DYNA. The reason to use these two kinds of material is that FDI can be seen as combination of matrix and spheroidal graphite, the mechanical properties of matrix is similar with that of SS400, so it is convenient to discuss the influence of spheroidal graphite.

Considering that erosion is combination of cutting effect and deformation effect by impact particles, the erosion mechanisms for these two materials were explained using a combining discussion of plastic strain and shear stress on material surface after single spherical particle impact. The simulation results showed that plastic strain and shear stress on FDI showed both higher than those on SS400, which could explain that erosion on FDI is higher than that on SS400 experimentally. Meanwhile, as for SS400, plastic strain changed little at different impact angles, but shear stress changed obviously with maximum shear stress occurring at impact angle 20deg.. And as for FDI, shear stress kept unchanged at different impact angles, but maximum plastic strain occurred around 50~80deg.. So it is inferred that plastic strain and shear stress play main role on erosions of FDI and SS400 respectively.

3. 3D Finite Element (FE) model of 5 spherical particles impacting on a mild steel ASTM A36 (similar with SS400) was built via ABAQUS. Material loss on target material was got by using two different material models, namely Johnson-Cook material model and simple material model with shear failure criterion. The erosion performances under these 2 different material models were discussed. (i) As for simple material model, increasing of shear failure not only lowered material loss, but also shifted the impact angle for maximum material loss from higher to lower. Material loss of shear failure $\varepsilon_f = 1.03$ was nearly similar with that under Johnson-Cook material model. (ii) Higher friction coefficient made more material loss under both material models, but simple material model played more obvious effect on increasing of material loss than Johnson-Cook material model. (iii) Craters under these 2 different material models showed similar shapes, but simple material model caused larger deformation than Johnson-Cook material model.

4. A coupled method of Finite Element (FE) and Smoothed Particles Hydrodynamics (SPH) was used in simulations of angular particles impact on mild steel. The simulation was conducted via ANSYS/LS-DYNA. Angular particles were simplified as cones. Different cones can be got by varying the conic angle but keeping volume of cones same, which can make these different cones have same kinetic energy when they are impacting on target material. Simulation results showed that a

tiny material is easy to protrude from material surface for cones impact at low impact angles, and maximum plastic strain always occurs at the nearby region of notch, especially occurs at the root of protruded material when impact angle is low. Normal impact of cone provides greater breakage than oblique impact. With increasing of angularity, breakage increases for oblique impact but keeps nearly unchanged for normal impact. Normal impact of cones penetrates deeper than those of oblique impact, and larger angularity makes penetration depth shallower. Oblique impact of cones make larger plastic strain than normal impact, and larger angularity makes plastic strain larger for oblique impact, whereas a peak value of plastic strain exists at 70deg. for normal impact.

5. For a specified apparatus rotating chute, a coupled simulation of Discrete Element Method (DEM) and Finite Element Method (FEM) was used to predict the erosion state on liners of rotating chute. The simulation was conducted via EDEM and ANSYS workbench. Through DEM, the movement of raw materials in rotating chute was simulated, we can get which liners were under erosion by observing the stream of raw materials flow. And then the pressure of raw material particles on liners were transferred into FE model of rotating chute, the mechanical state on liners of rotating chute could be computed, we can get the stress distribution on liners so as to know which liners are easily eroded. It is found that the maximum stress always occurs at the liners just under the falling raw material flow, which means that these liners are easily for erosion occurring. By using this method, influences of diameter of raw material particles, inclination angle of chute, rotating velocity were also discussed. Simulation results showed that inclination angle influences erosion on rotating chute much more obvious than diameter of raw material particles and rotating velocity. Erosion on rotating chute decreases firstly and then increases, first decrease is because distance between pouring point and impact point becomes short with increasing of inclination angle, following increase is because large number of raw material is easy to pile up at high inclination angle.

8.2 Prospects for future work

Erosion is a very complicated process of deformation and loss on material surface. It is strongly affected by many factors, and the impact particles for erosion are always entrained in some fluid such as air or liquid, meanwhile, the process of erosion may also occur accompanying with some physical or chemical transitions on material surface. Considering these reasons, several recommendations as follows are given for erosion problems in the future work:

1. Angular particles were simplified as cones in this work, but the shapes and orientations of angular particles in actual cases are very complex. So it is necessary to conduct researches for erosion when impact particles have other shapes, and the impact process of particle with different orientations.

2. Although mass loss has been worked out, the relation of erosion factors on mass loss of target material, such as impact velocity, diameters of impact particles, impact angles etc., is still unclear. In the future work, a relation between these factors should be found, it is better to derive an equation of mass loss for these factors.

3. Erosion usually occurs in devices for solid-fluid conveying. For example, in our experiments, the impact particles were also entrained in air flow. However, in the simulations of this work, the fluid around impact particles was not considered. So, in the future work, it is better to consider a coupled simulation of solid and fluid into erosion problems.

4. The erosive prediction method for rotating chute in this work was conducted using numerical simulation, the results have not been verified with actual works. It is better to compare the simulation results with actual results to verify its validation.

ACKNOWLEDGEMENT

I would like to express my sincere gratitude and profound appreciation to my supervisor, Professor Kazumichi Shimizu for his precious guidance, assistance and encouragement during period of my doctoral student. It is my great honor to study in his laboratory and have this great opportunity to study abroad. He provided financial support for me to attend international conferences, so that I could get these chances to communicate with other foreign researchers. He is an open-minded, optimistic person, excellent in social skills. I have learnt a lot from him for his attitude toward career and life, which will benefit me for my whole life.

I would like to express my great gratitude to Dr. Kenta Kusumoto and Dr. Takafumi Funabiki, they provided many good advice and valuable comments for my study.

I would like to express my great gratitude to the secretary of my supervisor, Mrs. Yaegashi for her patient care and support to my life. Without her help, my life in Muroran would become more difficult.

I would like to express my great gratitude to Muroran Institute of Technology for her academic and financial supports to me. It is my great honor to study here and have this chance to make so many kind friends.

Finally, I am most grateful to my parents. They give me great support and lots of love, which help me to go further in this road. When I became desperate, their warm and comfortable talk made me strong to carry my way on.

PUBLICATIONS AND PRESENTATIONS

Journal Papers:

- [1] 肖磊, 清水一道, 楠本賢太, 球状炭化物鑄鉄のエロージョン摩耗における衝突角度依存性, 鑄造工学, 第 88 卷, 第 5 号(2016), pp252~257.
- [2] Lei Xiao, Kazumichi Shimizu, Kenta Kusumoto, Impact angle dependence of erosive wear for spheroidal carbide cast iron, Materials Transactions, 58.7, (2017) 1032-1037.

Presentations and proceedings in international conferences:

- [1] Lei Xiao, Kazumichi Shimizu, Kenta Kusumoto, Finite Element Method Analysis of Single Impact of Spherical Particles on FCD and SCI, The 13th Asian Foundry Congress (AFC-13), (2015. 10. 28, Hanoi, Vietnam)
- [2] Lei Xiao, Kazumichi Shimizu, Kenta Kusumoto, Impact behaviors of SS400 by spherical and tetrahedral solid particle through Finite Element Simulation, The 72nd World Foundry Congress (WFC-72), Nagoya, Japan(2016. 5. 25, Nagoya, Japan)

Presentations in Japan conferences:

- [1] Xiao Lei, Kazumichi Shimizu, Hiroya Hara, Kenta Kusumoto, Impact behavior of revolving chute liners by ball drop test, MIER2015, Muroran Institute of Technology, Japan. (2015. 5. 30, 北海道室蘭市)
- [2] 肖磊, 清水一道, 楠本賢太, 単一四面体粒子の衝突における延性材料の FEM 解析, 社団法人日本鑄造工学会, 第 167 回全国講演大会, (2015. 10. 24 北海道室蘭市)

LIST OF FIGURES

Chapter 1 Introduction and background

Fig. 1.1 Erosion phenomenon in blast furnace	4
Fig. 1.2 Classification of factors affecting erosion	4
Fig. 1.3 Typical curves of erosion and impact angle for ductile/brittle materials and cast iron	5
Fig. 1.4 Schematic view of Finnie's model for ductile material	6
Fig. 1.5 Craters on aluminum specimens at impact angle 18.5deg., impact velocity is 220m/s and 210m/s	8
Fig. 1.6 Two modes of surface deformation impact by an angular particle	8
Fig. 1.7 Surface deformation impact by a spherical particle	9
Fig. 1.8 Incremental erosion rate of 1075 (240 μ m SiC; velocity V=30.5m/s; angle of impingement, 30deg.)	9
Fig. 1.9 Numerical model of 105 irregular particles impact in [30] (target material is built using SPH method)	14
Fig. 1.10 Numerical model in [47] (target material is built using DEM)	14
Fig. 1.11 Previous FE models of our laboratory	15
Fig. 1.12 Structure of works in this thesis	16

Chapter 2 Experiments

Fig. 2.1 Microstructure of FCD and SCI	22
Fig. 2.2 Appearance of specimen	23
Fig. 2.3 Appearance of impact particles	23
Fig. 2.4 Blasting machine	24
Fig. 2.5 Test stage	24

Chapter 3 Impact angle dependence of erosion for spheroidal carbide cast iron

Fig. 3.1 FEM model	27
Fig. 3.2 3D observation of indentation depth generate on the target surface for FEM model	29
Fig. 3.3 Results of 3D FEM analysis for single particle impact	30
Fig. 3.4 Indentation depth as function of impact time for specimens	30
Fig. 3.5 Observation of indentation of specimens in single particle impact tests	31
Fig. 3.6 Correlation diagram of indentation depth between simulation results and test results	31
Fig. 3.7 Von mises stress distribution of specimens by FEM simulation	32
Fig. 3.8 Equivalent plastic strain distribution of specimens by FEM simulation	34
Fig. 3.9 Total equivalent plastic strain as function of impact angle for specimens	34
Fig. 3.10 Erosion rate as function of impact angle for specimens	35

Chapter 4 Finite element analysis of single particle impact on mild steel and spheroidal graphite cast iron

Fig. 4.1 FE model for SS400	39
Fig. 4.2 FE model for FDI	40
Fig. 4.3 Arrangement of spheroidal graphite particles in layer A and layer B	41
Fig. 4.4 Positions of spheroidal graphite particles in FDI	41
Fig. 4.5 Distribution of z-displacement at impact angle 30deg. from FE simulation	43
Fig. 4.6 Appearance of crater from single particle impact test	44
Fig. 4.7 Crater depth vs impact angle	44
Fig. 4.8 Erosion rate vs impact angle from test	45
Fig. 4.9 Distribution of plastic strain at impact angle 30deg.	47
Fig. 4.10 Distribution of shear stress at impact angle 30deg.	48
Fig. 4.11 Distribution of plastic strain on material surface with thickness 0~20 μ m at impact angle 30deg.	49
Fig. 4.12 Distribution of shear stress on material surface with thickness 0~20 μ m at impact angle 30deg.	50
Fig. 4.13 Plastic strain and shear stress vs impact angle on material surface with	

different thickness of SS400 and FDI (A-30)	50
Fig. 4.14 Plastic strain and shear stress vs impact angle on material surface of SS400 and FDI with different graphite positions	51
Chapter 5 A comparative study of material loss and crater deformation on ductile material during erosion simulation using 2 different material models	
Fig. 5.1 FE model and mesh	57
Fig. 5.2 Relationship between Material loss and impact angle under different shear failure ϵ_f for simple material model ($\mu=0.2$)	59
Fig. 5.3 Target material with maximum material loss of 2 different material models ($\mu=0.2$)	59
Fig. 5.4 Ratio of erosion vs impact angle from FEM and erosion tests	60
Fig. 5.5 Appearance of erosion surfaces for SS400	61
Fig. 5.6 Schematic of role of friction during erosion	61
Fig. 5.7 Relationship between material loss and impact angle from FEM under different friction coefficients	62
Fig. 5.8 Comparison of maximum material loss of 2 different material model under friction coefficients $\mu=0.1$ and 0.5	62
Fig. 5.9 Distribution of displacement in Z direction after first particle impact from FEM ($\mu=2$, impact direction is along positive x-axis)	64
Fig. 5.10 Appearance of craters after single particle impact test	65
Fig. 5.11 Crater depth and pile-up height at different impact angle ($\mu=0.2$ for FEM)	65
Chapter 6 Impact simulation of angular particles on mild steel using a coupled method of finite element and smoothed particle hydrodynamics	
Fig. 6.1 Deformation on target material under spherical particle and angular particle impact using Lagrange meshes	69
Fig. 6.2 Numerical models	75

Fig. 6.3 Cones with different conic angle θ 76

Fig. 6.4 Plastic strain on target material after 5 particle impact at impact angles 10deg., 30deg., 50deg., 70deg. and 90deg. (impact direction was from left to right for 10deg., 30deg., 50deg. and 70deg.) 78

Fig. 6.5 Process of material removal for cone impact after 2, 5 and 7 particles impact at impact angle 20deg. 79

Fig. 6.6 Relationship between plastic strain and impact angle from simulation . . . 80

Fig. 6.7 Relationship between erosion rate and impact angle from experiment . . . 80

Fig. 6.8 Energy evolution of single standard cone impact at impact angle 30deg. and 90deg. 82

Fig. 6.9 Simulation results under single cone impact with different conic angles . . . 83

Fig. 6.10 Schematic of movement of single cone for oblique and normal impact . . . 84

Chapter 7 Erosive prediction on liners of rotating chute using a coupled simulation of DEM and FEM

Fig. 7.1 Schematic view of interaction between two particles 90

Fig. 7.2 Schematic view of sum forces by neighboring particles on particle i . . . 91

Fig. 7.3 Arrays of liners in rotating chute 92

Fig. 7.4 Size of rotating chute 93

Fig. 7.5 Number of liners of rotating chute 94

Fig. 7.6 Velocity distribution of raw materials flow in rotating chute ($d=20\text{mm}$, $\theta=50\text{deg.}$, $\omega=8\text{rpm}$) 96

Fig. 7.7 Stress distribution of case 1 98

Fig. 7.8 Stress distribution of case 2 99

Fig. 7.9 Stress distribution of case 3 100

Fig. 7.10 The relationship between largest von mises stress on rotating chute and diameter of solid particles d , inclination angle θ , rotating velocity ω . . . 101

Fig. 7.11 Velocity distribution of raw materials flow in rotating chute under low inclination angle $\theta=30\text{deg.}$ and high inclination angle $\theta=70\text{deg.}$ ($d=20\text{mm}$,

$\omega=8\text{rpm}$) 102

LIST OF TABLES

Table 2.1 Chemical compositions (mass%) of FCD and SCI	22
Table 2.2 Chemical composition (mass%) and mechanical properties of FDI and S S 4 0 0 ^a	23
Table 3.1 Analysis conditions of material and particles	27
Table 4.1 Material Parameters	42
Table 5.1 Material parameters of ASTM A36 and SS400	56
Table 6.1 Material parameters of ASTM A36	73
Table 6.2 Dimensions of cones	76
Table 7.1 Material properties	94
Table 7.2 Simulation conditions	94